

**UNIVERSIDADE ESTADUAL DE CAMPINAS**

Faculdade de Engenharia Mecânica

**LEONARDO FANTON**

**Influence of plastic deformation and  
crystallographic texture on obtaining a  
stiffness gradient in Ti-30Nb-4Sn alloy by  
laser surface melting**

**Influência da deformação plástica e da  
textura cristalográfica na obtenção de um  
gradiente de rigidez na liga Ti-30Nb-4Sn  
por fusão superficial por laser**

CAMPINAS

2017

LEONARDO FANTON

**Influence of plastic deformation and  
crystallographic texture on obtaining a  
stiffness gradient in Ti-30Nb-4Sn alloy by  
laser surface melting**

**Influência da deformação plástica e da  
textura cristalográfica na obtenção de um  
gradiente de rigidez na liga Ti-30Nb-4Sn  
por fusão superficial por laser**

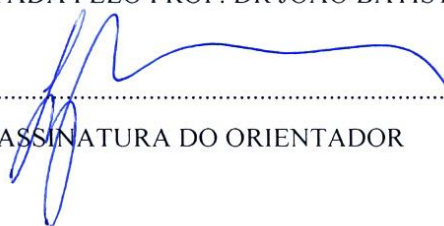
Thesis presented to the School of Mechanical Engineering of the University of Campinas in partial fulfillment of the requirements for the degree of Doctor in Mechanical Engineering, in the area of Materials and Fabrication Processes.

Tese apresentada à Faculdade de Engenharia Mecânica da Universidade Estadual de Campinas como parte dos requisitos exigidos para a obtenção do título de Doutor em Engenharia Mecânica, na Área de Materiais e Processos de Fabricação.

Orientador: Prof. Dr. João Batista Fogagnolo

ESTE EXEMPLAR CORRESPONDE À VERSÃO FINAL DA TESE  
DEFENDIDA PELO ALUNO LEONARDO FANTON, E  
ORIENTADA PELO PROF. DR JOÃO BATISTA FOGAGNOLO

ASSINATURA DO ORIENTADOR



Prof. Dr. João Batista Fogagnolo  
Dépto. de Engenharia de Manufatura e Materiais  
Faculdade de Engenharia Mecânica / UNICAMP  
Matricula 296926

CAMPINAS

2017

**Agência(s) de fomento e nº(s) de processo(s):** CAPES, 33003017  
**ORCID:** <http://orcid.org/0000-0001-6801-7798>

Ficha catalográfica  
Universidade Estadual de Campinas  
Biblioteca da Área de Engenharia e Arquitetura  
Luciana Pietrosanto Milla - CRB 8/8129

F218i Fanton, Leonardo, 1985-  
Influence of plastic deformation and crystallographic texture on obtaining a stiffness gradient in Ti-30Nb-4Sn alloy by laser surface melting / Leonardo Fanton. – Campinas, SP : [s.n.], 2017.

Orientador: João Batista Fogagnolo.  
Tese (doutorado) – Universidade Estadual de Campinas, Faculdade de Engenharia Mecânica.

1. Ligas de titânio. 2. Metais - Textura. 3. Módulo de elasticidade. 4. Caracterização de materiais. 5. Fusão a laser. I. Fogagnolo, João Batista, 1964-. II. Universidade Estadual de Campinas. Faculdade de Engenharia Mecânica. III. Título.

#### Informações para Biblioteca Digital

**Título em outro idioma:** Influência da deformação plástica e da textura cristalográfica na obtenção de um gradiente de rigidez na liga Ti-30Nb-4Sn por fusão superficial por laser

**Palavras-chave em inglês:**

Titanium alloys

Metals - Texture

Elastic modulus

Materials characterization

Laser melting

**Área de concentração:** Materiais e Processos de Fabricação

**Titulação:** Doutor em Engenharia Mecânica

**Banca examinadora:**

João Batista Fogagnolo [Orientador]

Eder Sócrates Najar Lopes

Emin Bayraktar

Andrea Madeira Kliauga

Daniel Rodrigo Leiva

**Data de defesa:** 21-02-2017

**Programa de Pós-Graduação:** Engenharia Mecânica

UNIVERSIDADE ESTADUAL DE CAMPINAS  
FACULDADE DE ENGENHARIA MECÂNICA  
COMISSÃO DE PÓS-GRADUAÇÃO EM ENGENHARIA  
MECÂNICA  
DEPARTAMENTO DE ENGENHARIA DE MANUFATURA E  
MATERIAIS  
TESE DE DOUTORADO

**Influence of plastic deformation and  
crystallographic texture on obtaining a  
stiffness gradient in Ti-30Nb-4Sn alloy by  
laser surface melting**

**Influência da deformação plástica e da  
textura cristalográfica na obtenção de um  
gradiente de rigidez na liga Ti-30Nb-4Sn  
por fusão superficial por laser**

Autor: Leonardo Fanton

Orientador: Professor Dr. João Batista Fogagnolo

A Banca Examinadora composta pelos membros abaixo aprovou esta Tese:

**Prof. Dr. João Batista Fogagnolo**

Instituição: Universidade Estadual de Campinas (Unicamp), Brasil

**Prof. Dr. Eder Sócrates Najar Lopes**

Instituição: Universidade Estadual de Campinas (Unicamp), Brasil

**Prof. Dr. Emin Bayraktar**

Instituição: Institut Supérieur de Mécanique de Paris (Supméca), França

**Profa. Dra. Andrea Madeira Kliuga**

Instituição: Universidade Federal de São Carlos (UFSCar), Brasil

**Prof. Dr. Daniel Rodrigo Leiva**

Instituição: Universidade Federal de São Carlos (UFSCar), Brasil

A Ata da defesa com as respectivas assinaturas dos membros encontra-se no processo de vida acadêmica do aluno.

Campinas, 21 de fevereiro de 2017.

## **Dedicatória**

Dedico este trabalho à minha família.

## **Agradecimentos**

Ao professor João Fogagnolo, pela orientação e entusiasmo pelo trabalho.

Aos meus companheiros de trabalho na Unicamp, Edwin, Lisiane, Jéssica, Fernando, Rodrigo e Sérgio, pela companhia e ajuda.

Aos professores Vicente Amigó e Emílio Rayón pela contribuição dada a este trabalho e por possibilitarem minha estadia na Universidade Politécnica de Valência (UPV).

Aos meus amigos de Valência: Pablo, Laís, Álvaro, Emílio e Luz, pela ajuda, conversas, cafés e sobretudo pelos bons momentos compartilhados.

Ao professor Rubens Caram e seus alunos, aos professores Hipólito Carvajal e Conrado Afonso, aos técnicos Claudenete Vieira, Claudomiro Alves e Márcia Taipina, pela ajuda oferecida na realização dos experimentos.

Ao professor Nelson Batista, por disponibilizar seu laboratório e pelos ensinamentos na área de textura cristalográfica.

Ao professor Sergio Button, pela supervisão durante o estágio de docência.

## Resumo

Este trabalho é um estudo sobre a fusão superficial a laser da liga Ti-30Nb-4Sn como forma de criar um gradiente de rigidez entre a superfície e o substrato. Foram usadas amostras deformadas por laminação a frio com redução em espessura de 24, 36, 51, 68 e 85%. Uma das amostras com 85% de deformação foi submetida a um tratamento de recristalização. Foi realizado um estudo sobre os efeitos da deformação a frio e recristalização na microestrutura, evolução de textura, módulo de elasticidade e dureza. A microestrutura de todas as amostras é composta pelas fases  $\alpha''$  e  $\beta$ . A técnica de indentação instrumentada foi utilizada para medir dureza e módulo de elasticidade. A dureza aumentou com a deformação e o módulo mostrou comportamento oposto. O tratamento térmico de recristalização fez com que o módulo de elasticidade e a dureza voltassem para valores de um material não deformado. A textura cristalográfica foi determinada por difração de raios-X (DRX) e difração de elétrons retroespalhados (EBSD). As amostras com 51% e 85% de deformação mostraram componentes de textura similares, em forma de fibras:  $[302]_{\alpha''} \parallel \text{ND}$ ,  $[110]_{\alpha''} \parallel \text{ND}$  e  $[001]_{\alpha''} \parallel \text{ND}$ . Já a amostra recristalizada mostrou dois componentes de textura:  $[110]_{\alpha''} \parallel \text{ND}$  e  $[203]_{\alpha''} \parallel \text{ND}$ . A textura da fase  $\beta$  foi medida apenas para a amostra recristalizada, sendo encontrado o componente  $[111]_{\beta} \parallel \text{ND}$ . A textura do material recristalizado foi consideravelmente mais forte que a das amostras deformadas. A diminuição de módulo de elasticidade após laminação a frio foi relacionada a discordâncias e defeitos cristalinos introduzidos pela deformação. As medidas de nanoindentação das amostras deformadas apresentaram uma diferença significativa nos valores entre indentações realizadas em diferentes seções transversais (RD, TD e ND). Essa anisotropia foi atribuída a estruturas de discordâncias provenientes da deformação a frio, e não à textura cristalográfica. Um gradiente de rigidez entre superfície e substrato foi criado nas amostras encruadas após fusão a laser, apresentando maior módulo de elasticidade na superfície tratada. Esse efeito foi atribuído à redução da densidade de discordâncias e outros defeitos cristalinos nas zonas fundida e recristalizada. A amostra recristalizada não mostrou gradiente de propriedades após fusão superficial a laser. O mapeamento EBSD realizado na região afetada pelo laser não mostrou nenhuma diferença significativa de textura entre superfície e substrato.

## Abstract

This work is a study about the laser surface melting treatment in a Ti-30Nb-4Sn alloy as a method to create a stiffness gradient between surface and substrate. It was used cold rolled specimens with thickness reductions of 24, 36, 51, 68 and 85%. One sample with 85% of deformation undergone recrystallization heat treatment. It was carried out a study about the effects of cold deformation and recrystallization on the microstructure, texture evolution, elastic modulus and hardness. Microstructure of all samples showed to be composed of  $\beta$  and  $\alpha''$  phases. Instrumented indentation (nanoindentation) was the technique used to measure hardness and elastic modulus. Hardness increased with deformation, while elastic modulus showed the opposite behavior. Recrystallization heat treatment caused elastic modulus and hardness to return to values of an undeformed specimen. The crystallographic texture was determined by X-ray diffraction (XRD) and electron backscatter diffraction (EBSD). The 51% and 85% deformed samples showed similar texture components, in form of fibers:  $[302]_{\alpha''} \parallel \text{ND}$ ,  $[110]_{\alpha''} \parallel \text{ND}$  and  $[001]_{\alpha''} \parallel \text{ND}$ . The recrystallized sample showed two fiber texture components:  $[110]_{\alpha''} \parallel \text{ND}$  and  $[203]_{\alpha''} \parallel \text{ND}$ . The texture of  $\beta$  phase was only measured for the recrystallized sample, being found a  $[111]_{\beta} \parallel \text{ND}$  texture component. Texture of recrystallized specimen was considerably stronger than as-deformed specimens. The decrease in elastic modulus after cold rolling was ascribed to dislocations and crystalline defects introduced by deformation. Nanoindentation measurements of deformed samples presented a significant difference in values between indentations performed on different cross sections (RD, TD and ND). This anisotropy was attributed to dislocation structures derived from cold deformation, rather than crystallographic texture. A stiffness gradient between surface and substrate was created in the work-hardened specimens after laser surface melting, showing higher elastic modulus in the treated surface. This effect was attributed to the reduction of dislocation density and other crystalline defects in the fusion and recrystallized zones. The recrystallized sample did not show any gradient of properties after laser surface melting. The EBSD mapping performed in the laser affected zone did not show any significant difference of texture between surface and substrate.



## List of Figures

Figure 1: Cold rolling process schema and reference axes ND, TD and RD. Adapted from (“Core Materials - Colaborative Open Resource Environment - for Materials”, 2010).	22
Figure 2: Euler angles and rotations (1, 2 and 3) as described by the Bunge notation. Adapted from (ENGLER O., 2010).	23
Figure 3: Rolled sheet showing different types of crystallographic texture. The cube inside each grain represent the grain orientation. (a) Sample with random grain orientation (no texture), (b) sample with a very strong (100)[010] texture component and (c) sample with two texture components called Goss and Cube textures. Adapted from (SUWAS; RAY, 2014).	24
Figure 4: (a) Schematic representation of the procedure to obtain a pole figure by X-ray diffraction and (b) the representation of $\alpha$ and $\beta$ angles on a pole figure. Adapted from (SUWAS; RAY, 2014).	26
Figure 5: (a) EBSD experimental setup and (b, c) examples of Kikuchi patterns for different crystal orientations. Adapted from (TRAGER-COWAN, 2012)	28
Figure 6: Examples of (a) phase map and (b) band contrast map for a mineral specimen containing three phases: forsterite, enstatite and diopside. Examples from MTEX MATLAB Toolbox (BACHMANN; HIELSCHER; SCHAEBEN, 2010).	29
Figure 7: Color assignment to different crystal directions for (a) cubic crystal symmetry and (b) orthorhombic crystal symmetry. Constructed with MTEX MATLAB Toolbox (BACHMANN; HIELSCHER; SCHAEBEN, 2010).	30
Figure 8: Examples of orientation maps for the forsterite phase: (a) IPF colored maps showing the crystal orientation aligned to X, Y and Z axes and (b) Euler colored maps. The forsterite phase has orthorhombic crystal symmetry and the specimen symmetry is triclinic. Examples from MTEX MATLAB Toolbox (BACHMANN; HIELSCHER; SCHAEBEN, 2010).	31
Figure 9: Examples of orientation distribution functions of two ideal texture components: (a) (130)[-310] peak-type texture component and (b) [302]//ND fiber texture component,	

represented in the Euler space for orthorhombic crystal and orthotropic specimen symmetries. Created with MTEX MATLAB Toolbox (BACHMANN; HIELSCHER; SCHAEBEN, 2010).....	33
Figure 10: Isomorphous titanium phase diagram. Adapted from (GEPREEL, 2013). $M_s$ and $M_f$ are martensite start and finish temperatures, respectively.....	34
Figure 11: Schematic illustration showing the correspondence between the cubic and orthorhombic titanium phases. From (KIM et al., 2006).....	35
Figure 12: Conduction and keyhole laser melting modes. ....	39
Figure 13: Laser surface remelting experimental schema. ....	44
Figure 14: Complete experimental planning of this work.....	45
Figure 15: VLM images for a sample with 24% of deformation. (a, b, c, d) Images with different magnifications of the same grain and (e, f) details of other two grains.....	47
Figure 16: VLM images of a sample with 36% of deformation.....	48
Figure 17: VLM images of a sample with 51% of deformation.....	49
Figure 18: VLM images of a sample with 68% of deformation. Some shear bands are indicated by arrows.....	49
Figure 19: VLM images of a sample with 85% of deformation. Some shear bands are indicated by arrows.....	50
Figure 20: VLM images of the recrystallized sample (85%REC).....	51
Figure 21: X-ray diffraction patterns for samples with 0% (FANTON et al., 2016), 24%, 36%, 51%, 68%, 85% of deformation and recrystallized (85%REC).....	53
Figure 22: Transmission electron microscopy of the 24% deformed sample. (a) Dark field image and its (b) selected area diffraction pattern of $[001]_\beta$ zone axis. ....	54
Figure 23: Visible-light microscopy images of the 51% deformed sample, showing the microstructure evolution from the fusion zone, passing through the heat affected zone until the substrate, sequentially from (a) to (f). The grains near to the fusion zone were	

recrystallized. Grain size of the recrystallized region progressively decreases as it gets farther from the fusion zone. ....	55
Figure 24: (a, b) VLM images of the fusion zone (FZ) and heat affected zone (HAZ) of the 51% deformed sample. ....	57
Figure 25: Fusion zone (FZ) and heat affected zone (HAZ) images of the 85% deformed sample. (a) General view of FZ and HAZ. (b) Grain size of the recrystallized region progressively decreases as it gets farther from the fusion zone. (c) Some grain boundaries cross the FZ/HAZ interface. (d, e) Martensite laths are observed in both HAZ and FZ.	58
Figure 26: Visible-light microscopy images of the recrystallized (85%REC) sample. No difference is observed between heat affect zone and substrate. ....	59
Figure 27: (a) FSD image of the 51% deformed sample and (b) region marked with a dashed square in (a). The dashed yellow lines indicate the boundaries between fusion zone (FZ) and heat affected zone (HAZ). Arrows indicate regions of the FZ with no martensite structure.....	60
Figure 28: Hardness of deformed samples and recrystallized sample (85%REC), measured by nanoindentation on RD, ND and TD cross sections and by microindentation on ND direction (FANTON et al., 2016).....	61
Figure 29: Elastic modulus of deformed samples and recrystallized sample (85%REC), measured by nanoindentation on RD, ND and TD cross sections and by ultrasound pulse-echo method on ND direction (FANTON et al., 2016).....	62
Figure 31: Experimental pole figures of the 51%, 85% and 85%REC samples. Scale bars are in arbitrary units.....	68
Figure 32: Location of some ideal fiber and peak-type texture components in the Euler orientation space ( $\phi_1, \Phi, \phi_2$ ). ....	69
Figure 33: Orientation distribution functions of (a) 51%, (b) 85% and (c) recrystallized (85%REC) samples. Scale bars represent multiples of random distribution (m.r.d.).....	71

Figure 34: Reconstructed pole figures from the estimated orientation distribution functions (ODFs) of samples (a) 51%, (b) 85% and (c) 85%REC. Scale bars represent multiples of random distribution (m.r.d.).	72
Figure 35: (a, b, c) EBSD band contrast map of three different regions of a recrystallized (85%REC) sample and (d) the mean angular deviation (MAD) distribution for all regions summed.	73
Figure 36: Orientation distribution functions of (a) $\alpha''$ and (b) $\beta$ phases for the recrystallized sample (85%REC), estimated from EBSD measurements of the regions shown in Figure 35. Scale bars represent multiples of random distribution (m.r.d.).	74
Figure 37: EBSD analysis of a single grain composed by a matrix of $\beta$ phase and $\alpha''$ martensite laths formed upon rapid cooling. (a) Band contrast map; (b, c) Euler colored orientation maps for (b) $\beta$ and (c) $\alpha''$ phases. (d, e, f, g, h) Pole figure plots for all identified orientations.	78
Figure 38: Variation of elastic modulus as a function of crystal directions of (a) $\beta$ and (b) $\alpha''$ phases, according to the elastic constants calculated by Sun et al. (SUN et al., 2007).	79
Figure 39: Influence of crystallographic texture on the specimen's elastic modulus anisotropy, considering (a, b, c) the $\alpha''$ ODFs found by XRD analysis of 51%, 85% and 85%REC samples and (d, e) the $\alpha''$ and $\beta$ ODFs found by EBSD analysis of the 85%REC sample. The average elastic modulus of the 85%REC sample is shown on (f).	82
Figure 40: EBSD analysis for the 85% deformed and laser surface melted sample. (a) Band contrast (BC) image showing the fusion zone (red rectangle) and heat affected zone (blue rectangle). (b, c) Orientation maps for the (b) $\beta$ phase and (c) $\alpha''$ phase superposed with the BC image. EBSD analysis were performed on the RD-ND plane, transverse to laser tracks, and the orientation maps show the crystals directions aligned in the normal direction.	83
Figure 41: EBSD analysis for three distinct regions of the recrystallized (85%REC) and laser surface melted sample. (a, b, c) Band contrast (BC) image showing the fusion zone (red rectangle) and heat affected zone (blue rectangle). (d, e, f, g, h, i) Orientation maps	

for the (d, e, f)  $\beta$  phase and (g, h, i)  $\alpha''$  phase superposed with the BC image. EBSD analysis were performed on the RD-ND plane, transverse to laser tracks, and the orientation maps show the crystals directions aligned in the normal direction..... 85

Figure 42: EBSD analysis for the 85% deformed and laser surface melted sample. (a) Band contrast (BC). (b, c) Orientation maps for the (b)  $\beta$  phase and (c)  $\alpha''$  phase superposed with the BC image. (d, e, f) EDS maps for Ti, Nb and Sn elements. EBSD analysis were performed on the RD-ND plane, transverse to laser tracks, and the orientation maps show the crystals directions aligned in the normal direction. Laser track boundaries are marked with red dashed lines..... 87

Figure 43: EBSD analysis for the recrystallized (85%REC) and laser surface melted sample. (a) Band contrast (BC). (b, c) Orientation maps for the (b)  $\beta$  phase and (c)  $\alpha''$  phase superposed with the BC image. (d, e, f) EDS maps for Ti, Nb and Sn elements. EBSD analysis were performed on the RD-ND plane, transverse to laser tracks, and the orientation maps show the crystals directions aligned in the normal direction. Laser track boundary is marked with a red dashed line. .... 87

Figure 44: EBSD analysis for the recrystallized (85%REC) and laser surface melted sample. (a) Band contrast (BC). (b, c) Orientation maps for the (b)  $\beta$  phase and (c)  $\alpha''$  phase superposed with the BC image. (d, e, f) EDS maps for Ti, Nb and Sn elements. EBSD analysis were performed on the RD-ND plane, transverse to laser tracks, and the orientation maps show the crystals directions aligned in the normal direction. Laser track boundaries are marked with a red dashed line..... 88

Figure 45: EBSD analysis for the 85% deformed and laser surface melted sample. (a) Band contrast (BC). (b, c) Orientation maps for the (b)  $\beta$  phase and (c)  $\alpha''$  phase superposed with the BC image. (d, e, f) EDS maps for Ti, Nb and Sn elements. EBSD analysis were performed on the RD-ND plane, transverse to laser tracks, and the orientation maps show the crystals directions aligned in the normal direction..... 89

Figure 46: EBSD analysis for the 85% deformed and laser surface melted sample. (a) Band contrast (BC). (b, c) Orientation maps for the (b)  $\beta$  phase and (c)  $\alpha''$  phase superposed with the BC image. (d, e, f) EDS maps for Ti, Nb and Sn elements. EBSD

analysis were performed on the RD-ND plane, transverse to laser tracks, and the orientation maps show the crystals directions aligned in the normal direction..... 89

Figure 47: EBSD analysis for the recrystallized (85%REC) and laser surface melted sample. (a) Band contrast (BC). (b, c) Orientation maps for the (b)  $\beta$  phase and (c)  $\alpha''$  phase superposed with the BC image. (d, e, f) EDS maps for Ti, Nb and Sn elements. EBSD analysis were performed on the RD-ND plane, transverse to laser tracks, and the orientation maps show the crystals directions aligned in the normal direction..... 90

## List of Tables

Table 1: Composition of the alloy determined by XRF. ....	46
Table 2: Overview of the crystallographic texture components observed by XRD and EBSD analyses. It was used a tolerance of 15° from ideal orientation for quantifications. ....	76

# List of Abbreviations and Acronyms

## Latin letters

BC: Band contrast

C: Stiffness (GPa)

°C: Degrees Celsius (temperature)

CSM: Continuous stiffness measurement (nanoindentation test)

E: Elastic modulus (GPa)

EBSD: Electron backscatter diffraction

EBSP: Electron backscatter pattern

FSD: Forward scatter detector (SEM)

FZ: Fusion zone

H: Hardness (GPa)

(hkl): Miller indices of a crystallographic plane

HAZ: Heat affected zone

IPF: Inverted pole figure

K: Kelvin (temperature)

LSM: Laser surface melting

MAD: Mean angular deviation

m.d.r.: Multiples of random distribution

$M_f$ : Martensite finish transformation temperature

$M_s$ : Martensite start transformation temperature

ND: Normal direction of a rolled specimen

ODF: Orientation distribution function

OIM: Orientation imaging microscopy



RD: Rolling direction of a rolled specimen

S: Compliance ( $\text{GPa}^{-1}$ )

SEM: Scanning electron microscope

TD: Transverse direction of a rolled specimen

TEM: Transmission electron microscope

[uvw]: Miller indices of a crystallographic direction

VLM: Visible-light microscope

XRD: X-ray diffraction

XEDS: X-ray energy dispersive spectroscopy

wt%: Weight percent

### **Greek letters**

$\alpha$ : Hexagonal phase of titanium

$\alpha'$ : Martensitic hexagonal phase of titanium

$\alpha''$ : Martensitic orthorhombic phase of titanium

$\beta$ : Cubic phase of titanium

$\phi_1$ : First Euler angle

$\Phi$ : Second Euler angle

$\phi_2$ : Third Euler angle

$\omega_{\text{ath}}$ : Athermal omega phase of titanium

$\omega_{\text{iso}}$ : Isothermal omega phase of titanium

# Summary

1	Introduction .....	20
1.1	Objectives .....	21
2	Literature review.....	22
2.1	Crystallographic texture.....	22
2.1.1	XRD pole figures.....	25
2.1.2	EBSD .....	26
2.1.3	The orientation distribution function.....	31
2.2	Titanium alloys .....	34
2.2.1	Titanium phases.....	34
2.2.2	Texture in $\beta$ titanium alloys.....	37
2.3	Laser surface melting.....	38
3	Experimental procedure.....	41
3.1	Preparation of samples and chemical analysis.....	41
3.2	Microscopy .....	41
3.3	X-ray diffraction .....	42
3.4	Measurement of hardness and elastic modulus.....	43
3.5	Laser surface melting (LSM).....	43
3.6	Experimental planning.....	44
4	Results and discussion.....	46
4.1	Initial characterization .....	46
4.1.1	Alloy composition .....	46
4.1.2	Microstructure and phase characterization of cold rolled and recrystallized specimens .....	46

4.1.3	Microstructure characterization of laser surface melted samples.....	54
4.2	Evaluation of hardness and elastic modulus .....	61
4.2.1	General results .....	61
4.2.2	Factors that could be affecting elastic modulus and hardness.....	65
4.3	Crystallographic texture analysis .....	66
4.3.1	Texture of cold rolled and recrystallized specimens .....	66
	XRD texture analysis.....	66
	EBSD texture analysis .....	73
	Overview of texture components.....	75
	On the origin of texture components .....	77
	Elasticity tensors.....	78
4.3.2	Texture of the laser surface melted samples.....	83
4.4	Correlation between crystallographic texture and nanoindentation measurements .....	90
5	Conclusions .....	93
6	References .....	95

# 1 INTRODUCTION

Titanium alloys are commonly used in the aerospace industry and biomedical field. Its high specific strength helps to save weight of airplanes and its biocompatibility makes it an interesting material for the replacement of hard tissues like bones and teeth. The elastic modulus of a prosthesis should have similar elastic modulus to that of the bone to which it is connected, in order to avoid the so-called stress shielding effect. No metal alloy has an elastic modulus so low as of the bone's, but titanium alloys present a much lower elastic modulus than most of metallic biomaterials.

Fatigue life is an important feature for metals in both medical and aerospace applications, whereas they are frequently subjected to cyclic stresses. Since fatigue cracks generally initiate at a surface, the surface condition of a component is very important. One way of reducing stresses on the surface of a piece is modifying it to have a lower elastic modulus than the inner material.

The control of elastic modulus in titanium alloys could improve its properties and expand its applications. As titanium phases present anisotropy of elastic properties, the control of crystallographic preferred orientation (texture) is a viable technique to modify its properties in some desired direction. Deformation and recrystallization are two common ways of modifying crystallographic texture.

The capabilities of XRD and EBSD will be explored in order to gather information about deformation and recrystallization textures. Several studies have focused on the texture of  $\beta$  (CHEN et al., 2015; CUI et al., 2010; GEPREEL, 2013; HANADA et al., 2014a, 2014b; HAYAMA et al., 2014; INAMURA et al., 2005; MATSUMOTO; WATANABE; HANADA, 2005, 2007; SANDER; RAABE, 2008; SINGH; SCHWARZER, 2008; SOKOLOVA; ANISIMOVA; SOKOLOV, 1999; YANG et al., 2014) and  $\alpha'$  phases (HANADA et al., 2014a, 2014b; HANADA; MASAHASHI; JUNG, 2013; HAYAMA et al., 2014; MATSUMOTO; WATANABE; HANADA, 2005, 2007) in titanium alloys. Nevertheless,  $\alpha'$  phase appears to have received less attention, particularly in terms of recrystallization texture. It is important to remind that, up to the present date, few information about the recrystallization texture of both  $\alpha'$  and  $\beta$  titanium phases can be found in the literature.

## 1.1 Objectives

The main objective of this work is to examine the feasibility of the obtainment of a stiffness gradient between surface and substrate of a titanium alloy. To do so, properties of both regions need to be modified. Then, cold rolling deformation and recrystallization treatment is proposed to modify properties of substrate and laser surface remelting will be used to modify surface properties.

The cold rolling and recrystallization treatment, as well as the laser surface melting, can potentially cause alterations in microstructure and crystallographic texture. Additionally, there are few studies about texture of titanium  $\alpha''$  phase, especially after recrystallization treatment. Thus, the study of crystallographic texture and its correlation with mechanical properties is a specific objective of this work.

## 2 LITERATURE REVIEW

### 2.1 Crystallographic texture

Crystals have different properties in different crystal directions. The  $\alpha$  titanium hexagonal phase, for example, presents elastic modulus of 145 GPa in the [0001] direction and 100GPa in the [10-10] direction (LUTJERING; WILLIANS, 2007). In a polycrystalline material, each grain is an individual crystal with a specific orientation relative to an external reference. For a rolled specimen, the external reference axes are the rolling direction (RD), transverse direction (TD) and normal direction (ND), as exemplified in Figure 1.

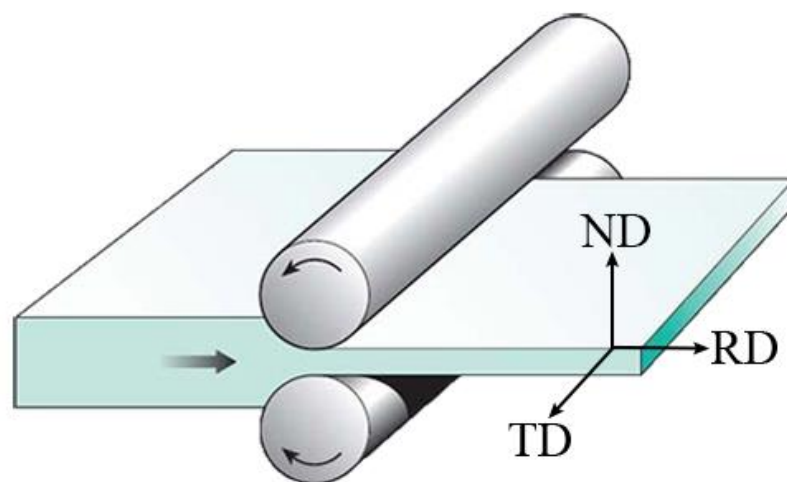


Figure 1: Cold rolling process schema and reference axes ND, TD and RD. Adapted from (“Core Materials - Colaborative Open Resource Environment - for Materials”, 2010).

If grains are randomly oriented, the average properties of the material will be isotropic. In practice, it is more common to observe a preferred orientation of grains, also called crystallographic texture. The stronger is the texture intensity, i.e., the percentage of grains within a certain orientation, more pronounced will be the average anisotropy. Some properties that are dependent on the crystallographic texture are: elastic modulus, Poisson’s ratio,

mechanical strength, ductility, toughness, magnetic permeability and electrical conductivity (ENGLER O., 2010).

The orientation of a texture component in a rolled specimen may be described by the notation  $(hkl)[uvw]$ , where  $(hkl)$  is the crystal plane parallel to the rolling plane (orthogonal to ND) and  $[uvw]$  is the crystal direction aligned to the rolling direction. Orientations may also be described by three angles called Euler angles. The Euler angles may be defined by three methods proposed by Bunge, Roe and Williams (SUWAS; RAY, 2014). In this work the Bunge notation will be adopted, since it is the most commonly used. Consider the specimen coordinate system, formed by the RD, TD and ND specimen directions, and the crystal coordinate system, formed by the  $[100]$ ,  $[010]$  and  $[001]$  crystal directions. Starting from a given orientation of the crystal relative to the specimen, the Euler angles define the necessary rotations to put the two coordinate systems into coincidence, as described in Figure 2. The first Euler angle,  $\phi_1$ , is a rotation about ND until RD becomes perpendicular to the plane formed by ND and  $[001]$ . The second Euler angle,  $\Phi$ , is a rotation around the rotated RD (RD' in Figure 2), until ND coincides with  $[001]$ . Finally, the third Euler angle,  $\phi_2$ , is a rotation around the rotated ND, making RD and TD to be coincident to  $[100]$  and  $[010]$ , respectively.

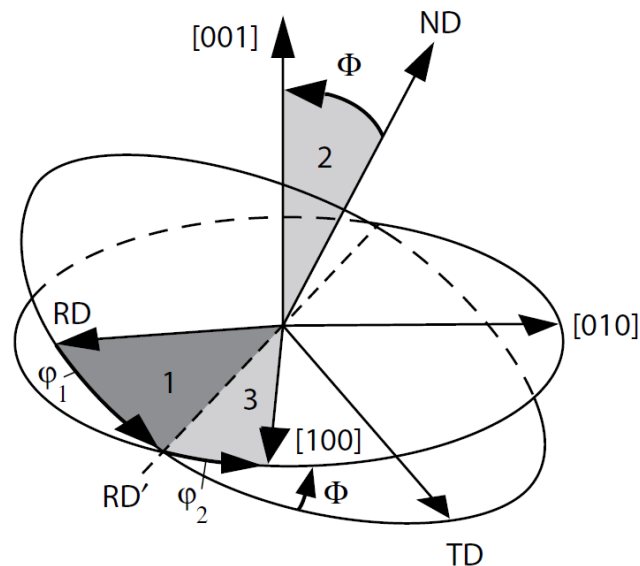


Figure 2: Euler angles and rotations (1, 2 and 3) as described by the Bunge notation. Adapted from (ENGLER O., 2010).

Figure 3 shows a schematic representation of grains orientation in a polycrystalline material.

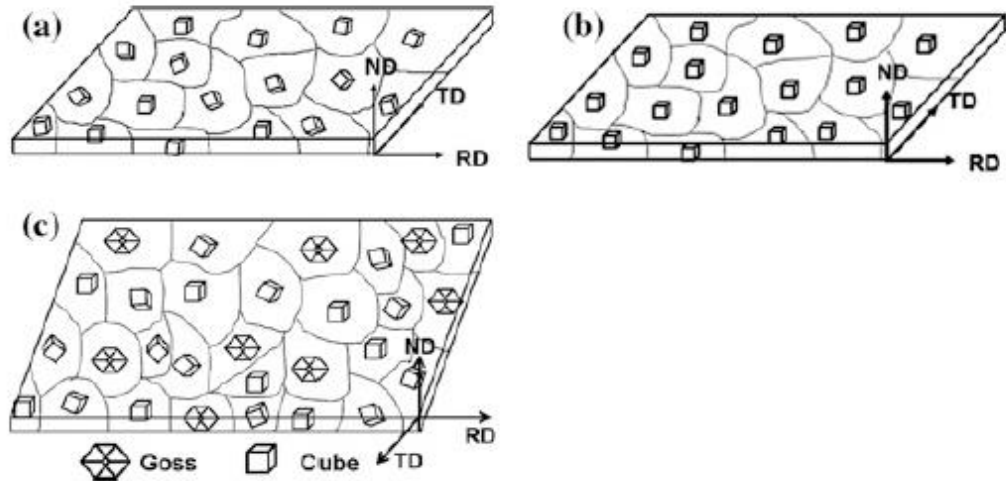


Figure 3: Rolled sheet showing different types of crystallographic texture. The cube inside each grain represent the grain orientation. (a) Sample with random grain orientation (no texture), (b) sample with a very strong (100)[010] texture component and (c) sample with two texture components called Goss and Cube textures. Adapted from (SUWAS; RAY, 2014).

The crystallographic texture of a workpiece depends on its processing history. There are four main processes that change crystallographic texture: (i) solidification, (ii) hot or cold working, as rolling and extrusion, (iii) recrystallization and (iv) phase transformation (SUWAS; RAY, 2014).

The nature of deformation texture is closely related to its crystalline structure and its deformation mechanisms (SUWAS; RAY, 2014). During plastic deformation, grains in a polycrystalline material undergo rotations until finding a more stable position. These rotations are complex and may depend on several factors, as preferential slipping systems, the initial condition of grains and interactions of grain boundaries and dislocations.

Two main theories explain the recrystallization texture. The first is the oriented nucleation theory, where nuclei with a certain orientation are preferentially activated during recrystallization. The second is the oriented growth. In this theory, nuclei are formed randomly, but only will grow the ones with a certain orientation relationship with matrix (LEE; HAN,



2013). In practice, it is very difficult to predict which texture will be obtained after processing. The most common textures obtained for different materials and processes may be found in the current literature (FIELD, 2004).

The industrial applications of textured materials are many. An example is the iron-silicon steel used in electrical transformers nuclei. These materials are manufactured in a way to generate the maximum number of grain oriented in the [100] direction, in which the body centered cubic crystals are more easily magnetized. Another application is in the fabrication of beverage cans and other deep drawing processes, where a balanced texture is necessary to avoid the production of “ears” and other problems (SUWAS; RAY, 2014).

Two of the most used methods to investigate crystallographic texture are pole figure measurement using X-ray diffraction (XRD) and electron backscattered diffraction (EBSD) based on scanning electron microscopy (SEM).

### 2.1.1 XRD pole figures

The XRD texture analysis by means of pole figures provides a statistical measure of the orientations of grains in a crystalline material. It gives no information about the spatial location of any particular grain, which is why it is considered a macrotexture measurement (SUWAS; RAY, 2014).

When a radiation with wavelength comparable to atomic spacing interact with a crystalline solid, this radiation is scattered in a mirror-like fashion, according to the Bragg’s law (HAMMOND, 2009):

*Equation 1: Bragg's law*

$$n\lambda = 2d_{hkl}\sin\theta$$

Where  $n$  is an integer (the order of diffraction),  $d_{hkl}$  is the lattice plane spacing,  $\lambda$  is the wavelength of incident wave and  $\theta$  is the angle of incidence to the planes. Planes of atoms

actually do not reflect X-rays like this, but this equations is correct in a geometrical sense and gives us a simple way to analyze crystal structures (HAMMOND, 2009).

The pole figure obtained by X-ray diffraction is a stereographic projection that shows the intensity of diffraction of a certain crystallographic plane for different positions of the specimen. Figure 4 shows a schematic representation of the experimental procedure to obtain a pole figure. The X-ray beam source and detector are kept at a constant angle  $2\theta$  at which the X-ray beam is known to be diffracted by a certain plane. Then the specimen is rotated by two angles,  $\alpha$  and  $\beta$ , in a way that the diffraction intensities of all possible positions are measured and recorded by a computer software. The angle  $\alpha$  is normally limited to  $75^\circ$  due to problems related to the increasing defocusing of X-ray beam as  $\alpha$  becomes higher.

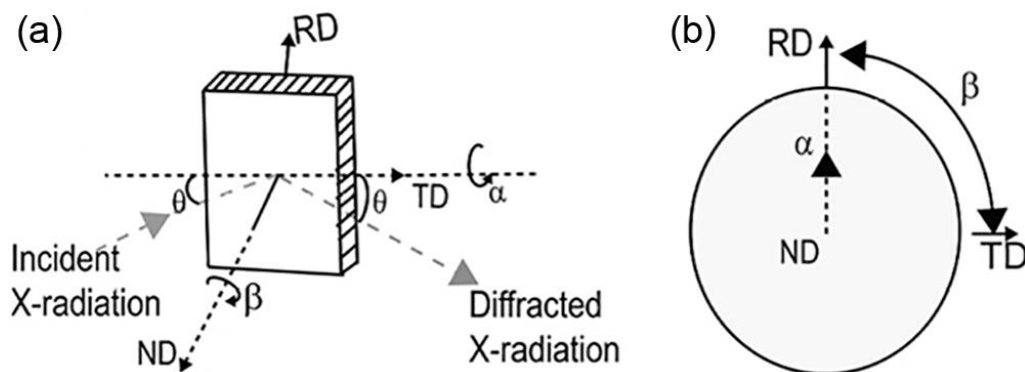


Figure 4: (a) Schematic representation of the procedure to obtain a pole figure by X-ray diffraction and (b) the representation of  $\alpha$  and  $\beta$  angles on a pole figure. Adapted from (SUWAS; RAY, 2014)

### 2.1.2 EBSD

EBSD mapping, also known as orientation imaging microscopy (OIM), has become an increasingly popular technique since the automated EBSD mapping was implemented in the 1990s. Figure 5 shows a schematic diagram of the EBSD experimental setup. When the electron beam of a SEM hits a crystalline material, some backscattered electrons are emanated through

the surface. These electrons form a flux pattern, in the form of cones, that are related to the planes in the crystal lattice in which these electrons diffracted (WILKINSON; HIRSCH, 1997). These electrons are detected by a flat phosphor screen, forming a pattern in the form of bands, known as Kikuchi pattern or electron backscattered pattern (EBSP). The EBSP is then analyzed by a special computer software that detects a number of Kikuchi bands using the Hough transform. With the information of all candidate phases previously provided by the user, the software determines the phase and orientation that best fit the pattern (WILKINSON; BRITTON, 2012). The nature of the process gives EBSD texture analysis some advantages over XRD. It performs a point-to-point analysis that creates a map describing lattice orientation and phase for each point (SCHWARTZ et al., 2009). Despite being considered a microtexture measurement, the speed of analysis offered by modern microscopes make viable the EBSD analysis of relatively large areas. Once the orientation map is created, it is easy to obtain complete pole figures of any desired plane and quantify phases and texture components.

One of the drawbacks encountered on EBSD mapping is the correct differentiation of phases with similar crystal structures. Similarities of interplanar angles and diffraction planes between the candidate phases can lead to erroneous indexing. If the examined phases have differences in composition, it is possible to overcome this obstacle by simultaneously collecting chemical information through X-ray energy dispersive spectroscopy (XEDS) (NOWELL; WRIGHT, 2004; WRIGHT; NOWELL, 2006a). EBSD sample preparation is often a concern. Even the deformation of surface during polishing could make EBSD patterns worse. Additionally, lattice parameters of new alloys are frequently unknown, being necessary to use parameters of similar alloys, which could lead to errors.

Deformed or fine-grained materials are also more difficult to be analyzed by EBSD. Such materials produce patterns of lower quality due to a resolution limitation associated to the size of volume interaction and the fine scale of the structure (WRIGHT et al., 2015). The electron beam would no longer interact with a single and perfect crystal lattice, but with a set of lattices derived from different grains and/or slighter differences in orientation caused by dislocations. In this case, the EBSP obtained is a superposition of various individual patterns (WRIGHT; NOWELL, 2006b). The use of a field emission gun electron microscope is recommended for such materials, since the electron beam diameter is smaller than other microscopes.

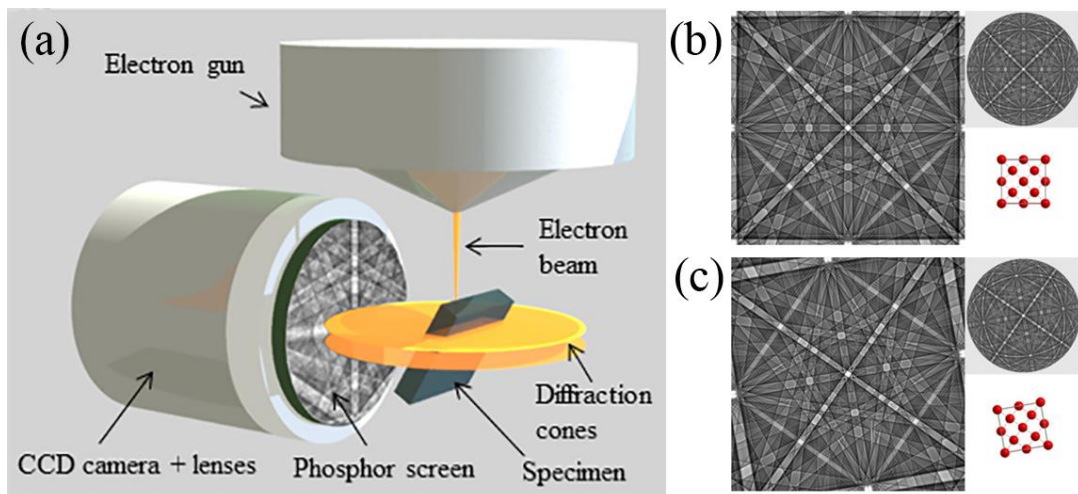


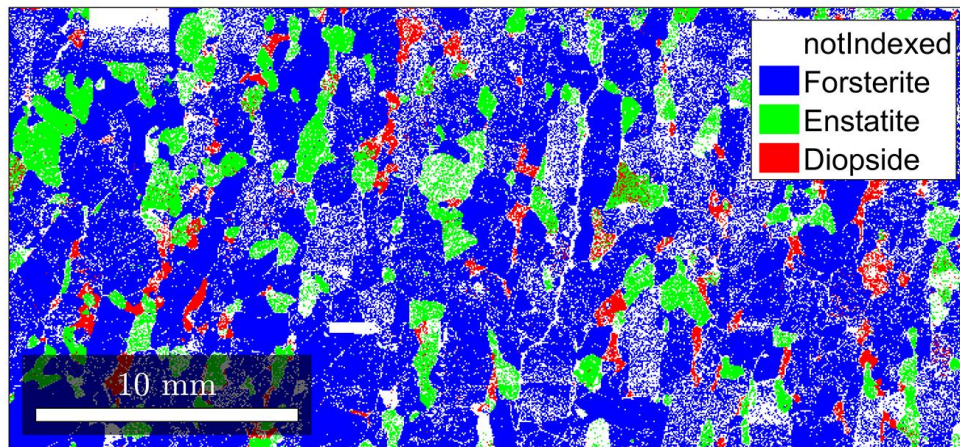
Figure 5: (a) EBSD experimental setup and (b, c) examples of Kikuchi patterns for different crystal orientations. Adapted from (TRAGER-COWAN, 2012)

Apart from crystalline imperfections, sample preparation and surface contamination also may affect the quality of EBSPs obtained. To obtain the best pattern quality, the specimen's surface should be free of deformation and very clean, since the backscattered electrons are originated from a depth of only 30-40 nm below surface (SUWAS; RAY, 2014). Even the surface deformation caused by mechanical polishing could be a problem. The quality of EBSPs is measured by a property called band contrast (BC), derived from the Hough transform.

It is important to note that the band contrast is not a direct indication of the pattern indexing confidence level. Even if the EBSP has a good quality, it may not fit well the simulated EBSPs of candidate phases informed by the user. The property that measures the quality of indexing is the mean angular deviation (MAD). The MAD is defined as the angular misfit between experimentally detected and simulated Kikuchi bands.

An EBSD map may show different properties, such as phases, crystal orientation and band contrast (BC). BC maps are generally gray scale maps from black to white, where darker shades represent worse EBSP quality and lighter shades indicate better EBSP quality. Since the band contrast of grain boundaries present poor quality, BC maps are often used to reveal grains. Figure 6 shows examples of an EBSD phase map and a BC map.

## (a) Phases



## (b) Band contrast

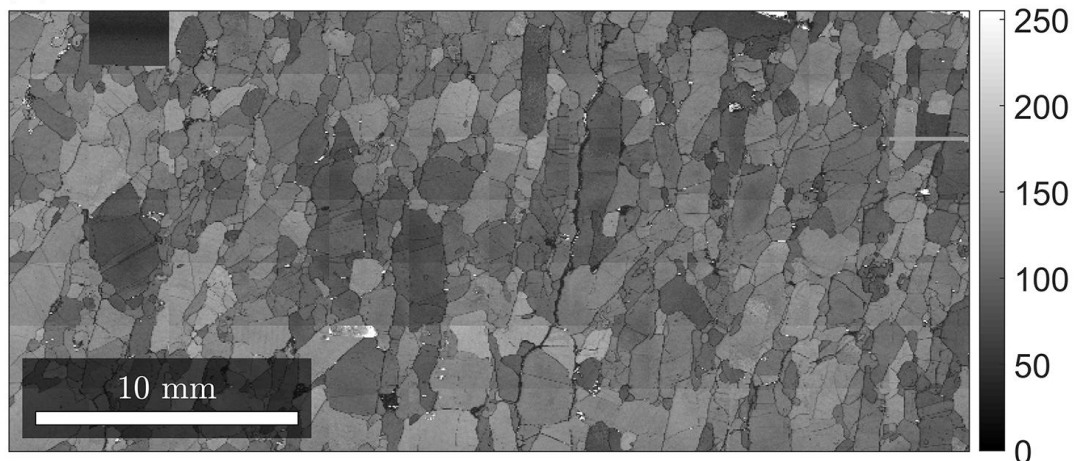


Figure 6: Examples of (a) phase map and (b) band contrast map for a mineral specimen containing three phases: forsterite, enstatite and diopside. Examples from MTEX MATLAB Toolbox (BACHMANN; HIELSCHER; SCHAEBEN, 2010).

EBSD maps may also represent crystal orientations. A method often used is the inverse pole figure (IPF) colored maps. First, a direction of the specimen reference frame is chosen, usually RD, TD or ND in the case of rolled specimens. Then, colors are used to represent the crystal direction that is parallel to the chosen specimen direction. Each color is assigned to a crystal direction of the fundamental sector of the inverse pole figure. Figure 7 shows the color codes for cubic and orthorhombic crystal symmetries. IPF colored maps are very popular

because they are simple to be interpreted. Figure 8-a presents examples of IPF colored maps, showing crystal directions parallel to the main specimen axes, X, Y and Z.

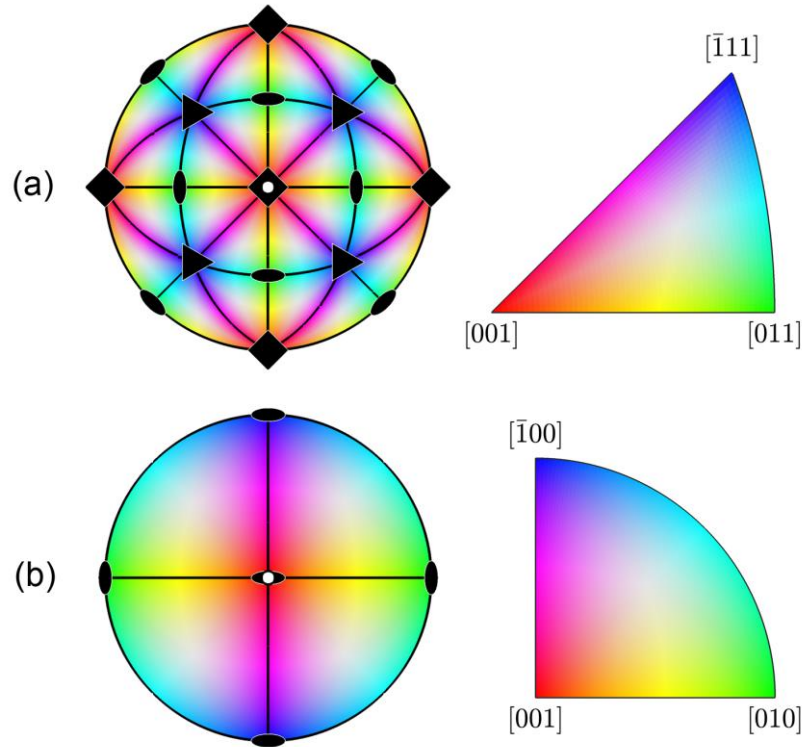


Figure 7: Color assignment to different crystal directions for (a) cubic crystal symmetry and (b) orthorhombic crystal symmetry. Constructed with MTEX MATLAB Toolbox (BACHMANN; HIELSCHER; SCHAEBEN, 2010).

Another form of representing orientations is by Euler colored maps, where colors are assigned to each crystal orientation, given by the three Euler angles. Figure 8-b show an example of Euler colored orientation map. Despite these maps are more complete, in the sense that it gives a full description of crystal orientations in only one map, it is also more difficult to be visually interpreted (NOLZE; HIELSCHER, 2016).

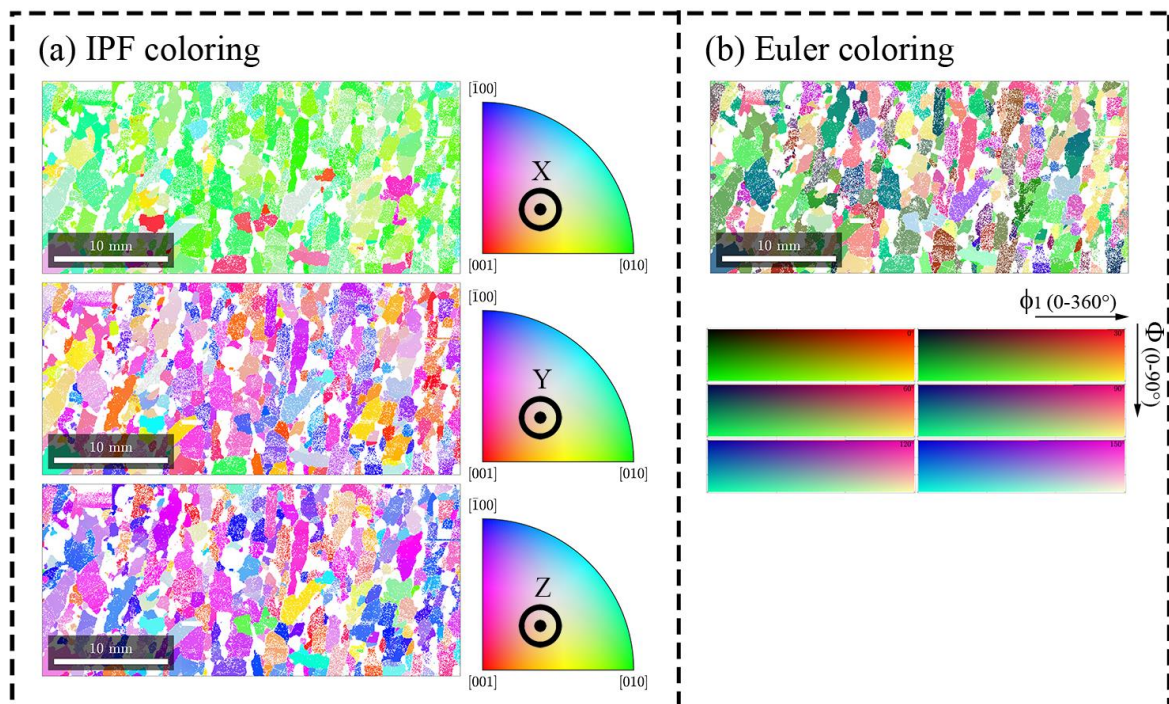


Figure 8: Examples of orientation maps for the forsterite phase: (a) IPF colored maps showing the crystal orientation aligned to X, Y and Z axes and (b) Euler colored maps. The forsterite phase has orthorhombic crystal symmetry and the specimen symmetry is triclinic. Examples from MTEX MATLAB Toolbox (BACHMANN; HIELSCHER; SCHAEBEN, 2010).

### 2.1.3 The orientation distribution function

Note that a XRD pole figure provides the distribution of a certain lattice plane (pole), but no information about crystal orientation is directly given. To obtain the distribution of crystal orientations, it is necessary to compare the information of at least two pole figures. The visual interpretation of a set of pole figures give us a qualitative information of texture. If one desire to quantify texture components and have a full description of crystal orientations, it is necessary to calculate the orientation distribution function (ODF) using a specialized computer software (HIELSCHER; SCHAEBEN, 2008). The ODF is a function that provides the volume percentage of crystals with a certain orientation.

The most common way to graphically represent an ODF is by plotting a three-dimensional graph, where the x, y and z axes are the three Euler angles ( $\phi_1$ ,  $\Phi$  and  $\phi_2$ ). The intensity of each orientation is indicated by colors that represent multiples of random distribution (m.d.r.), that is, how many times it is more intense than a material with uniform distribution of crystal orientations (not textured). To make its visualization easier, the ODF is frequently represented by two dimensional sections along one of the main axes. The Euler space symmetry vary depending on crystal and specimen symmetries. For a cubic crystal and orthotropic specimen, for example,  $\phi_1$ ,  $\Phi$  and  $\phi_2$  may be limited to angles from 0 to 90°, since other angles are crystallographically equivalent. For a orthorhombic crystal and orthotropic specimen,  $\phi_1$  and  $\Phi$  vary from 0 to 90°, whilst  $\phi_2$  vary from 0 to 180°. Figure 9 shows two examples of ODFs of “ideal” texture components, represented in the Euler space.

Although EBSD measurements directly provide the orientation of crystals, it is also possible to calculate the ODF from a EBSD map. So, the volume fraction of a texture component may be calculated directly from the EBSD data or from the calculated ODF.



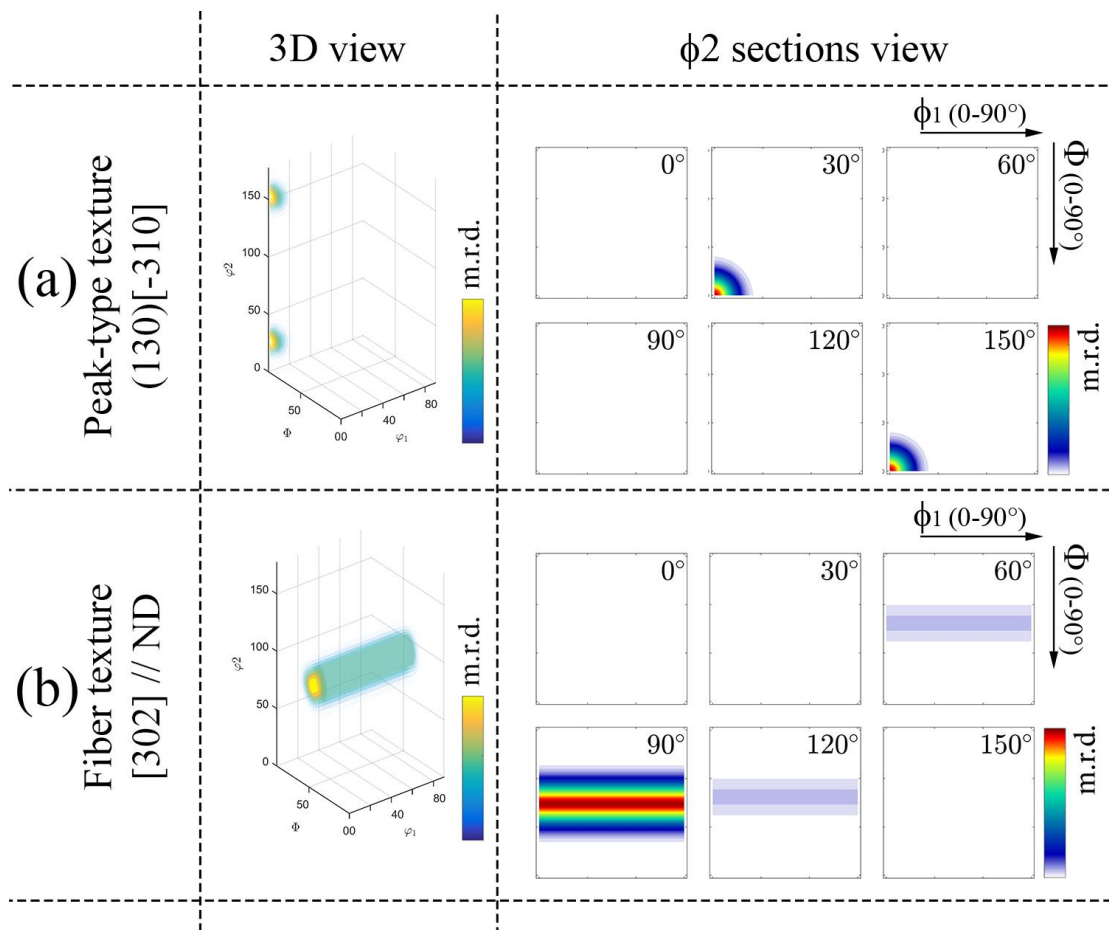


Figure 9: Examples of orientation distribution functions of two ideal texture components: (a)  $(130)[-310]$  peak-type texture component and (b)  $[302]//ND$  fiber texture component, represented in the Euler space for orthorhombic crystal and orthotropic specimen symmetries. Created with MTEX MATLAB Toolbox (BACHMANN; HIELSCHER; SCHAEUBEN, 2010).

Once the ODF has been estimated, it is possible to calculate the pole figure of any lattice plane or direction from the ODF data. To verify the quality of ODF estimation from XRD pole figure data, the most practical and reliable method is to recalculate the same pole figures that were measured experimentally and compare them. A good match between experimental and recalculated pole figures indicates a good ODF quality. In the case of such pole figures do not present a good match, it is possible that experimental pole figures were not correctly measured or the parameters chosen to estimate the ODF are not adequate.

## 2.2 Titanium alloys

### 2.2.1 Titanium phases

Titanium alloys offer high specific strength, excellent corrosion resistance and good biocompatibility. These characteristics make titanium alloys an excellent choice for the aerospace sector and medical engineering (LEYENS; PETERS, 2003). Figure 10 shows the isomorphous titanium phase diagram as function of the amount of  $\beta$  stabilizer elements. Pure titanium present two allotropic forms. The first is the hexagonal (HCP)  $\alpha$  phase, stable up to 882.5°C. Above this temperature, titanium transforms to its second allotropic form, the body-centered cubic  $\beta$  phase. Some alloying elements like aluminum, oxygen, nitrogen and carbon act as  $\alpha$  phase stabilizers. Others, like molybdenum, vanadium, niobium, iron and nickel are  $\beta$  phase stabilizers. Some elements are neutral, like zirconium (FROES, 2015; LÜTJERING; WILLIAMS, 2007).

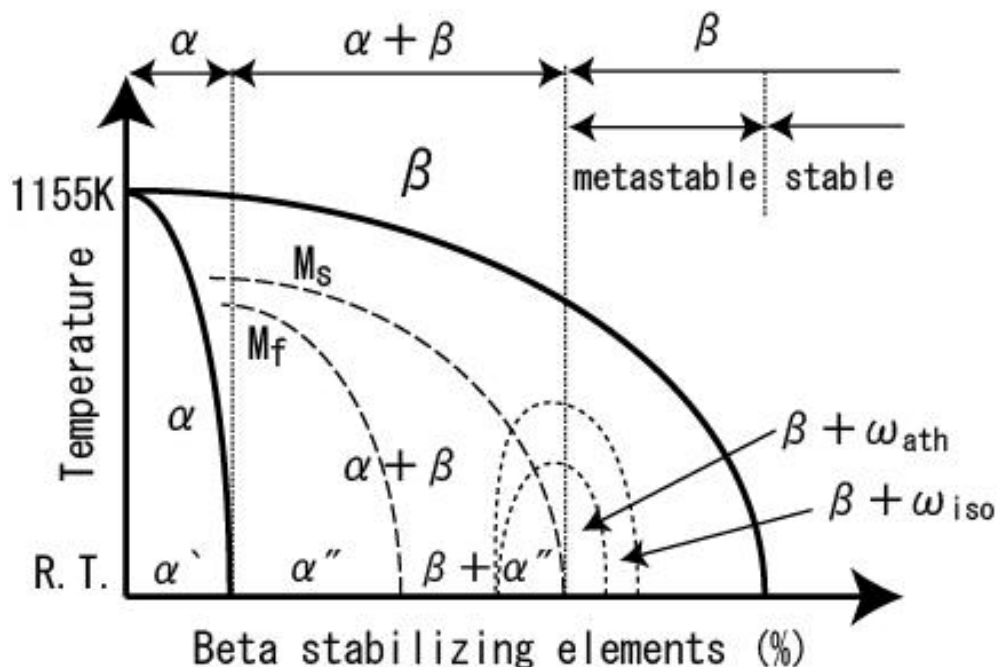


Figure 10: Isomorphous titanium phase diagram. Adapted from (GEPREEL, 2013).  $M_s$  and  $M_f$  are martensite start and finish temperatures, respectively.

When quenched from temperatures above the  $\alpha/\beta$  transition, the  $\beta$  titanium phase may undergo a martensitic transformation. This kind of transformation involves the movement of atoms by a shear type process. There is no diffusion of atoms and consequently the new phase present the same composition of the parent phase. The martensitic structure in titanium alloys have the geometry of plates or disks (LÜTJERING; WILLIAMS, 2007) that may have the appearance of needles when seen in 2D micrographs. The martensitic phase formed may be of two different types, depending on the alloy composition. For lower amounts of  $\beta$ -stabilizer elements, the  $\alpha'$  hexagonal martensite is formed. For higher amounts of  $\beta$  stabilizer elements, the  $\alpha''$  orthorhombic phase is formed instead (D'YAKONOVA; LYASOTSKII; RODIONOV, 2007). The orthorhombic martensite may be considered a distorted version of the hexagonal martensite.

The orthorhombic titanium and its parent cubic phase obey the following Burger's orientation relationship:  $(-110)_\beta // (001)_{\alpha''}$  and  $[111]_\beta // [110]_{\alpha''}$ . Figure 11 shows a schematic illustration showing the lattice correspondence between the cubic and orthorhombic titanium phases. As the cubic structure is more symmetric than the orthorhombic structure, six different orientations of  $\alpha''$  may be originated from a single  $\beta$  crystal.

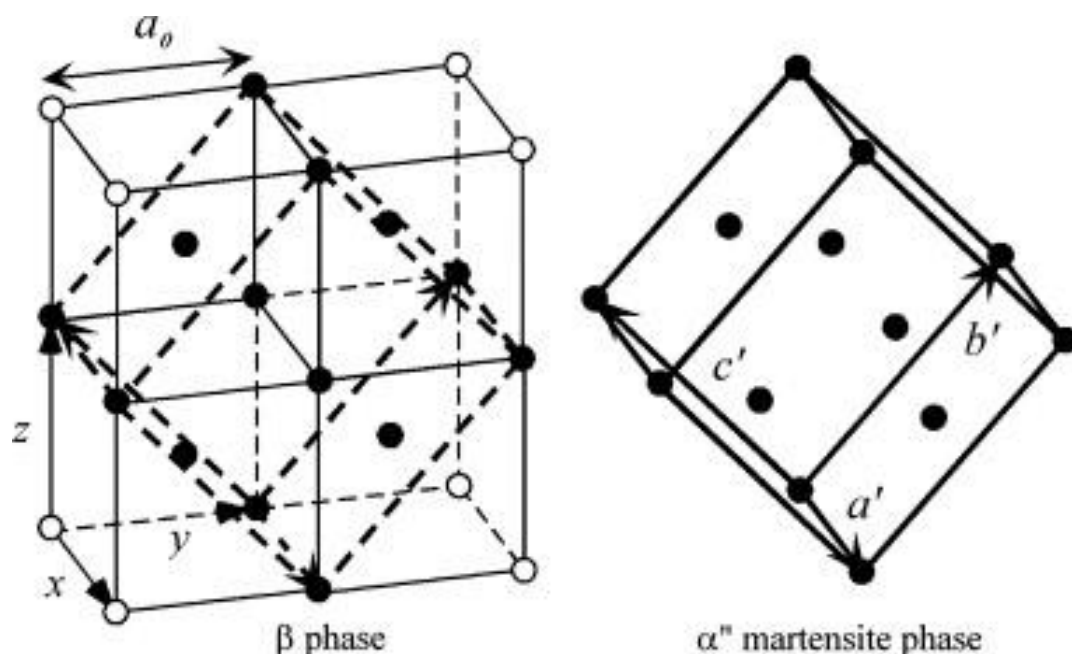


Figure 11: Schematic illustration showing the correspondence between the cubic and orthorhombic titanium phases. From (KIM et al., 2006).

If an even greater quantity of  $\beta$  stabilizer elements is added, the martensitic transformation start temperature ( $M_s$ , indicated by a dashed line in Figure 10) drops to below room temperature. In this case, the resulting quenched specimen will be composed by only metastable  $\beta$  phase. Titanium alloys may present another phase called  $\omega$  phase, generally undesirable because it is too brittle. It is a metastable phase formed in alloys with relatively high contents of  $\beta$  stabilizer elements. This phase may be formed during quenching, called athermal  $\omega$  phase, or during ageing of solution and quenched material, called isothermal  $\omega$  phase (HICKMAN, 1969).

The Ti-30Nb-4Sn alloy was first studied by LOPES (2009). A recent study of SALVADOR et al. (2016) has shown that in the Ti-30Nb-4Sn alloy the  $\omega$  phase formation is suppressed by the addition of 4wt-% Sn.

Beta ( $\beta$ ) Titanium alloys have relatively lower elastic modulus compared to other commonly used metallic biomaterials like 316L stainless steel (200 GPa), Co-28Cr-6Mo (210 GPa) and Ti-6Al-4V (110GPa) (CALLISTER, 2000; LUTJERING; WILLIAMS, 2007; NAG; BANERJEE, 2012). While pure titanium has a modulus of about 110 GPa (LIU; CHU; DING, 2004), some Ti-Nb, Ti-Mo and other beta alloys can reach values as low as 50 GPa (ALMEIDA et al., 2012; BRAILOVSKI et al., 2011; CARDOSO et al., 2014; CORREA; KURODA; GRANDINI, 2014; HO et al., 1999; KENT; WANG; DARGUSCH, 2013; POPA et al., 2014; SAKAGUCHI et al., 2005; ZHOU; NIINOMI; AKAHORI, 2004). This is considered a biomechanical advantage when used as implants for replacement of hard tissues like bones. One of the main problems with using metallic implants for bone replacement is their relatively high elastic modulus. The stiffness of the prosthesis must be as close as possible to that of the replaced tissue in order to reduce the stress shielding effect (DE VITERI; FUENTES, 2013). According to Wolff's law, the bone remodels itself in response to the load exerted on it and its density may be reduced (osteopenia) if not properly stimulated (OSHIDA, 2013). This phenomenon could be minimized if the prosthesis were made of alloys with Young's modulus closer to that of bone (10-40GPa) (NAG; BANERJEE, 2012).

The elastic modulus of titanium alloys strongly depends on their phases. Lee et al. (LEE; JU; LIN, 2002) studied Ti-Nb alloys with several different Nb contents. Considering the dominant phase obtained for each composition, they proposed the following sequence for the

elastic modulus of titanium phases:  $\omega > \alpha > \alpha' > \alpha'' > \beta$ . In another study on Ti-Mo alloys, Ho et al. (HO et al., 1999) also suggested that  $\alpha''$  and  $\beta$  have lower Young's moduli than other titanium phases. For this reason, titanium alloys based on these phases are a good choice when low stiffness is required.

### 2.2.2 Texture in $\beta$ titanium alloys

In many applications, the stress applied on a piece is concentrated in a given direction. Since titanium phases have a crystallographic anisotropy of elastic properties, the elastic modulus of a polycrystalline alloy could be controlled in a specific direction by controlling the preferred orientation of grains.

Texture may also play an important role in implant biocompatibility. It is known that the less dense atomic planes have greater surface energy. Thus, the planes that are exposed on the specimen's surface may influence properties like wettability, corrosion and cell-material interactions (BAHL; SUWAS; CHATTERJEE, 2014). HOSEINI et al. (2014) showed that the planes on the surface have an influence on the chemical structure of the surface oxide film. The nature of this oxide film also influence the cell-material interactions.

HAYAMA et al. (2014) published a work about crystallographic texture evolution of a Ti-35Nb alloy after cold rolling. The alloy was composed of  $\beta$  and  $\alpha''$  phases. The authors found two texture components for the  $\beta$  phase: a (110) strong fiber and a (111) weak fiber. GEPREEL (2013) has performed an extensive study about texture tendency of cold rolled  $\beta$  titanium alloys and noted two main behaviors: (i) for single  $\beta$ -phase alloys, the (100)[110] component was likely to be formed and increased with  $\beta$ -phase stability, and (ii) for alloys with low  $\beta$ -phase stability other components also developed. CHEN et al. (2015) performed hot rolling of a  $\beta$ -Ti alloy (Ti-15Mo-3Al-2.7Nb-0.2Si) and reported that after 57% hot-rolling three texture components formed: (112)[110], (001)[100] and (111)[110]. After 84% of deformation, texture components became very weak. CUI et al. (2010) carried out cold rolling of a Ti-28Nb-13Zr-2Fe metastable- $\beta$  alloy. For less deformed samples (15%) they reported a strong (112)[110] component. With 30% of deformation they observed a (111)[110] component and

for the 50% deformed sample the texture changed to a strong (111)[112] and a weak (001)[110]. After 85% of deformation the (001)[110] component became the strongest one. MATSUMOTO et al. (2007) studied the development of texture in a Ti-35Nb-4Sn alloy containing  $\beta$  and  $\alpha$  phases and reported the following texture components: (211)[110] and (200)[110] for the  $\beta$  phase and (220)[001] and [200](010) for the  $\alpha$  phase.

### 2.3 Laser surface melting

The laser (acronym for Light Amplification by Stimulated Emission of Radiation) is a device that produce a very directional and intense light beam. Applications of lasers are many, from delicate eye surgeries to cutting of very “strong” materials. Lasers can also be found in many of our everyday products such as CD players and bar code readers (SILFVAST, 2004).

When the laser beam interacts with a metallic surface, a significant amount of light is reflected and a small portion is absorbed. The absorbed portion of light heats the metal. As the temperature increases, the surface absorptivity gets higher and the laser heating effect becomes more efficient (KANNATEY-ASIBU JR., 2009). If the temperature reached by the irradiated region is sufficiently high, the metal will be melted and possibly evaporated. This vaporization, in the case it occurs, creates a vapor cavity in the material. There are two different types of heating modes that lead to different shapes of the melt pool: the “conduction mode” and the “keyhole mode”.

The conduction mode occurs in processes with lower power densities, usually bellow  $10^6$  W/cm<sup>2</sup> (KANNATEY-ASIBU JR., 2009). In this mode, the substrate is heated by the laser beam up to its melting temperature, presenting little or no evaporation. The laser energy absorbed by the specimen’s surface penetrate in the metal by thermal conduction. The penetration depth will be dependent of the metal’s thermal diffusivity and laser interaction time (RIVA; LIMA; OLIVEIRA, 2009). When higher power densities are used, some amount of material is vaporized, forming a cavity (keyhole) containing vapor, plasma or both. Surrounding this cavity there is molten metal. The pressure inside the cavity balance the liquid pressure and

keep the cavity opened during the process. Figure 12 shows a schematic representation of conduction and keyhole laser melting modes.

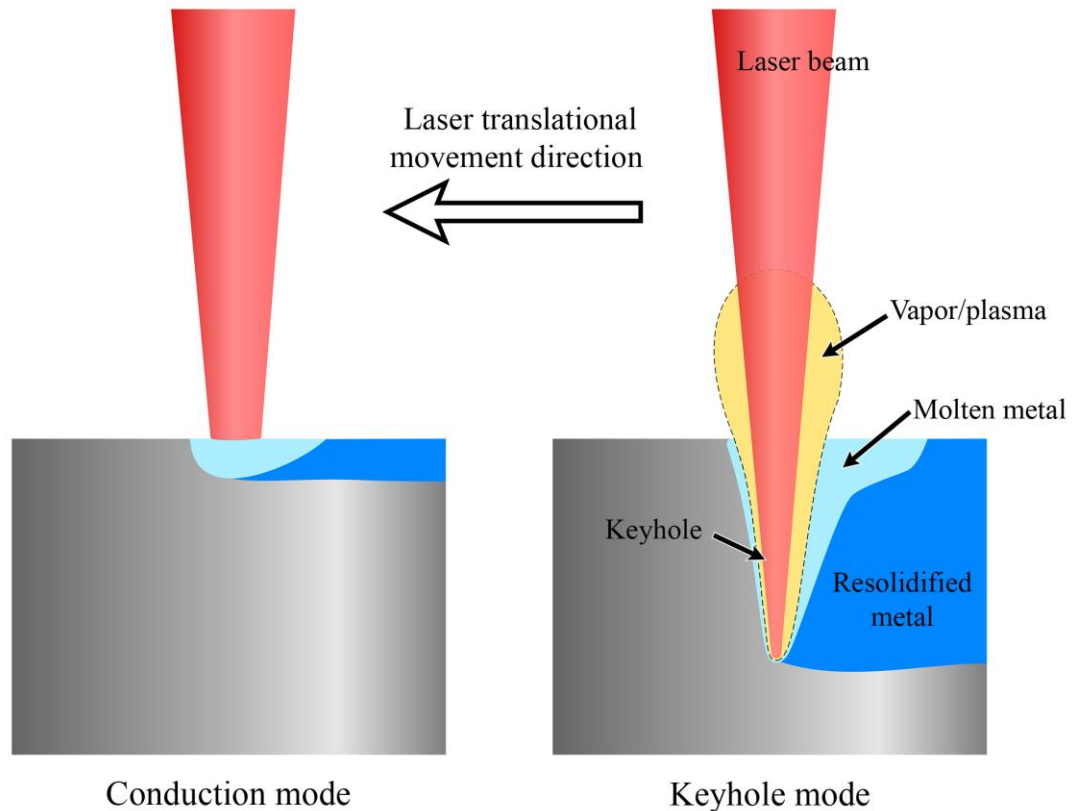


Figure 12: Conduction and keyhole laser melting modes.

In the keyhole mode, laser absorption is much higher than in the conduction mode. Additionally, the larger depth to width ratio of the melt pool is an advantage for most welding processes. However, instabilities of the cavity may lead to the formation of porosity caused by gas bubbles that are trapped inside the material after solidification. For this reason, the conduction mode is preferred for treatments in which penetration is not a concern.

Laser surface melting (LSM) is the irradiation of a laser beam over a metal surface with sufficiently power to elevate its temperature above the melting point. This treatment changes the surface layer characteristics, normally leading to a more refined structure (SUN; GUAN; ZHU, 2016). The main characteristic of any process involving laser melting, like welding or cutting, is that the highly-concentrated energy source provides rapid cooling during solidification and a small heat affected zone.

LSM technique has been subject of several relatively recent works. CANDEL et al. (2016) performed it on a sintered Ti-30Nb-2Sn alloy and showed that this technique is able to close the surface open porosity and minimize elastic modulus. LSM is also known as a method of increasing corrosion resistance of Mg alloys and steels, as described by SUN et al. (2016) and CONDE et al. (2000). This technique also provides improved wear rate for Ti-6Al-4V alloys, by increasing hardness and corrosion resistance due to the formation of passive oxide layers, according to the work of BALLA et al. (2014). Biomaterials used as implants can also benefit from the LSM technique. The surface roughness created on the material's surface is good for cellular attachment and consequently increase biocompatibility. Moreover, it is less time consuming and cleaner than other surface texturing techniques such as chemical etching and anodization, as pointed out by PRODANOV et al. (2011).

Laser surface alloying is a LSM related technique where additional elements are added to the specimen's surface during laser melting process, creating a surface layer with different composition that could give different properties to this region. The research group of Dr. João Batista Fogagnolo, at Unicamp, Brazil, have recently published two articles about this subject (FOGAGNOLO et al., 2013, 2016). They successfully obtained a stiffness graded material, with a surface layer 30% less rigid than the inner material, using commercially pure titanium as substrate and Nb as the added alloying element. A material with lower elastic modulus on its surface could, theoretically, have its fatigue life improved by reducing the stress on the surface, where cracks usually originate.



### **3 EXPERIMENTAL PROCEDURE**

#### **3.1 Preparation of samples and chemical analysis**

Ti-30Nb-4Sn ingots were arc melted in a melting chamber using a copper crucible and a tungsten electrode. The obtained alloy was homogenized at 1000°C for 8h followed by water quenching at room temperature. The homogenized ingot was chemically analyzed in three different regions. The composition of the alloy was examined by X-ray fluorescence spectroscopy (XRF) (Rigaku RIX3100), while nitrogen and oxygen levels were evaluated using a gas analyzer (LECO-TC400).

The ingots were cold rolled, at room temperature, in multiple passes to avoid adiabatic heating. It was obtained samples with 24, 36, 51, 68 and 85% of reduction in thickness. One sample with 85% of deformation was heat treated at 800°C for 30 min to promote recrystallization and water quenched. This sample will henceforth be referred in this text as the 85%REC sample. All heat treatments were carried out in argon atmosphere to prevent oxidation.

#### **3.2 Microscopy**

All specimens were observed by visible-light microscopy (VLM) in order to verify changings after different degrees of deformation and after recrystallization. EBSD analysis was carried out only on the recrystallized (85%REC) specimen. After laser surface melting treatment (see section 3.5) on the 51%, 85% and 85%REC specimens, the fusion and affected zones were observed by both VLM and EBSD.

Specimens were prepared by grinding with SiC abrasive sandpaper up to 1200 grit, followed by polishing with diamond paste (9  $\mu\text{m}$ ) and final polishing with colloidal silica suspension (0.05  $\mu\text{m}$ ). A reflected light differential interference contrast (DIC) microscope was

used for VLM observation, using the Kroll's etchant to reveal microstructure. The grain size of the recrystallized sample (85%REC) was measured in accordance with ASTM E112 standard.

EBSD analyses were performed using three different microscopes:

- 1) ZEISS (AURIGA Compact) electron microscope equipped with a field emission electron gun and OXFORD EBSD system using AZtecHKL acquisition software, belonging to the Polytechnic University of Valencia, Spain;
- 2) ZEISS (EVO MA15) equipped with LaB6 electron gun and OXFORD EBSD system using Channel 5 acquisition software, belonging to the Faculty of Mechanical Engineering of the University of Campinas, São Paulo, Brazil;
- 3) FEI (QUANTA 400) equipped with field emission electron gun and OXFORD EBSD system using Channel 5 acquisition software, belonging to the Technological Research Institute (Instituto de Pesquisas Tecnológicas – IPT), São Paulo, Brazil.

For TEM analysis it was used a 200kV JEOL (JEM 2100F) microscope. Samples were prepared using Focused Ion Beam (FIB) technique.

### **3.3 X-ray diffraction**

The X-ray diffraction (XRD) analysis was performed in a PANalytical X'Pert PRO diffractometer equipped with a Cu-K $\alpha$  radiation source, belonging to the Faculty of Mechanical Engineering of Unicamp, Campinas, Brazil.

The pole figures of 51%, 85% and 85%REC samples were obtained with a Rigaku X-ray diffractometer (Cu-K $\alpha$  radiation source) equipped with a texture goniometer, belonging to the Nuclear and Energy Research Institute, IPEN–CNEN, São Paulo, Brazil. The Orientation Distribution Function (ODF) based on such pole figures was estimated as an attempt to better describe texture components and quantify them. The ODFs were calculated from DRX pole figure using the MTEX toolbox for MATLAB™ (BACHMANN; HIELSCHER; SCHAE BEN, 2010). The pole figure inversion method used to generate the ODFs is explained in detail by HIELSCHER and SCHAE BEN (2008).

### **3.4 Measurement of hardness and elastic modulus**

A G-200 nanoindenter from Agilent Technology (Santa Clara, USA) was used for the measurement of hardness (H) and elastic modulus (E). Specimen's surface was grinded and polished by the same method used for microscopy analysis. E and H were measured as a continuous function of depth of penetration, using the Continuous Stiffness Measurement (CSM) method (HAY; AGEE; HERBERT, 2010). It was used a constant maximum depth of 1500 nm and the value for each indentation was obtained as an average between 1000 and 1500 nm. A Berkovich-geometry tip was used and the indenter shape was previously calibrated by indenting a sample of fused silica with a known elastic modulus. Indentations were performed on sample cuts orthogonal to RD, ND and TD, always on regions near to the sample surface, where the deformation is more pronounced, and near to the central rolling line. At least twelve indentations were made on each area of interest.

### **3.5 Laser surface melting (LSM)**

Specimens in three different conditions (51%, 85% and 85%REC) were chosen for the laser surface melting treatment. The rolling surface of these samples was remelted by multiple overlapped beads, as exemplified in Figure 13. It was used an ytterbium fiber laser source with wavelength of 1070 nm and Gaussian beam. The distance between laser tracks was 175 $\mu$ m. Laser power was 150W and the laser focus was on the sample surface with a translational speed of 600mm/min. An argon flux (99.999 purity) of 15 liters per minute was applied over the irradiated area to remove plasma and fume that could potentially be formed during the melting process.

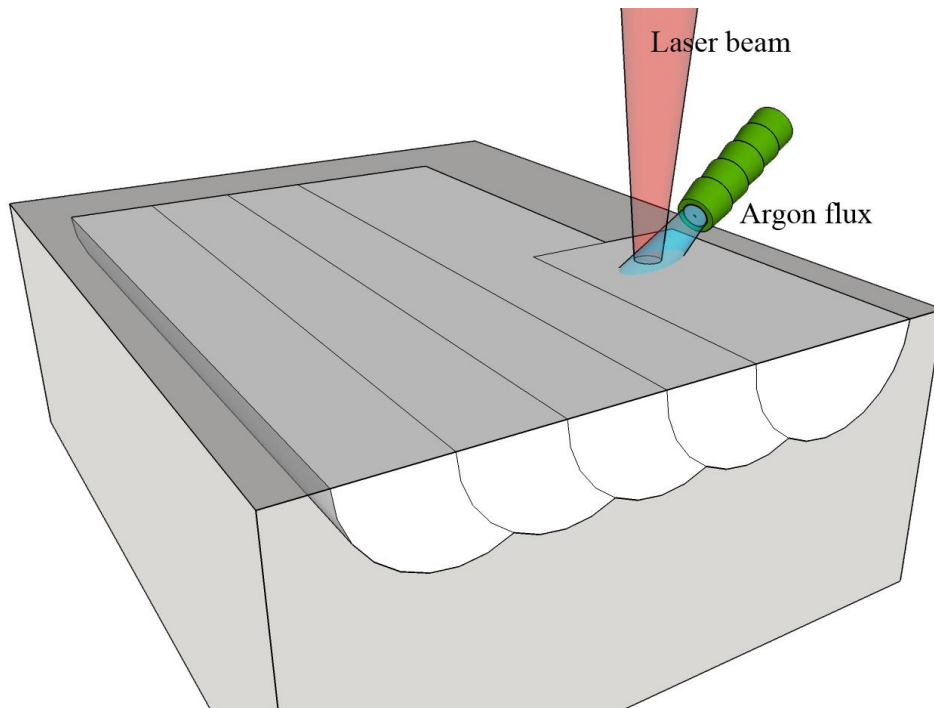


Figure 13: Laser surface remelting experimental schema.

The fusion and heat affected zones were characterized by the following techniques:

- Visible-light microscopy, for identification of microstructure,
- EBSD mapping for phase identification and microtexture analysis, and;
- Instrumented indentation (nanoindentation), for determination of hardness and elastic modulus of different regions affected by the laser treatment.

### 3.6 Experimental planning

Figure 14 describes the experimental procedure.

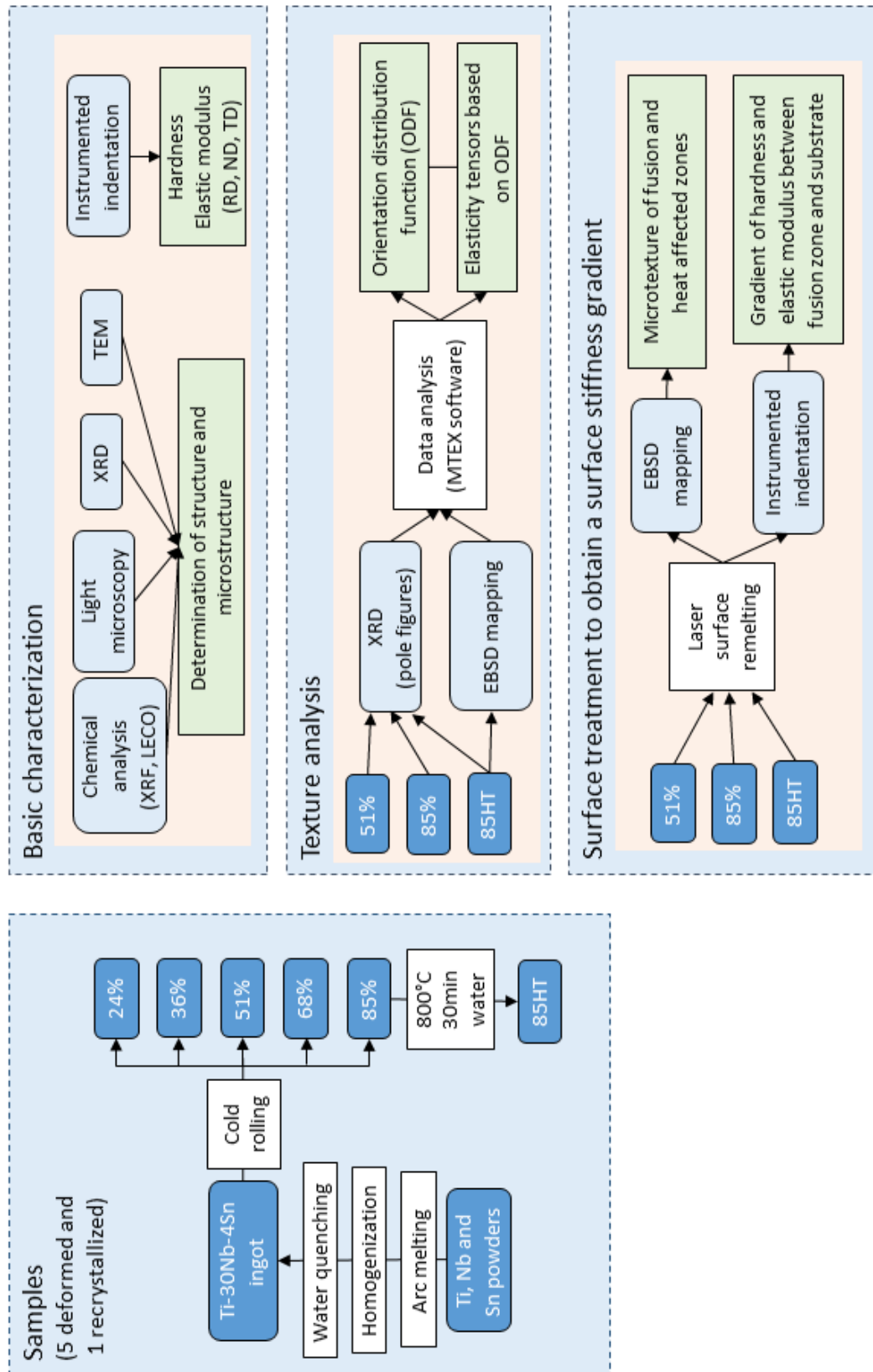


Figure 14: Complete experimental planning of this work.

## 4 RESULTS AND DISCUSSION

### 4.1 Initial characterization

#### 4.1.1 Alloy composition

The composition of the alloy determined by X-ray fluorescence spectroscopy (XRF) is described in Table 1. As can be seen, the Nb and Sn contents are very close to the nominal composition. Although there is no standard for maximum allowable oxygen and nitrogen levels for this class of alloy, the values obtained here can be considered low. The ASTM F67-06 standard for titanium grade 2 specifies a maximum of 0.25 and 0.03% for oxygen and nitrogen, respectively.

Table 1: Composition of the alloy determined by XRF.

Element	Nb	Sn	O <sub>2</sub>	N <sub>2</sub>	Ti
Content (in mass %)	29.2	3.9	0.13	0.0045	Balance
Std dev	0.2	0.1	0.004	0.00035	

#### 4.1.2 Microstructure and phase characterization of cold rolled and recrystallized specimens

Figure 15-a presents a micrograph of the 24% deformed sample, showing three grains with relatively large size. The grain in the center of Figure 15-a is also shown with higher magnifications in Figure 15-b,c,d. The martensite  $\alpha''$  laths in this grain seems to be “cut”, forming bands with approximately 45° to the rolling direction. This characteristic could be

related to some plastic deformation related phenomenon. Images of Figure 15-e,f show high magnification images of two other grains, also presenting a great amount of martensite laths.

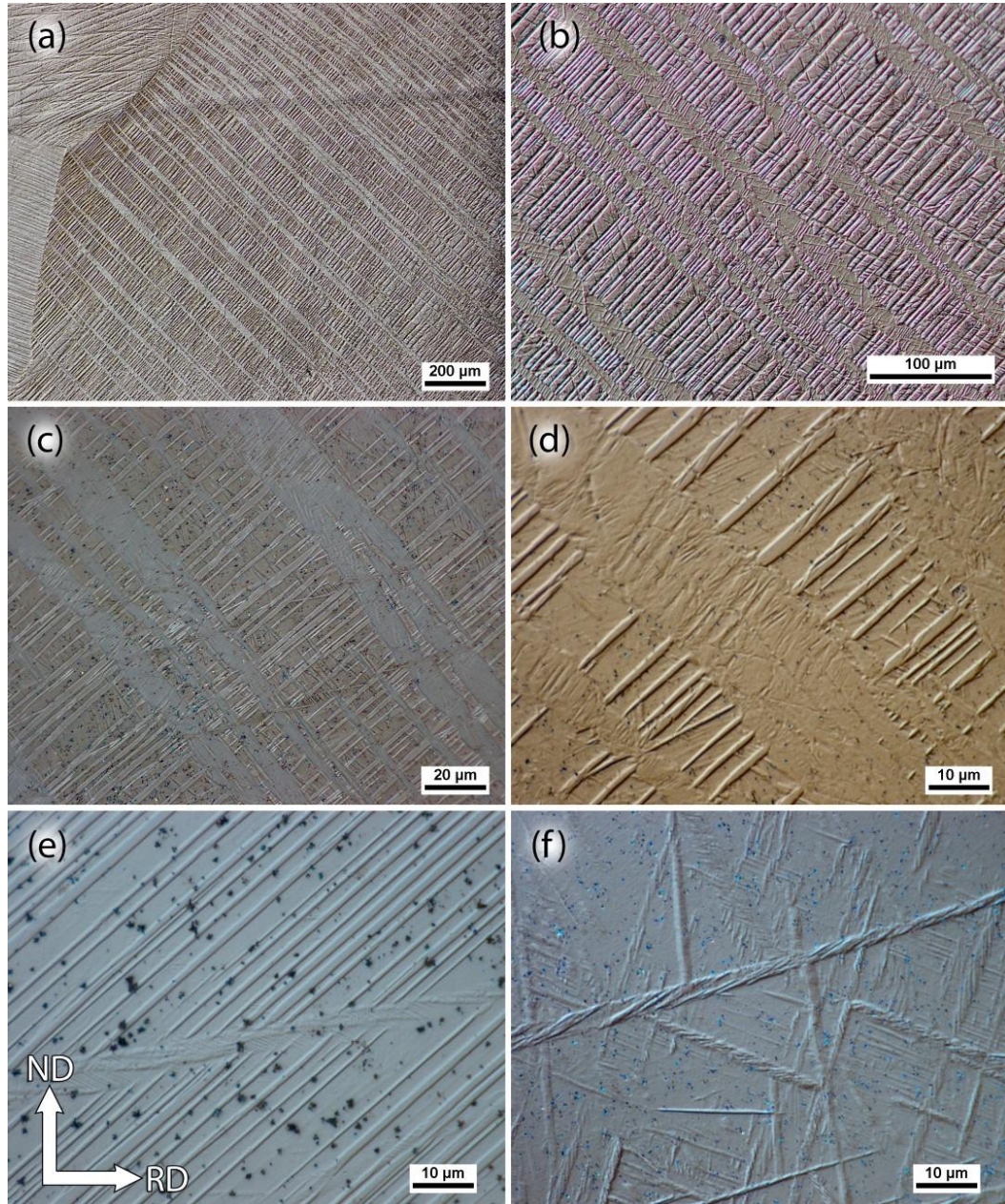


Figure 15: VLM images for a sample with 24% of deformation. (a, b, c, d) Images with different magnifications of the same grain and (e, f) details of other two grains.

The VLM images of samples with 36 and 51% of thickness reduction are depicted in Figures 16 and 17. Some grain boundaries can still be observed in Figure 16-a,b and Figure 17-

b,c. Some regions in the 51% sample show a wave-like pattern, as exemplified in Figure 17-a, that could be caused by deformation heterogeneities. Regions with higher deformation become harder and consequently the removal of material during sample preparation (grinding and polishing) is not homogeneous. In Figures 16-c,d and 17-c,d the martensite laths that are present all over the samples can be better observed.

The wave-like aspect becomes more intense in the micrographs of 68% and 85% samples (Figures 18 and 19). Grain boundaries can no longer be observed in these samples and some shear bands become visible (indicated by arrows). Shear bands are caused by intense localized slipping during plastic deformation. They form an angle of 30 to 60° to the deformation direction and may cross several grains. Despite the deformation mechanism that generates shear bands is not completely understood, they are normally seen in highly cold deformed metals with large grains (SANDIN, 2003).

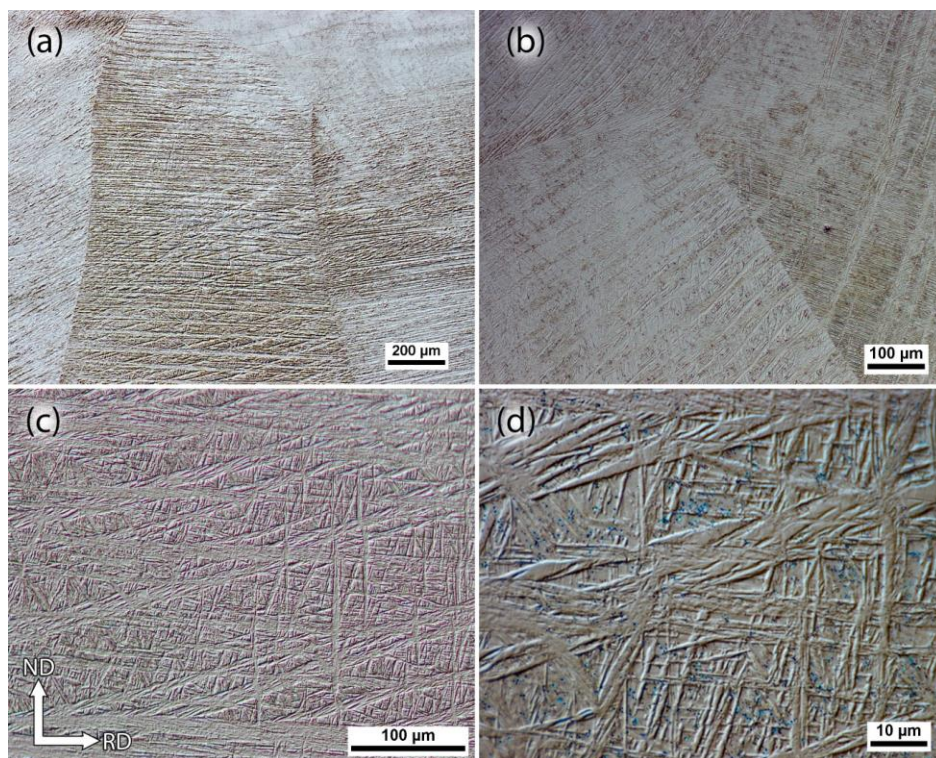


Figure 16: VLM images of a sample with 36% of deformation.



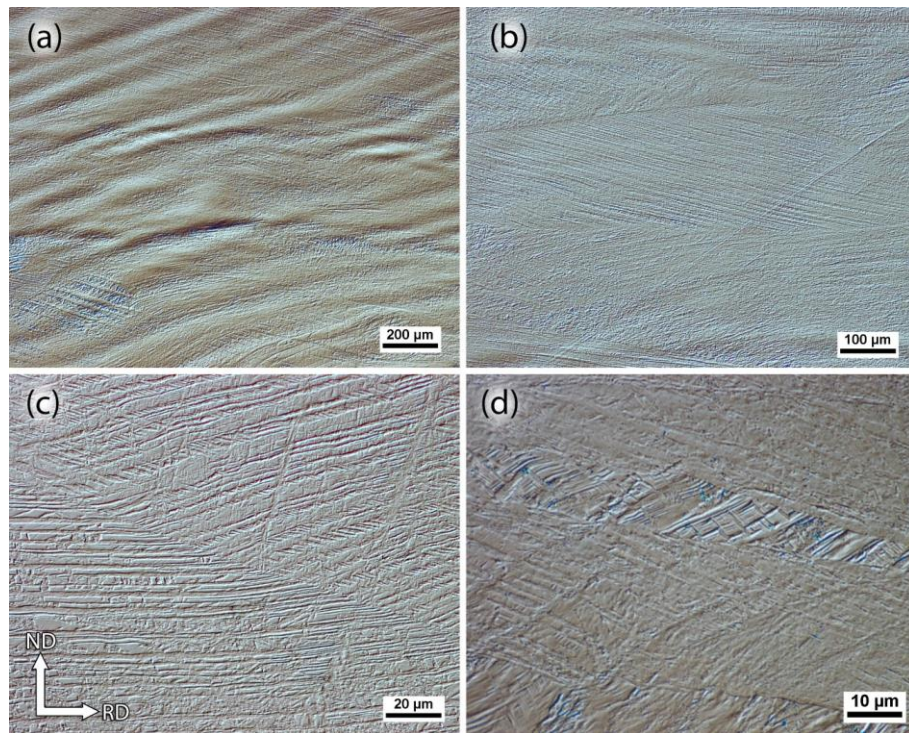


Figure 17: VLM images of a sample with 51% of deformation.

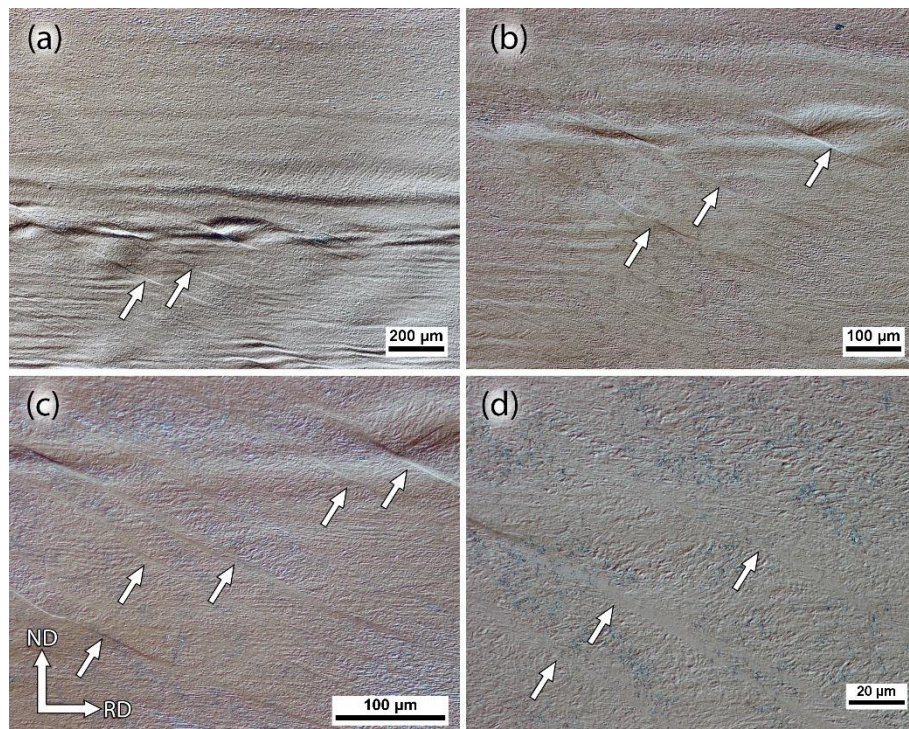


Figure 18: VLM images of a sample with 68% of deformation. Some shear bands are indicated by arrows.

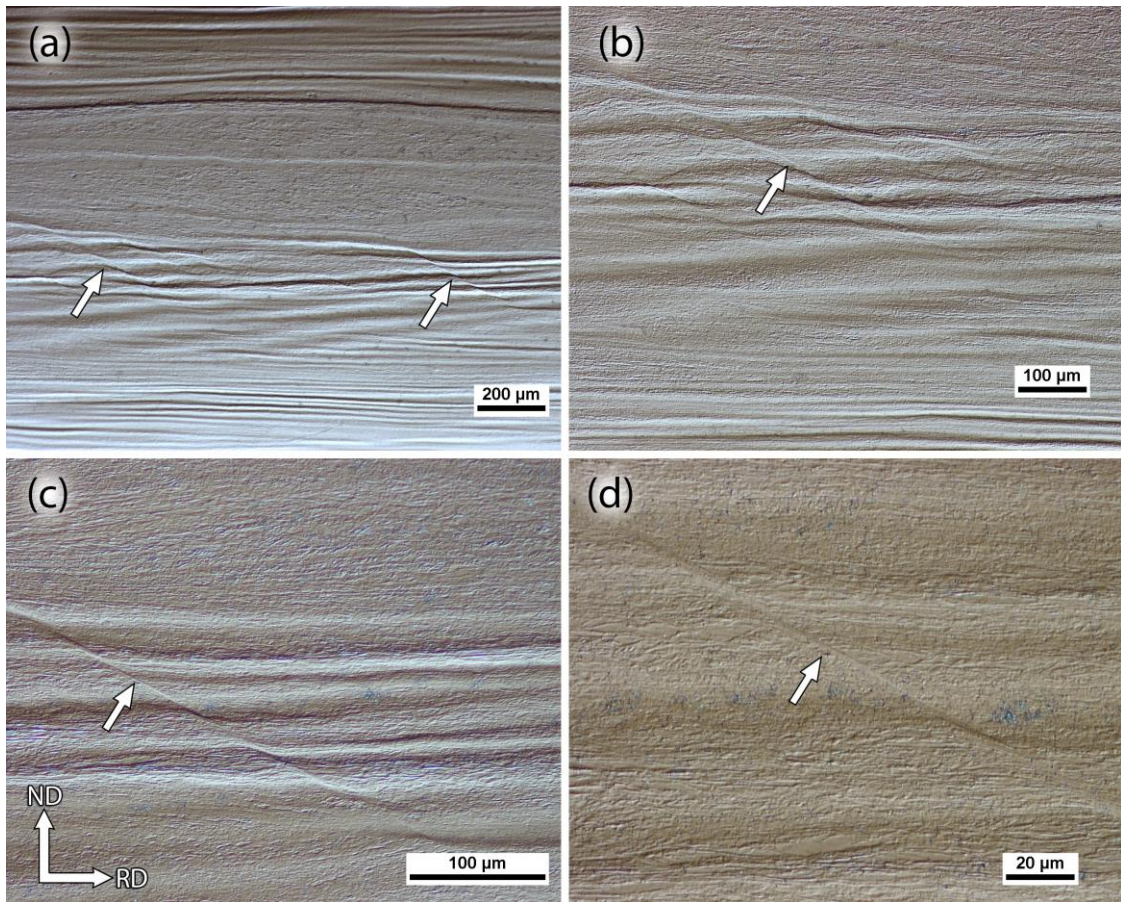


Figure 19: VLM images of a sample with 85% of deformation. Some shear bands are indicated by arrows.

Figure 20 shows the microstructure of the recrystallized (85%REC) sample, revealing a grain size of about  $37\ \mu\text{m}$  (ASTM grain size number 6.6). A high quantity of martensite laths is visible, as in the deformed specimens.

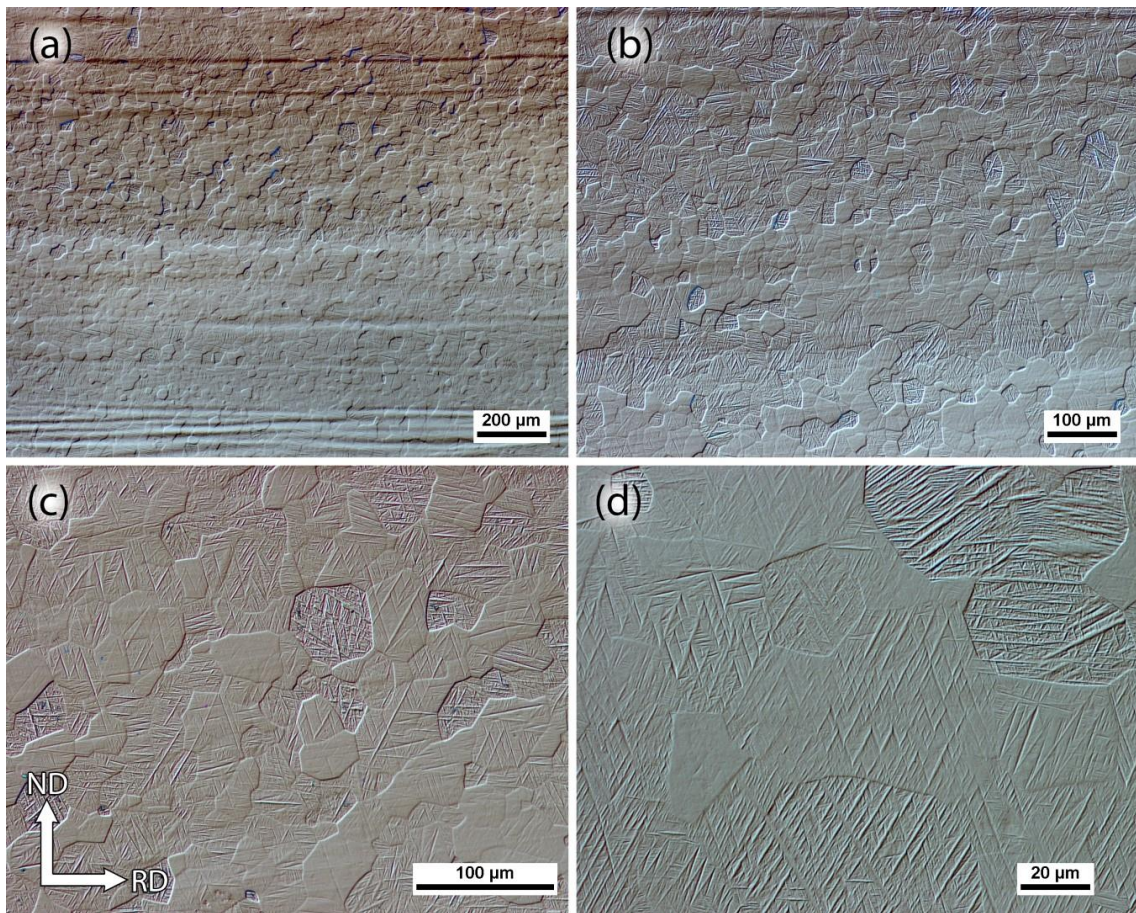


Figure 20: VLM images of the recrystallized sample (85%REC).

Figure 21 shows the XRD patterns of Ti-30Nb-4Sn alloy with different degrees of deformation and after recrystallization. Possible phases related to the observed peaks were determined using the standard peaks of  $\alpha''$  [JCPDS X-ray Powder Diffraction File No. 17-102] and  $\beta$  [JCPDS X-ray Powder Diffraction File No. 89-3726]. Previous works (MORAES et al., 2014; OZAKI et al., 2004) show that these phases are expected in the Ti-30Nb-4Sn alloy. The analysis did not reveal any  $\omega$  phase peak. The absence of XRD peaks related with  $\omega$  phase does not assure the absence of this phase. However, it has been reported that  $\omega$  phase precipitation is prevented by adding Sn to Ti-Nb alloys (SALVADOR, 2015), hence, this absence was expected.

As the main  $\beta$  phase peaks are overlapped by the  $\alpha''$  ones, the presence of  $\beta$  phase cannot be confirmed by these XRD patterns, while the presence of  $\alpha''$  is undoubtful. Hence, the martensite laths observed by VLM is the orthorhombic  $\alpha''$  martensite. MORAES et al.

(2014) reported the presence of  $\alpha''$  orthorhombic martensitic phase in a similar alloy. This phase is usually formed in the presence of a large amount of  $\beta$  stabilizer elements, but not sufficient to fully stabilize the  $\beta$  phase. For Ti-Nb alloys, this is the equivalent to approximately 13 to 36 wt.% of niobium (OZAKI et al., 2004).

The  $\alpha''$  phase is formed during rapid cooling, but it is known that this phase could also be induced by plastic deformation (FROES, 2015). So, the martensitic phase observed in the undeformed (FANTON et al., 2016) and recrystallized (Figure 20) samples are surely derived from quenching treatment. The deformed specimens (24% to 85%) may also contain some amount of martensite formed during cold deformation.

With increasing deformation, the XRD peaks became broader due to subgrain refinement and residual lattice distortion. The XRD pattern of the 85%REC sample revealed a change in the relative intensity of some  $\alpha''$  peaks, indicating a change in texture after recrystallization.

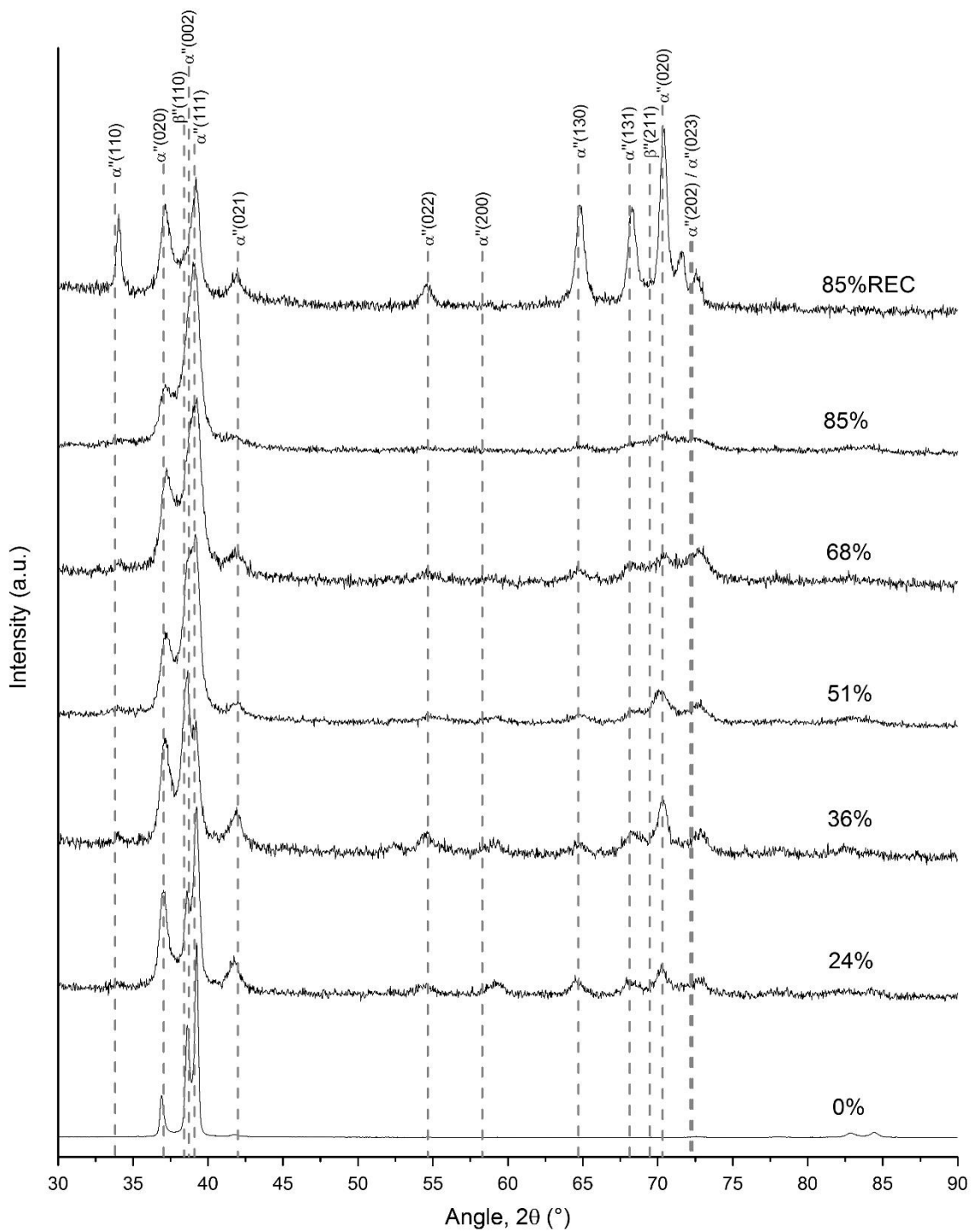


Figure 21: X-ray diffraction patterns for samples with 0% (FANTON et al., 2016), 24%, 36%, 51%, 68%, 85% of deformation and recrystallized (85%REC).

As the presence of  $\beta$  phase was not clear in the X-ray diffraction patterns, transmission electron microscope (TEM) was used to confirm it. Figure 22 shows a TEM bright field image

and its respective selected area diffraction pattern for a 24% rolled sample. The dark field image shows a martensite plate and the diffraction pattern confirm the presence of both  $\alpha''$  and  $\beta$  phases.

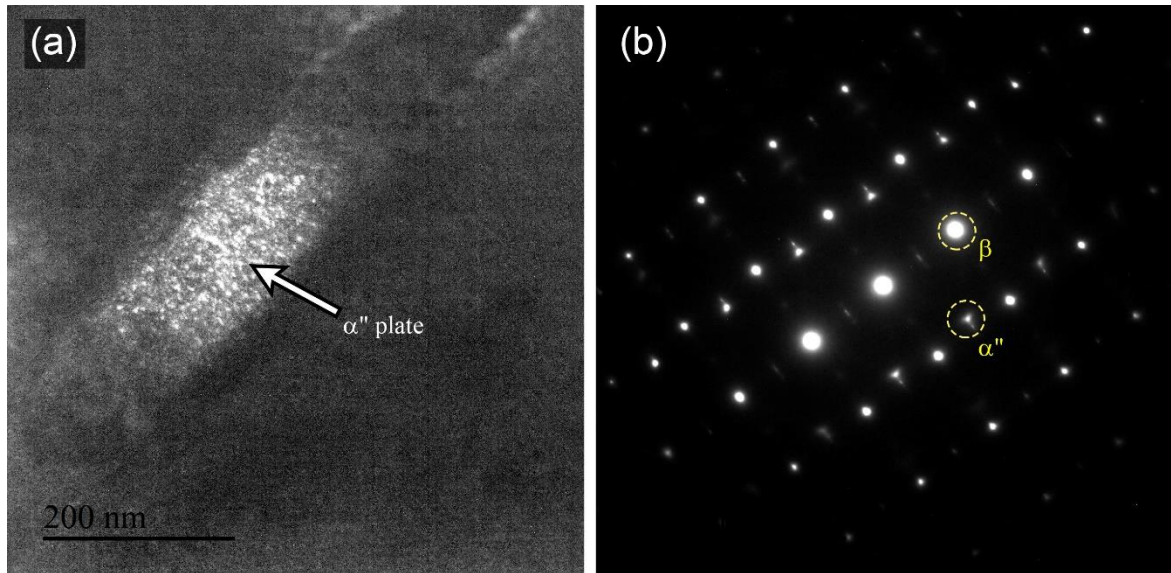


Figure 22: Transmission electron microscopy of the 24% deformed sample. (a) Dark field image and its (b) selected area diffraction pattern of  $[001]_{\beta}$  zone axis.

#### 4.1.3 Microstructure characterization of laser surface melted samples

Figure 23 shows some microstructure images of the 51% deformed and surface melted sample. Images from (a) to (f) are a sequence showing the microstructure evolution from the fusion zone, passing through the heat affected zone until the substrate. The region closer to the fusion zone have been recrystallized (Figure 23-a, b). The grain size of this recrystallized zone progressively decreases as the distance from fusion zone gets higher, until it becomes so small that grains can no longer be seen (Figure 23-b, upper part). This effect can be explained by the fact that the heat input is bigger close to the melted surface, facilitating diffusion and grain growth. As the distance from surface increases, it is observed a darker region that is apparently more sensitive to the etching reagent (Figure 23-c, d). On the farthest regions (Figure 23-e, f)

the material finally presents the characteristics of the substrate, indicating that the laser heat has no longer influence.

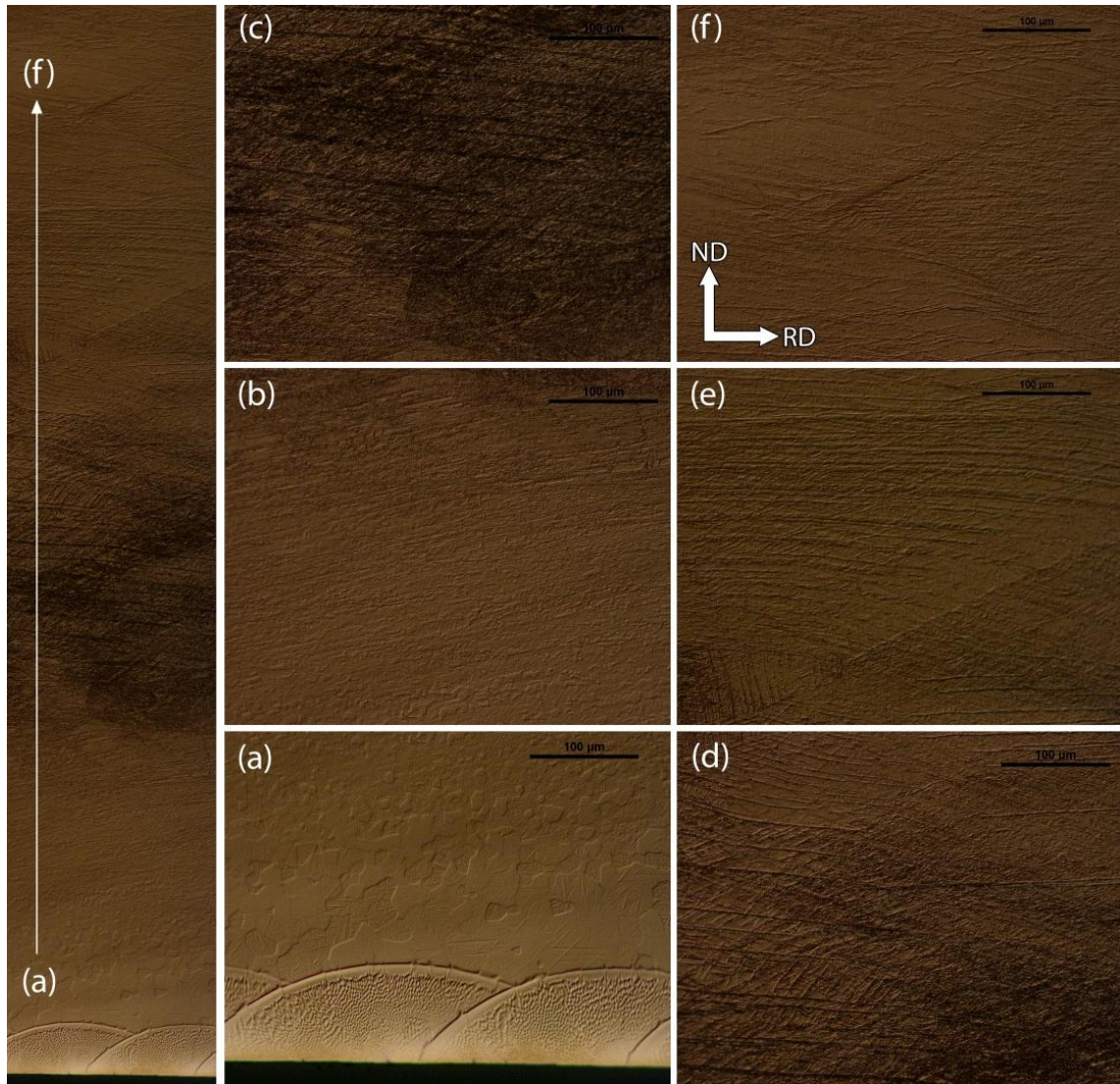


Figure 23: Visible-light microscopy images of the 51% deformed sample, showing the microstructure evolution from the fusion zone, passing through the heat affected zone until the substrate, sequentially from (a) to (f). The grains near to the fusion zone were recrystallized. Grain size of the recrystallized region progressively decreases as it gets farther from the fusion zone.

Micrographs of the 51% sample (Figure 24) show that some grains cross the interface between fusion and heat affected zones, revealing an epitaxial-type solidification of the fusion zone.

The solubility of niobium in titanium is greater in the solid phase than in the liquid, making titanium to be rejected during solidification process (LIU et al., 2009). Then, during the solidification of the fusion zone, the liquid closer to the solidification front is richer in titanium. As the distance from the solidification front increases, the liquid composition tends to stabilize, becoming homogeneous. The liquid ahead of the solid/liquid interface will present a constitutional undercooling caused by the gradient of composition in this region. This phenomenon make the solid/liquid interface unstable, giving rise to a cellular solidification process, as seen in the all micrographs of laser surface melted specimens. Note that there is no cellular structure at beginning of the fusion zone solidification, indicating that the destabilization of the solid/liquid interface takes some time to begin.



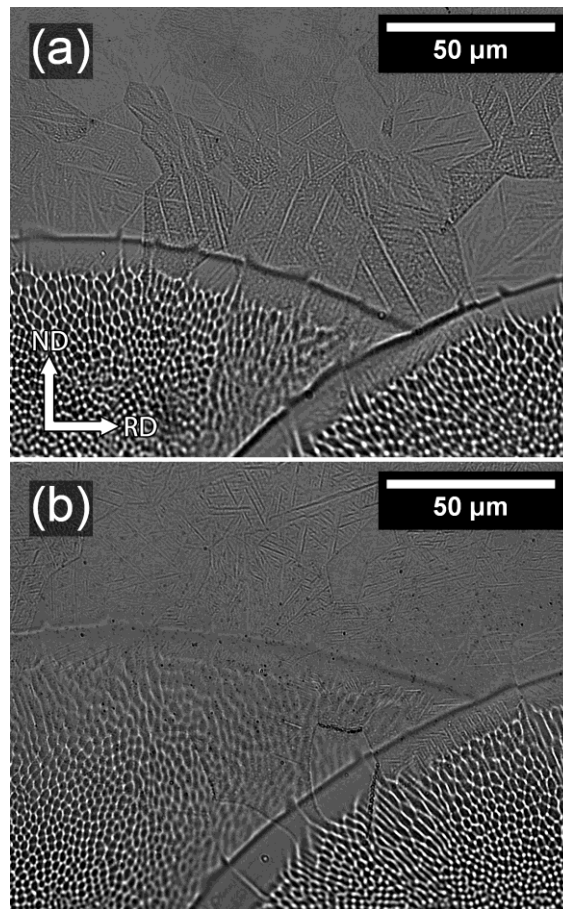


Figure 24: (a, b) VLM images of the fusion zone (FZ) and heat affected zone (HAZ) of the 51% deformed sample.

The characteristics observed in the micrographs of the 51% deformed sample are similarly observed in the micrographs of the 85% sample, as presented in Figure 25. Another region showing epitaxial growth can be readily observed in Figure 25-c.

The highly localized heat of the laser beam combined with a fast translational speed ensure the laser surface melting process to present high cooling rate. As  $\alpha''$  phase can be easily identified in all surface melted samples, we can conclude that the cooling rate was sufficiently high to activate the martensitic  $\beta \rightarrow \alpha''$  transformation, similarly to the water quenching treatment. The martensitic  $\alpha''$  phase present in the heat affected zone can be seen in all samples, especially in the micrographs with higher magnifications, such as the Figure 25-d. Although not so readily revealed by etching, the  $\alpha''$  phase can also be observed in the fusion zone, as shown in Figure 25-e.

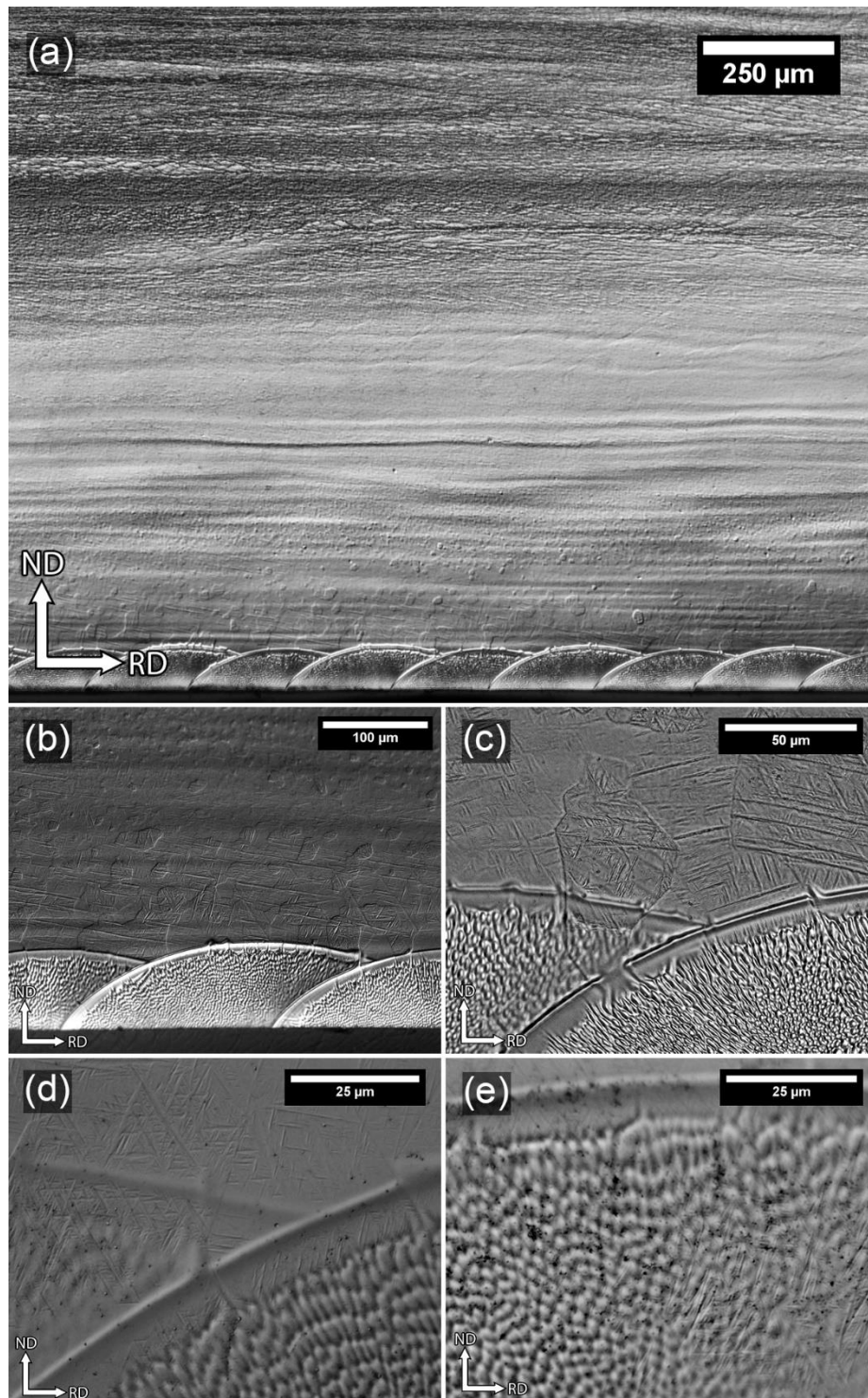


Figure 25: Fusion zone (FZ) and heat affected zone (HAZ) images of the 85% deformed sample. (a) General view of FZ and HAZ. (b) Grain size of the recrystallized region progressively decreases as it gets farther from the fusion zone. (c) Some grain boundaries cross the FZ/HAZ interface. (d, e) Martensite laths are observed in both HAZ and FZ.

The micrographs of Figures 26 present the fusion and heat affected zones of a recrystallized specimen. This sample showed a different feature after the laser surface melting: there are no apparent differences in microstructure between heat affected zone and substrate.

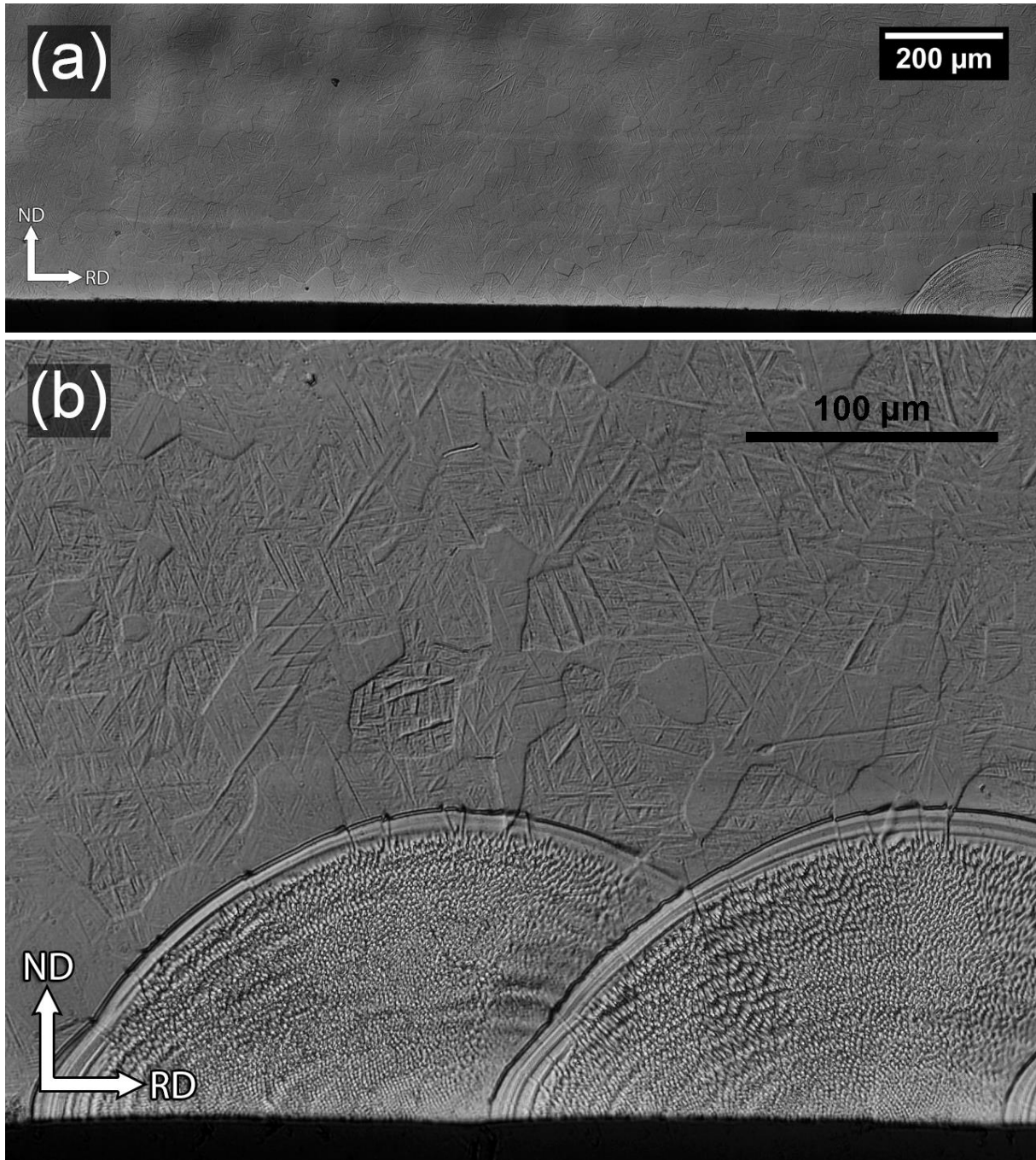


Figure 26: Visible-light microscopy images of the recrystallized (85%REC) sample. No difference is observed between heat affect zone and substrate.

The martensitic phase was easily observed using electron microscopy. Figure 27 shows forward-scatter detector (FDS) images of the 51% deformed sample. Martensite structures are seen all over the specimen, but some regions in the FZ and in the FZ/HAZ interface have lower amounts of martensite.

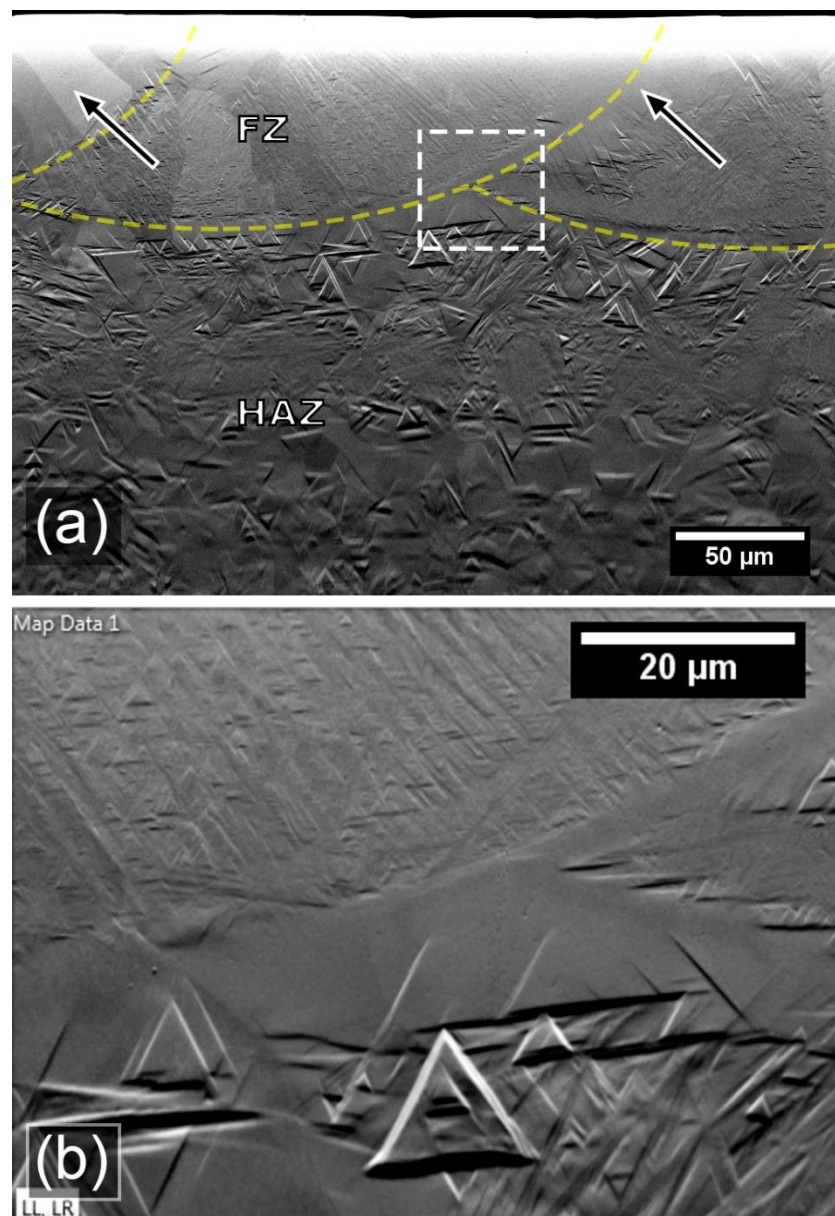


Figure 27: (a) FSD image of the 51% deformed sample and (b) region marked with a dashed square in (a). The dashed yellow lines indicate the boundaries between fusion zone (FZ) and heat affected zone (HAZ). Arrows indicate regions of the FZ with no martensite structure.

## 4.2 Evaluation of hardness and elastic modulus

### 4.2.1 General results

Nanoindentation measurements have been performed on RD, TD and ND cross sections of all deformed specimens and the recrystallized specimen (85%REC). In a recent published article (FANTON et al., 2016), it was measured hardness and elastic modulus of the same samples used in this work, using microindentation testing and pulse-echo ultrasound method, respectively. Figures 28 and 29 show the obtained values of nanoindentation hardness and elastic modulus, as well as the results from FANTON et al. (2016), for comparison purpose.

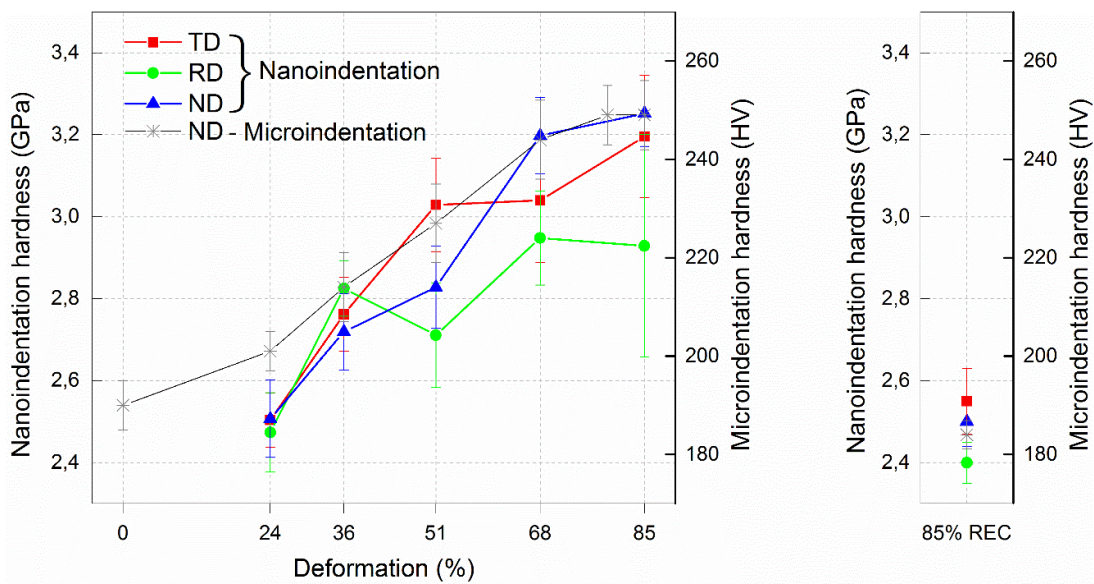


Figure 28: Hardness of deformed samples and recrystallized sample (85%REC), measured by nanoindentation on RD, ND and TD cross sections and by microindentation on ND direction (FANTON et al., 2016).

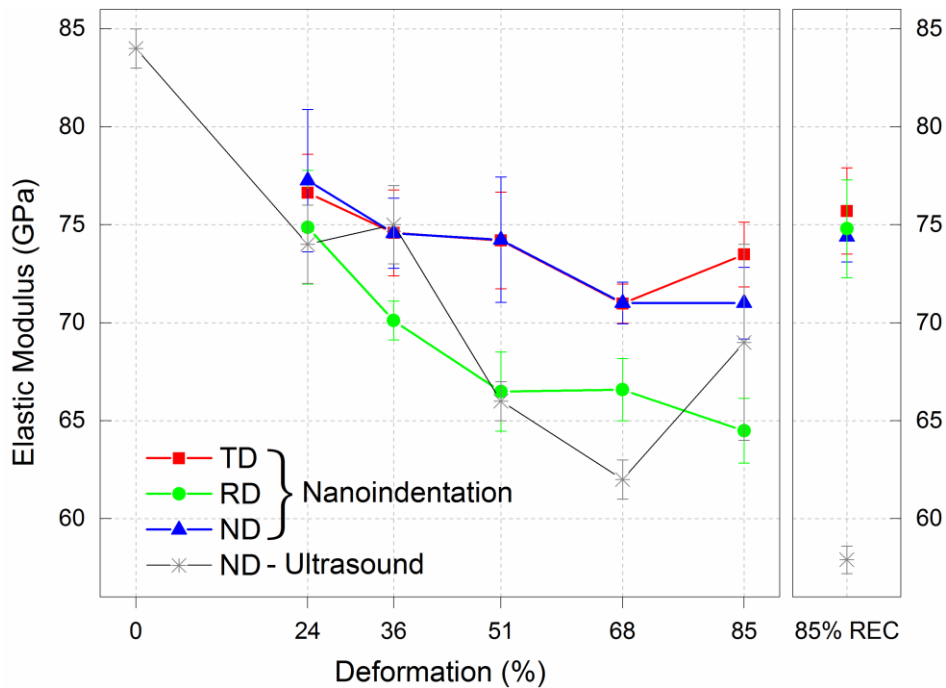


Figure 29: Elastic modulus of deformed samples and recrystallized sample (85%REC), measured by nanoindentation on RD, ND and TD cross sections and by ultrasound pulse-echo method on ND direction (FANTON et al., 2016).

As cold rolling deformation degree increases, hardness values rise due to work hardening. Elastic modulus, conversely, decreases as the deformation degree increases. For the recrystallized sample (85%REC), both hardness and elastic modulus returned to similar values of the less deformed sample.

With respect to differences in measurements made on different cross sections, some tendencies can be observed. For the less deformed sample (24%), the hardnesses measured on RD, TD and ND cross sections are very close to each other. Despite still being inside the measurement error, values seem to become more dissimilar at 36% and specially from 51 to 85% of deformation. A more pronounced anisotropy is observed for elastic modulus: RD cross section measurements present lower values than TD and ND, specially from 36 to 85% of thickness reduction. The elastic modulus and hardness of 85%REC sample show no significant differences between different cross section measurements.

Comparing the results obtained in this work using nanoindentation with the values found by FANTON et al. (2016) using ultrasound pulse-echo technique and microindentation, we see

a very similar tendency, except for a notable difference: the recrystallized sample showed a great decrease in elastic modulus. This contradiction will be discussed in section 4.4.

Nanoindentation tests were carried out for the analysis of hardness and elastic modulus of laser surface melted samples to obtain a profile of properties between fusion zone and substrate. Results are shown in Figure 30. The 51% and 85% deformed specimens may be divided in three different regions after laser surface melting: (i) the fusion zone, ii) the heat affected zone (mostly recrystallized), and (iii) the cold rolled substrate, unaffected by laser treatment. These samples presented the same overall tendency: hardness of fusion and heat affected zones has been reduced and the elastic modulus has been increased. For the recrystallized specimen (85%REC), it was not observed any difference neither in hardness nor in elastic modulus between the different affected zones.

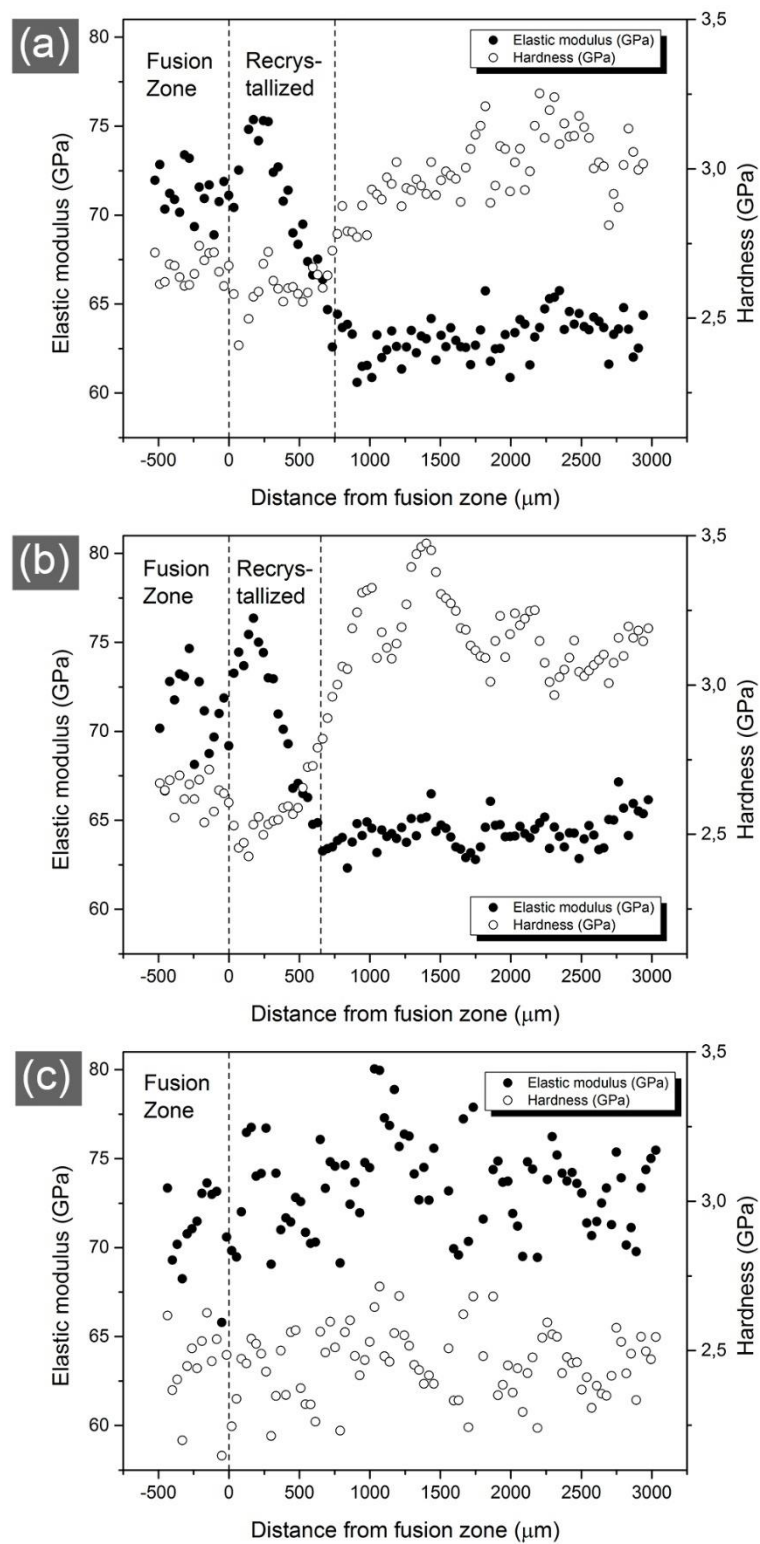


Figure 30: Nanoindentation measurements for the (a) 51%, (b) 85% and (c) 85%REC samples showing the values of hardness and elastic modulus relative to the distance from fusion zone.



#### 4.2.2 Factors that could be affecting elastic modulus and hardness

The increase of hardness proportional to the deformation degree is a well-known phenomenon that can be attributed to subgrain refinement, enhanced lattice distortion and increase in dislocation density. After recrystallization treatment, the defects introduced by cold deformation are eliminated, explaining why hardness of the 85%REC sample is comparable to that of the less deformed sample (24%).

The elastic modulus reduction after cold rolling has already been observed in other studies (HAYAMA et al., 2014; WANG et al., 2008; XU et al., 2012). This behavior can be associated to the increase in dislocation density and other crystalline defects during cold rolling process. The growth of crystalline defects such as dislocations and grain boundaries may increase the average interatomic distance and thus reduce the strength of atomic bonds, which in turn implies a reduction of elastic modulus. This phenomenon could also explain the increase of elastic modulus on the region treated by laser surface melting, since the crystalline defects introduced by cold working are eliminated in the fusion and recrystallized zones.

Apart from that, the formation of stress induced  $\alpha''$  phase during cold rolling was pointed out as a factor that could contribute to lower elastic modulus (WANG et al., 2008; XU et al., 2012). Both  $\alpha''$  and  $\beta$  are known as the titanium phases presenting the lowest elastic modulus in titanium alloys; but their precise relation is not yet clear. In the work of Lee et al. (LEE; JU; LIN, 2002) on the bending modulus of Ti-Nb alloys,  $\alpha''$  phase presented higher modulus than  $\beta$ . Thus, the possible formation of  $\alpha''$  phase during deformation does not seem to be the main cause of elastic modulus reduction.

Crystallographic texture is another important factor that could be affecting elastic modulus measurements (KOCKS; WENK; TOMÉ, 2000). Some studies successfully demonstrate that nanoindentation measurements are sensitive to crystal orientation (HAUŠILD; MATERNA; NOHAVA, 2014; RENNER et al., 2016; WANG; LU, 2016). However, some difficulties may be found. In the work of FIZANNE-MICHEL et al. (2014) it was carried out nanoindentation measurements on grains of commercially pure titanium with known orientation. While hardness was influenced by grain orientation, elastic modulus did not show

any clear correlation. For this reason, a detailed study of texture evolution seems to be important to satisfactorily explain what factors are really affecting elastic modulus and hardness measurements.

Finally, the dislocation structure formed during cold rolling could affect measurement made on different cross sections. As observed by LI et al. (2006), in many cases the crystallographic texture is not sufficient to explain the flow stress anisotropy observed in cold rolled specimens. Cold deformation creates a deformation microstructure with dense dislocation walls and microbands having a specific macroscopic orientation relative to the sample axes (HANSEN; JENSEN, 1992).

### **4.3 Crystallographic texture analysis**

#### 4.3.1 Texture of cold rolled and recrystallized specimens

##### *XRD texture analysis*

Most of the XRD peaks showed in Figure 21 fit the  $\alpha''$  phase pattern quite well. However,  $\beta$  peaks are not clearly distinguishable, i.e., some of them appear to be absent while others are possibly overlapped with  $\alpha''$  peaks. Despite it was confirmed by TEM the presence of both  $\alpha''$  and  $\beta$  phases, only texture of  $\alpha''$  was possible to be described by XRD. Some difficulties in creating pole figures by XRD can be found in multi-phase material analysis due to overlapping of peaks of different phases. Peak separation is frequently a laborious process, making it difficult or impossible to obtain the necessary pole figures to determine texture (ENGLER O., 2010).

Figure 31 shows the  $\alpha''$  pole figures obtained for the 51%, 85% and 85% heat-treated samples. The ideal location of some peak-type and fiber textures are indicated (even if it is not present), as it will be useful during discussion. It is important to remember that specimen

symmetry of rolled specimens is orthotropic, so each pole figure may be divided in four quarters that should ideally be symmetric.

The (130), (131), (022) and (020) pole figures of 51% deformed specimen (Figure 31-a) contain poles related to the (130)[-310] texture component. The (203)[010] component is seen in the (022), (200) and (131) pole figures.

For the 85% specimen (Figure 31-b), positions of poles are similar, with the difference that the (130)[-310] becomes visible also in the (200) pole figure.

In the pole figures of the recrystallized specimen (85%REC) (Figure 31-c), the (130)[-310] and (203)[010] texture components still fit the majority of poles. These components may be considered as maximums of partial fibers that are visible in the (200) and (022) pole figures.

Note that the ideal position of some poles related to the (203)[010] and (001)[410] texture components is on the borders of some pole figures ( $\alpha > 75^\circ$ ), where X-ray intensities are not measured. Also, the positions of poles for different texture components are very close to each other. The ODF estimation by computer software is much more sensitive to differences of intensities on a pole figure than our naked eye. For this reason, ODF calculation could make the identification of some components easier.

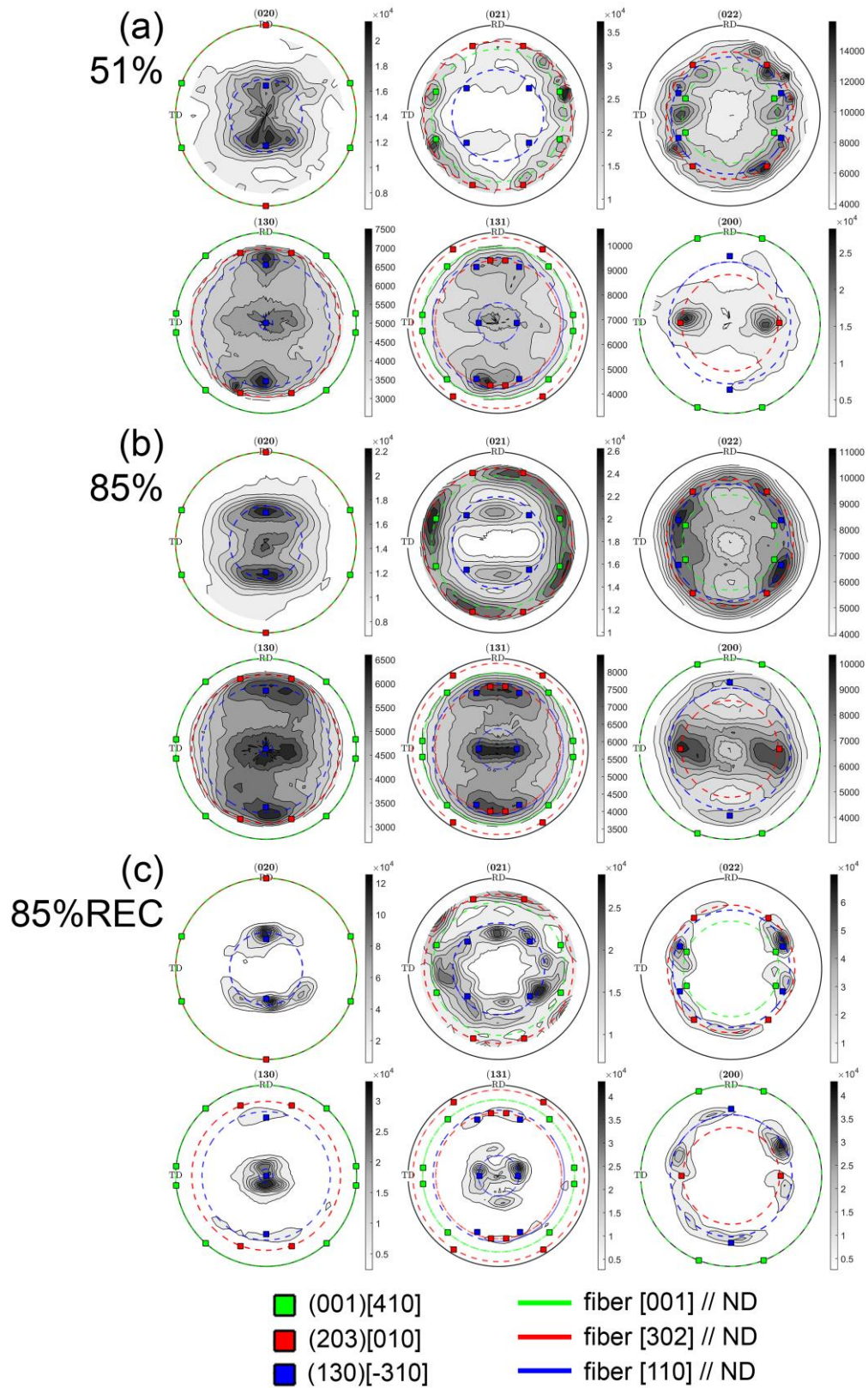


Figure 31: Experimental pole figures of the 51%, 85% and 85%REC samples. Scale bars are in arbitrary units.

As a guide to easier locate texture components in the ODFs that will be presented in this work, Figure 32 depicts the ideal location of some fibers and peak-type texture components in the Euler space.

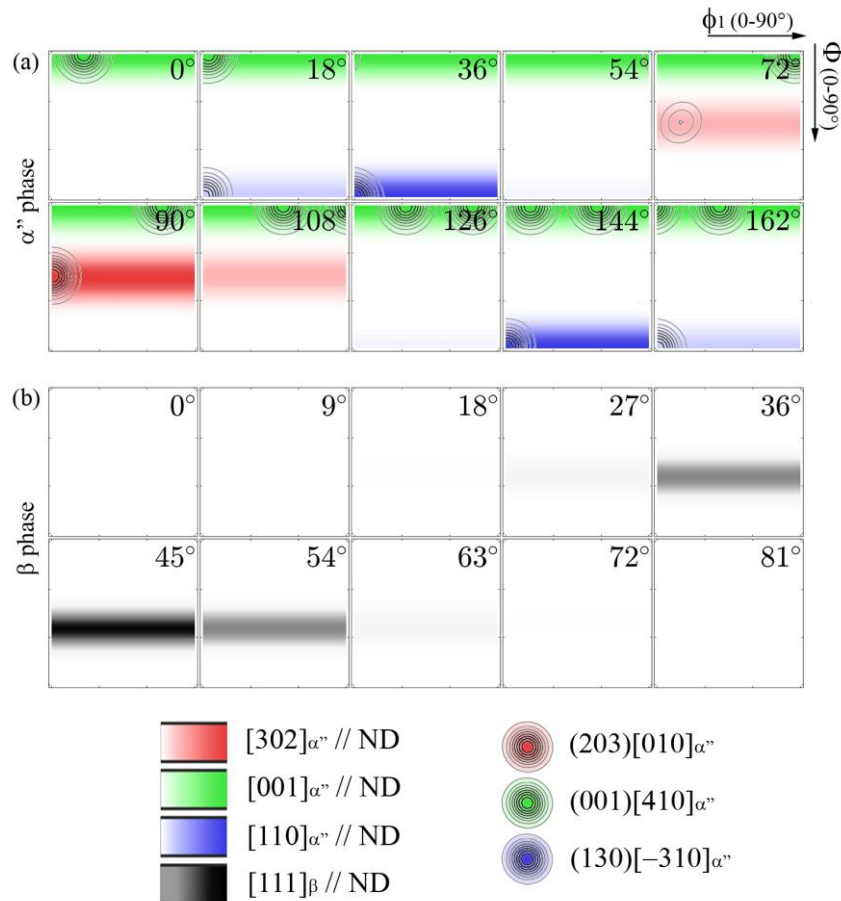


Figure 32: Location of some ideal fiber and peak-type texture components in the Euler orientation space ( $\phi_1$ ,  $\Phi$ ,  $\phi_2$ ).

The estimated ODFs based on XRD pole figure data are shown in Figure 33. A practical way to verify the reliability of an ODF is comparing the experimental pole figures with those reconstructed from ODF data. The reconstructed pole figures are shown in Figure 34, presenting a very good similarity with the original pole figures shown in Figure 31. Note that the reconstructed pole figures are complete ( $\alpha$  angle is not limited to  $75^\circ$ ).

For calculations of ODF volume within a certain orientation it was used the MTEX MATLAB Toolbox, considering a misorientation tolerance of  $15^\circ$  from the ideal texture component.

The ODF of the 51% sample (Figure 33-a) confirm the  $(203)[010]_{\alpha'}$  component, representing 3.8% of total ODF volume. This component could be considered as the maximum of a partial fiber  $[302]_{\alpha'} \parallel \text{ND}$  (12.4%). The ODF also shows other texture components that were not easily noticeable on the experimental pole figures: the fiber  $[001]_{\alpha'} \parallel \text{ND}$  (6.4%), with maximum at  $(001)[410]_{\alpha'}$  (4.8%), and the fiber component  $[110]_{\alpha'} \parallel \text{ND}$  (8.6%). The  $(130)[-310]_{\alpha'}$  texture component, saw in the pole figures, showed to be the weakest component (2.6%).

The ODF of the 85% deformed sample (Figure 33-b) shows the following texture components:  $[302]_{\alpha'} \parallel \text{ND}$  (11.8%) fiber with maximum at  $(203)[010]_{\alpha'}$  (4.0%),  $[001]_{\alpha'} \parallel \text{ND}$  (6.15%) fiber with maximum at  $(001)[410]_{\alpha'}$  (4%) and  $[110]_{\alpha'} \parallel \text{ND}$  (9.18%) fiber with maximum at  $(130)[-310]_{\alpha'}$  (2.6%).

The ODF of the recrystallized sample (85%REC) (Figure 33-c) shows two texture components:  $[302]_{\alpha'} \parallel \text{ND}$  (9.9%) fiber and  $[110]_{\alpha'} \parallel \text{ND}$  fiber (25.6%) with maximum at  $(130)[-310]_{\alpha'}$  (13.8%). The  $[001]_{\alpha'} \parallel \text{ND}$  component, seen in the deformed samples, is no longer present. The  $[110]_{\alpha'} \parallel \text{ND}$  fiber texture found in this sample is the strongest component found by XRD texture analysis.

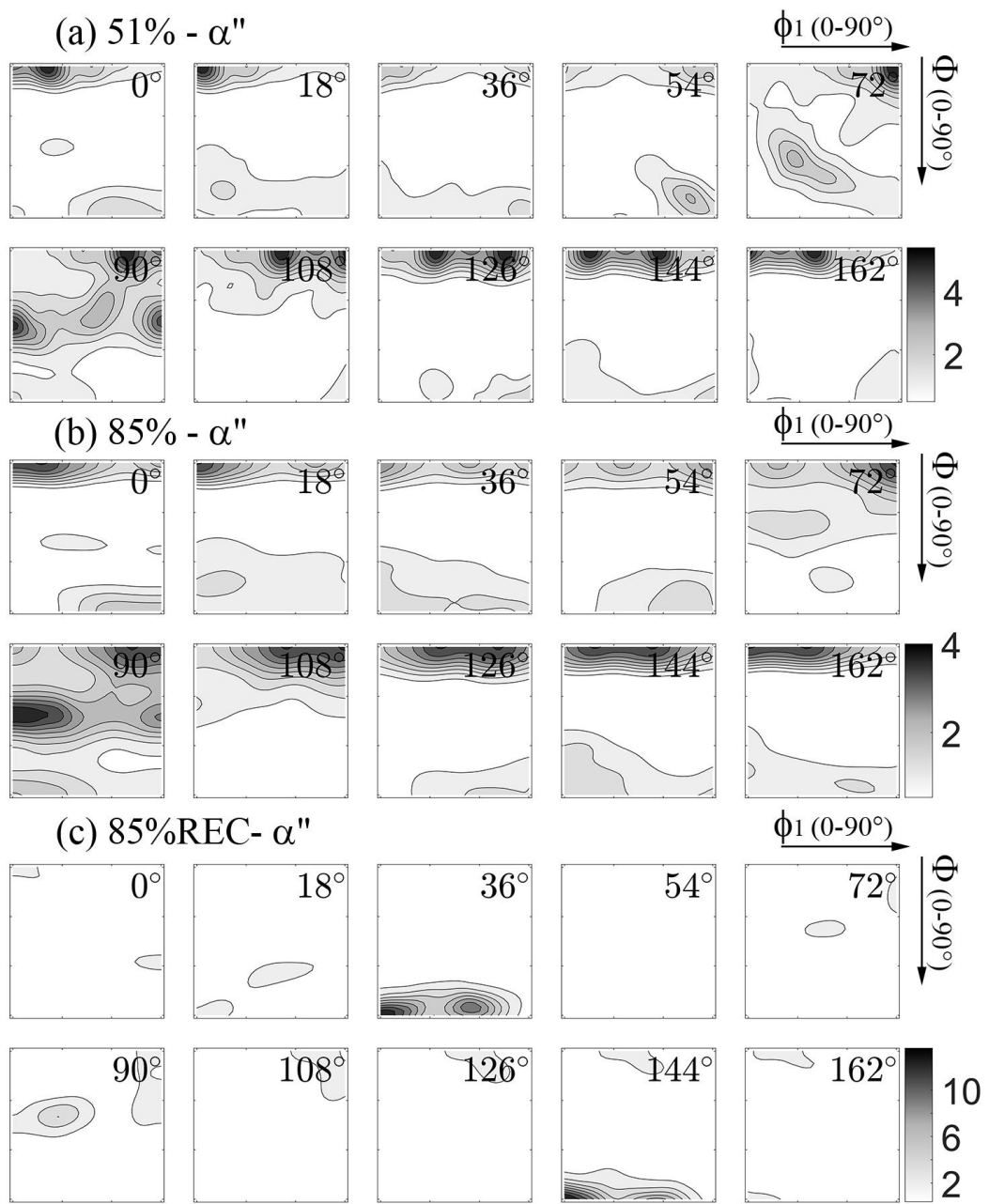


Figure 33: Orientation distribution functions of (a) 51%, (b) 85% and (c) recrystallized (85%REC) samples. Scale bars represent multiples of random distribution (m.r.d.).

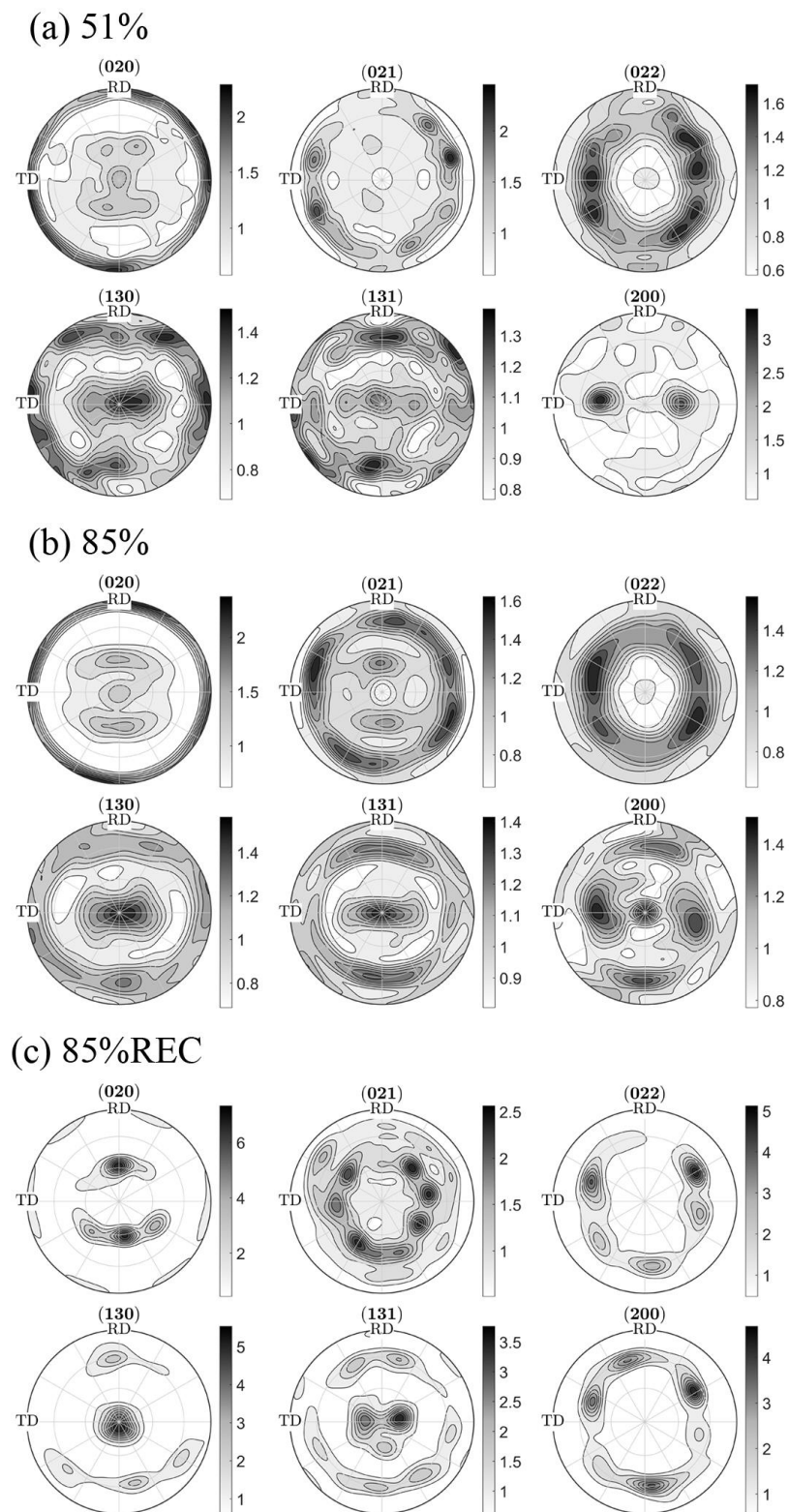


Figure 34: Reconstructed pole figures from the estimated orientation distribution functions (ODFs) of samples (a) 51%, (b) 85% and (c) 85%REC. Scale bars represent multiples of random distribution (m.r.d.).



### *EBSD texture analysis*

Only the texture of the recrystallized sample (85%REC) was investigated by EBSD mapping since deformed samples presented low quality EBSPs, due to crystal defects and grain refinement.

EBSD mapping of three different regions of a recrystallized sample were performed to obtain information about crystallographic texture. Figure 35 shows the band contrast image for these three regions and the mean angular deviation (MAD) distribution for the three regions summed. EBSD measurements with MAD equal or smaller than 1 will be not considered for calculations. Grain boundaries and martensite laths are clearly distinguished and some heterogeneity on martensite lath density is observed.

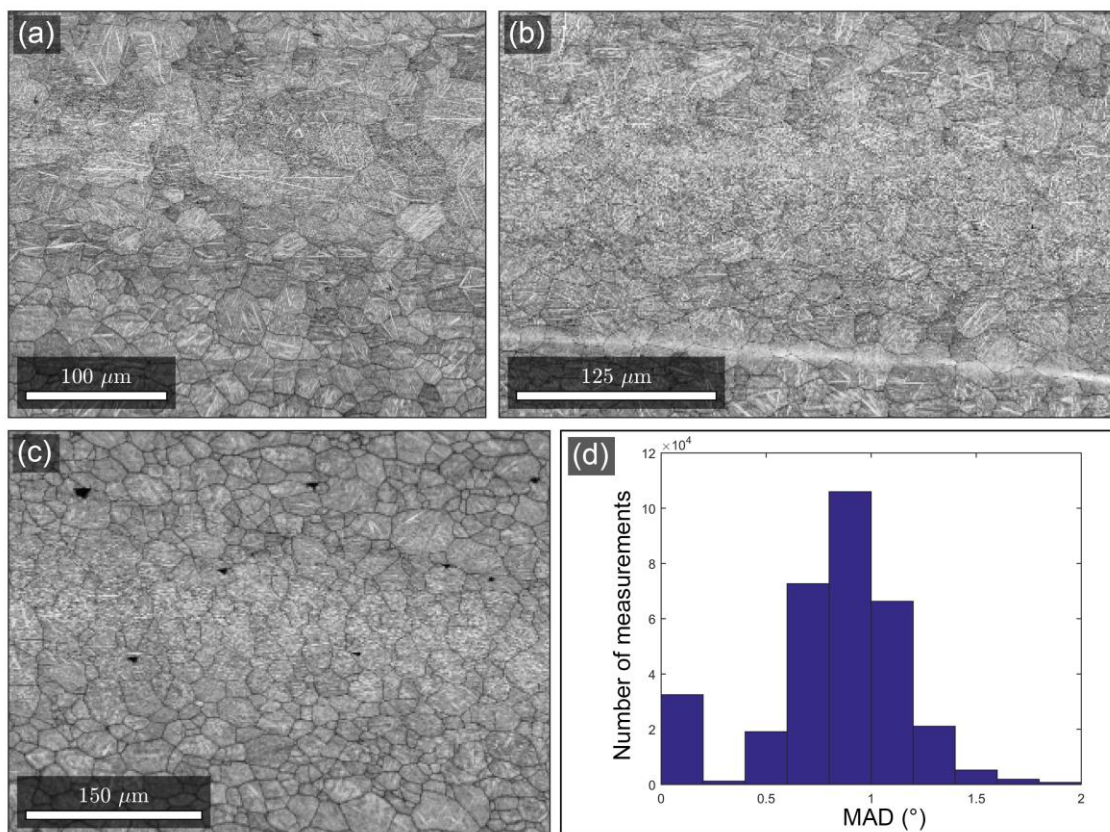


Figure 35: (a, b, c) EBSD band contrast map of three different regions of a recrystallized (85%REC) sample and (d) the mean angular deviation (MAD) distribution for all regions summed.

Figure 36 shows the orientation distribution functions of  $\alpha''$  and  $\beta$  phases for the recrystallized sample (85%REC), calculated from the EBSD maps showed in Figure 35. It was identified two texture components for the  $\alpha''$  phase: fiber  $[302]_{\alpha''} \parallel \text{ND}$  and  $[110]_{\alpha''} \parallel \text{ND}$ , representing 34,2% and 24% of ODF volume, respectively. For the  $\beta$  phase it was identified a strong fiber component  $[111]_{\beta} \parallel \text{ND}$  (47.5%).

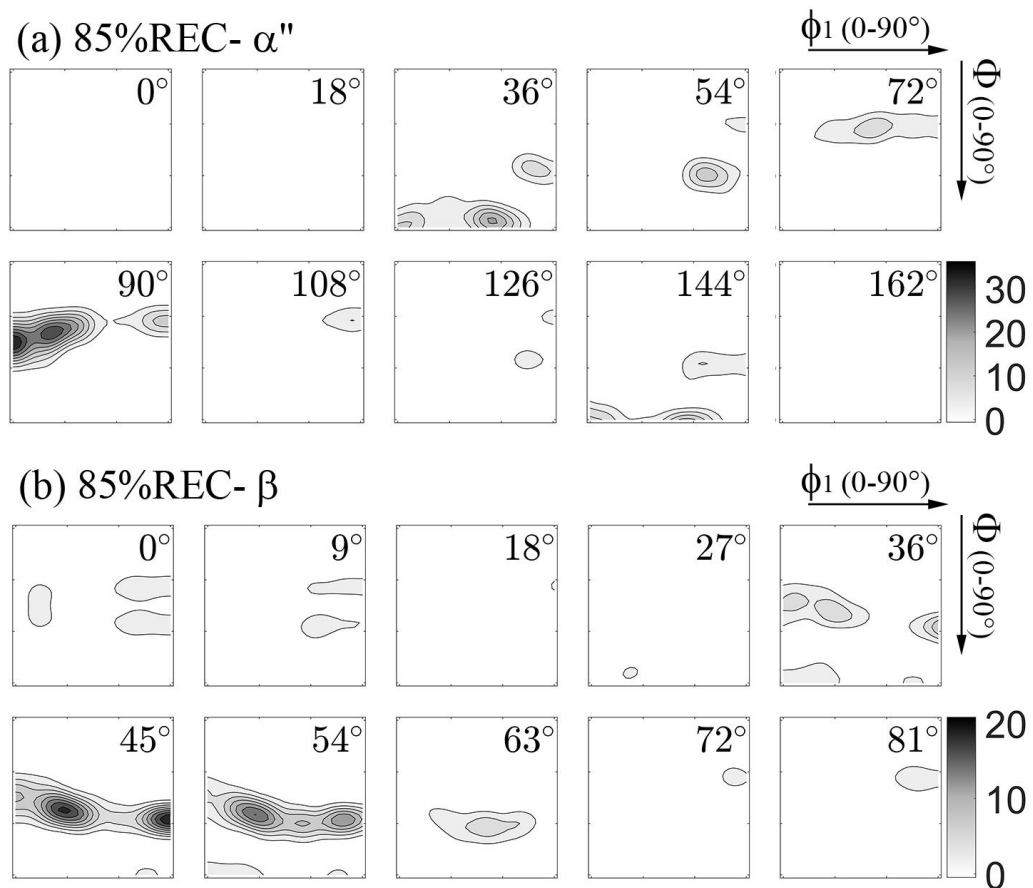


Figure 36: Orientation distribution functions of (a)  $\alpha''$  and (b)  $\beta$  phases for the recrystallized sample (85%REC), estimated from EBSD measurements of the regions shown in Figure 35.

Scale bars represent multiples of random distribution (m.r.d.).

### *Overview of texture components*

Table 2 shows the texture components found by EBSD and XRD analysis, as well as the quantification of each component. The 51% and 85% deformed samples were analyzed only by X-ray diffraction (XRD) and no information about texture of  $\beta$  phase was possible to be determined, as explained earlier. These samples do not present a strong texture, being the most important component the  $[302]_{\alpha''} \parallel \text{ND}$  fiber, representing about 12% of total volume of  $\alpha''$  phase.

The 85%REC sample was analyzed by both XRD and EBSD. The  $[110]_{\alpha''} \parallel \text{ND}$  fiber represents about 25% of  $\alpha''$  volume, as confirmed by both techniques, whilst the  $[302]_{\alpha''} \parallel \text{ND}$  fiber component express about 10% and 34% of total volume when analyzed by XRD and EBSD, respectively.

EBSD and XRD techniques showed a similar amount of the  $[110]_{\alpha''} \parallel \text{ND}$  fiber component. The difference observed in the  $[302]_{\alpha''} \parallel \text{ND}$  fiber component may be caused by variations of texture in different regions of the specimen.

Table 2: Overview of the crystallographic texture components observed by XRD and EBSD analyses. It was used a tolerance of 15° from ideal orientation for quantifications.

Sample	Method of calculation	Phase	Texture component and fiber maximum (if significant)
51%	ODF from DRX pole figures	$\alpha''$	[302]  ND fiber (12.4%) with maximum at (203)[010] (3.8%)
			[110]  ND fiber (8.6%)
			[001]  ND fiber (6,4%) with maximum at (001)[410] (4.8%)
		$\beta$	Not measured
85%	ODF from DRX pole figures	$\alpha''$	[302]  ND fiber (11.8%) with maximum at (203)[010] (4.0%)
			[110]  ND fiber (9.18 %)
			[001]  ND fiber (6.15%) with maximum at (001)[410] (4.0%)
		$\beta$	Not measured
85% REC	ODF from DRX pole figures	$\alpha''$	[302]  ND fiber (9.9%)
			[110]  ND fiber (25.6%) with maximum at (130)[-310] (13.8%)
		$\beta$	Not measured
	ODF from EBSD	$\alpha''$	[302]    ND fiber (34.2%) with maximum at $\phi_1=0, \Phi=45, \phi_2=90$ (20%)
			[110]    ND fiber (24.0%) with maximum at $\phi_1=58, \Phi=90, \phi_2=144$ (5.6%)
		$\beta$	[111] $_{\beta}$    ND fiber (63.0%) with maximum at $\phi_1=90, \Phi=57, \phi_2=45$ (47.5%)

The alignment of direction [010] along the rolling direction has already been observed for the  $\alpha''$  phase (HANADA; MASAHASHI; JUNG, 2013; MATSUMOTO; WATANABE;

HANADA, 2005, 2007). MATSUMOTO et al. (2005, 2007) found  $(200)[010]_{\alpha'}$  and  $(220)[001]_{\alpha'}$  textures of  $\alpha'$  for Ti-Nb-Sn alloys. In a more recent work, HAYAMA et al. (2014) reported  $(1-21)[-214]_{\alpha'}$  and  $(1-42)[213]_{\alpha'}$  textures for a Ti-35Nb alloy.

#### *On the origin of texture components*

As explained on section 2.2, the cubic titanium phase ( $\beta$ ) partially transforms to a martensitic orthorhombic phase ( $\alpha'$ ) upon rapid cooling from high temperatures. The martensite laths and the  $\beta$  matrix must obey the following Burger's orientation relationship:  $(-110)_{\beta} // (001)_{\alpha'}$  and  $[111]_{\beta} // [110]_{\alpha'}$ . Due to the cubic symmetry of  $\beta$  phase, it is known that for each orientation of  $\beta$ , six different orientations of  $\alpha'$  phase can be originated from the  $\beta \rightarrow \alpha'$  transformation. Figure 37 shows the EBSD analysis of a single grain of Ti-30Nb-4Sn alloy containing both  $\beta$  and  $\alpha'$  phases. This sample is free of deformation.

From the Euler colored maps of Figure 37 (b, c), it has been identified one orientation of  $\beta$  and six different orientations of  $\alpha'$ . By plotting these orientations on the  $(-110)_{\beta}$ ,  $(001)_{\alpha'}$ ,  $[111]_{\beta}$  and  $[110]_{\alpha'}$  pole figures (Figure 37-d, e, f, g), it is confirmed that all orientations of  $\alpha'$  agree with the Burgers orientation relationship of the  $\beta \rightarrow \alpha'$  transformation. The  $\beta$  phase has its  $[111]$  crystal direction near parallel to the normal specimen direction (ND). From the six possible orientations of  $\alpha'$ , three have the  $[110]_{\alpha'}$  direction aligned to ND and the other three have the  $[302]_{\alpha'}$  direction aligned to ND. This grain is therefore oriented accordingly to the fibers  $[111]_{\beta} // ND$ ,  $[110]_{\alpha'} // ND$  and  $[302]_{\alpha'} // ND$  previously observed.

From the discussion above, it becomes clear that the fibers  $[110]_{\alpha'} // ND$  and  $[302]_{\alpha'} // ND$  are transformation-type textures derived from the  $\beta$  phase texture  $[111]_{\beta} // ND$ . The fiber  $[001]_{\alpha'} // ND$  found in the 51% and 85% deformed samples could have been originated, not from quenching, but from the cold rolling deformation process.

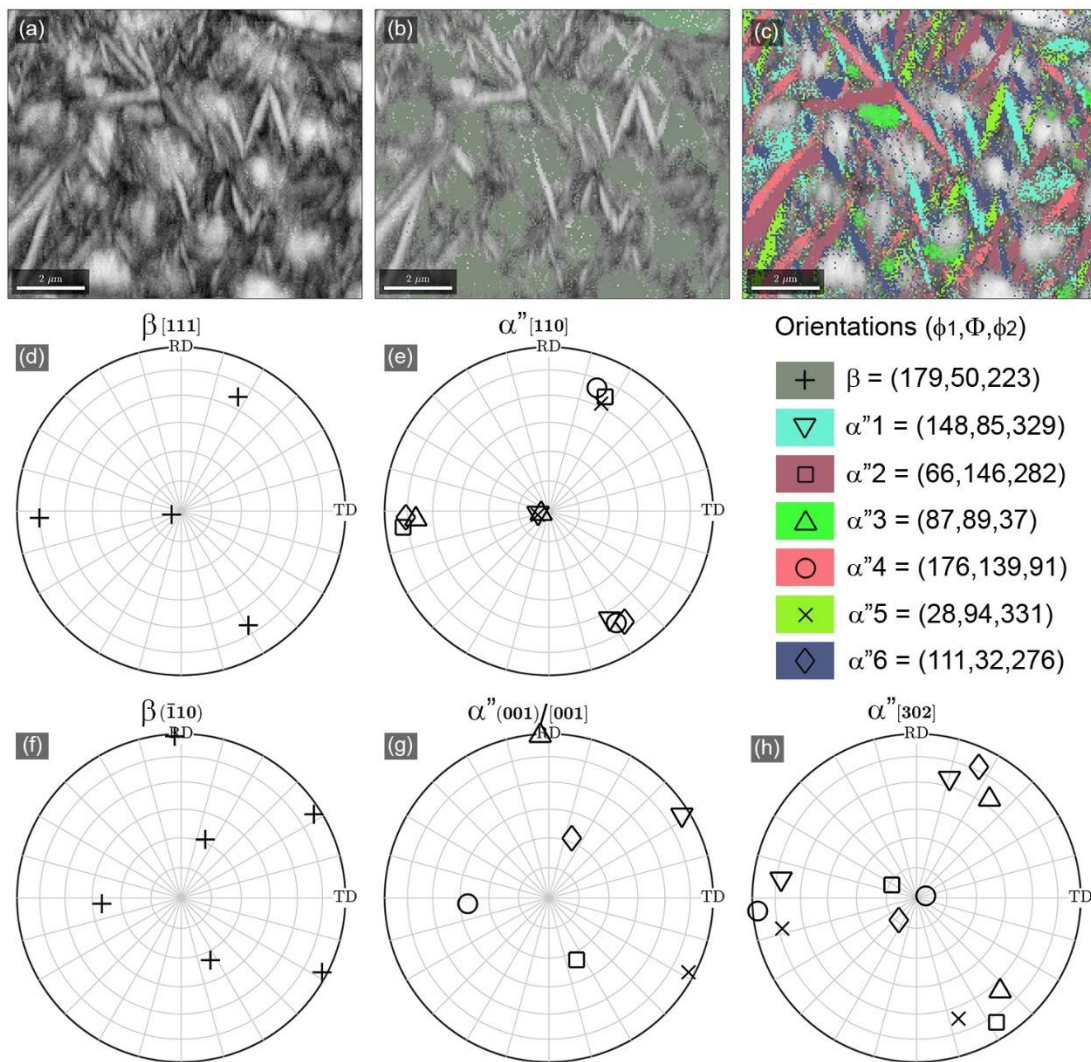


Figure 37: EBSD analysis of a single grain composed by a matrix of  $\beta$  phase and  $\alpha'$  martensite laths formed upon rapid cooling. (a) Band contrast map; (b, c) Euler colored orientation maps for (b)  $\beta$  and (c)  $\alpha'$  phases. (d, e, f, g, h) Pole figure plots for all identified orientations.

### *Elasticity tensors*

Once the ODFs describing specimen's texture have been estimated, it is possible to predict elastic modulus anisotropy by combining the ODFs with the stiffness tensors of  $\alpha'$  and  $\beta$  phases. The stiffness constants ( $C$ ) of  $\alpha'$  and  $\beta$  phases were calculated by Sun et al. (SUN et

al., 2007). These constants form an elasticity tensor that predicts the elastic modulus in any crystal direction  $[uvw]$  by applying the following equations (NYE, 2013):

For cubic systems:

*Equation 2: Elastic modulus of a cubic crystal in a  $[uvw]$  (Miller) direction.*

$$E_{[uvw]}^{cubic} = s_{11} - 2(s_{11} - s_{12} - \frac{1}{2}s_{44})(l_1^2 l_2^2 + l_2^2 l_3^2 + l_3^2 l_1^2)$$

For orthorhombic systems:

*Equation 3: Elastic modulus of an orthorhombic crystal in a  $[uvw]$  (Miller) direction.*

$$E_{[uvw]}^{orthorhombic} = l_1^4 s_{11} + 2l_1^2 l_2^2 s_{12} + 2l_1^2 l_3^2 s_{13} + l_2^2 s_{22} + 2l_2^2 l_3^2 s_{23} + l_3^4 s_{33} + l_2^2 l_3^2 s_{44} + l_1^2 l_3^2 s_{55} + l_1^2 l_2^2 s_{66}$$

Where the  $s$  values are the compliance constants ( $S=C^{-1}$ ) defined by the elasticity tensor and  $l_1$ ,  $l_2$  and  $l_3$  are the cosines of the angles between any desired crystal direction  $[uvw]$  and the three main crystal axes  $[001]$ ,  $[010]$  and  $[001]$ , respectively.

The variation elastic modulus for different crystal directions in both cubic  $\alpha''$  and orthorhombic  $\beta$  titanium phases is shown in Figure 38.

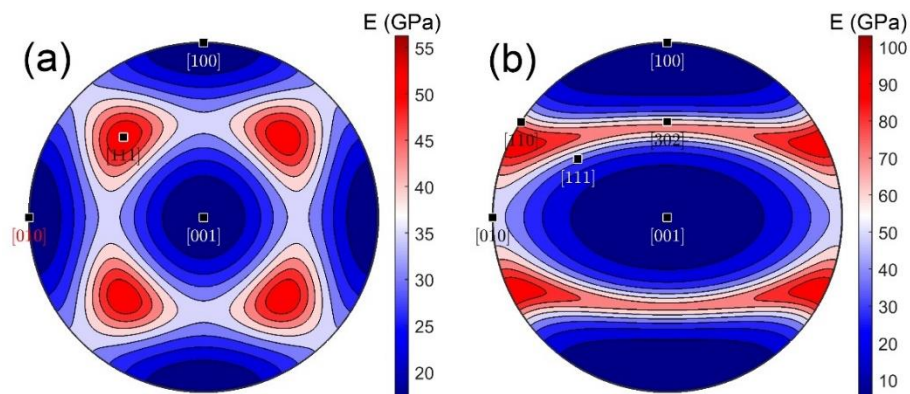


Figure 38: Variation of elastic modulus as a function of crystal directions of (a)  $\beta$  and (b)  $\alpha''$  phases, according to the elastic constants calculated by Sun et al. (SUN et al., 2007).

Once we have the elasticity tensors of  $\alpha''$  and  $\beta$  phases and the orientation distribution functions (ODFs) describing how crystals are oriented, it is possible to create the elasticity tensor for each specimen. MTEX software was used for calculations, using the Voigt approximation (see (BUNGE, 1993), page 321). More information about tensor calculations using MTEX can be found in the work of MAINPRICE et al. (2011).

In total, it was obtained three ODFs from XRD texture analysis describing the orientations of  $\alpha''$  phase for the 51%, 85% and 85%REC samples (Figure 33) and two ODFs from EBSD analysis describing texture of  $\alpha''$  and  $\beta$  phases for the 85%REC sample (Figure 36).

The calculated stiffness tensors are:

$$C_{XRD}^{\alpha''\text{phase}}(51\% \text{ sample}) = \begin{bmatrix} 144.92 & 91.55 & 92.59 & 0 & 0 & 0 \\ 91.55 & 146.18 & 91.36 & 0 & 0 & 0 \\ 92.59 & 91.36 & 146.1 & 0 & 0 & 0 \\ 0 & 0 & 0 & 25.6 & 0 & 0 \\ 0 & 0 & 0 & 0 & 26.64 & 0 \\ 0 & 0 & 0 & 0 & 0 & 27.160 \end{bmatrix}$$

$$C_{XRD}^{\alpha''\text{phase}}(85\% \text{ sample}) = \begin{bmatrix} 145.35 & 91.91 & 91.92 & 0 & 0 & 0 \\ 91.91 & 145.75 & 91.7 & 0 & 0 & 0 \\ 91.92 & 91.7 & 146.04 & 0 & 0 & 0 \\ 0 & 0 & 0 & 25.92 & 0 & 0 \\ 0 & 0 & 0 & 0 & 26.62 & 0 \\ 0 & 0 & 0 & 0 & 0 & 26.9 \end{bmatrix}$$

$$C_{XRD}^{\alpha''\text{phase}}(85\%REC \text{ sample}) = \begin{bmatrix} 145.53 & 94.98 & 89.9 & 0 & 0 & 0 \\ 94.98 & 145.93 & 89.50 & 0 & 0 & 0 \\ 89.9 & 89.5 & 147.97 & 0 & 0 & 0 \\ 0 & 0 & 0 & 25.97 & 0 & 0 \\ 0 & 0 & 0 & 0 & 27.02 & 0 \\ 0 & 0 & 0 & 0 & 0 & 25.3 \end{bmatrix}$$

$$C_{EBSD}^{\alpha''\text{phase}}(85\%REC \text{ sample}) = \begin{bmatrix} 146.53 & 90.18 & 88.82 & 0 & 0 & 0 \\ 90.18 & 150.27 & 90.94 & 0 & 0 & 0 \\ 88.82 & 90.94 & 151.53 & 0 & 0 & 0 \\ 0 & 0 & 0 & 19.39 & 0 & 0 \\ 0 & 0 & 0 & 0 & 26.22 & 0 \\ 0 & 0 & 0 & 0 & 0 & 28.24 \end{bmatrix}$$



$$C_{EBS D}^{\beta \text{ phase}} (85\%REC \text{ sample}) = \begin{bmatrix} 130.02 & 100.55 & 97.96 & 0 & 0 & 0 \\ 100.55 & 130.43 & 97.54 & 0 & 0 & 0 \\ 97.96 & 97.54 & 133.03 & 0 & 0 & 0 \\ 0 & 0 & 0 & 11.82 & 0 & 0 \\ 0 & 0 & 0 & 0 & 12.24 & 0 \\ 0 & 0 & 0 & 0 & 0 & 14.83 \end{bmatrix}$$

Note that for the 51% and 85% deformed specimens only information about texture of the  $\alpha''$  phase is available. Then, it will not be possible to calculate the stiffness tensors of  $\beta$  phase for these samples. For the recrystallized (85%REC) specimen, texture of both  $\alpha''$  and  $\beta$  phases were determined by EBSD. Therefore, the total elastic modulus of this specimen can be calculated by the average of the elastic modulus of the two phases, proportional to the amount of each phase:

$$C_{EBS D}^{Total} = 0.62 C_{EBS D}^{\alpha'' \text{ phase}} + 0.38 C_{EBS D}^{\beta \text{ phase}} (85\%REC \text{ sample})$$

$$= \begin{bmatrix} 140.19 & 94.16 & 92.33 & 0 & 0 & 0 \\ 94.16 & 142.65 & 93.48 & 0 & 0 & 0 \\ 92.33 & 93.48 & 144.43 & 0 & 0 & 0 \\ 0 & 0 & 0 & 16.48 & 0 & 0 \\ 0 & 0 & 0 & 0 & 20.85 & 0 \\ 0 & 0 & 0 & 0 & 0 & 23.09 \end{bmatrix}$$

The elastic modulus for any direction relative to the specimen's reference frame can now be calculated using the stiffness tensors above and the following equation:

*Equation 4: Elastic modulus of an orthorhombic (orthotropic) specimen in a desired specimen direction.*

$$E_{[specimen \text{ direction}] }^{orthorhombic} = m_1^4 s_{11} + 2m_1^2 m_2^2 s_{12} + 2m_1^2 m_3^2 s_{13} + m_2^2 s_{22} + 2m_2^2 m_3^2 s_{23} + m_3^4 s_{33} + m_2^2 l_3^2 s_{44} + m_1^2 m_3^2 s_{55} + m_1^2 m_2^2 s_{66}$$

Where the  $s$  values are the compliance constants ( $S=C^{-1}$ ) defined by the elasticity tensors and  $m_1$ ,  $m_2$  and  $m_3$  are the cosines of the angles between any desired specimen direction and the reference frame axes RD, TD and ND, respectively.

In Figure 39 we see a stereographic projection representation of elastic modulus values as a function of specimen direction.

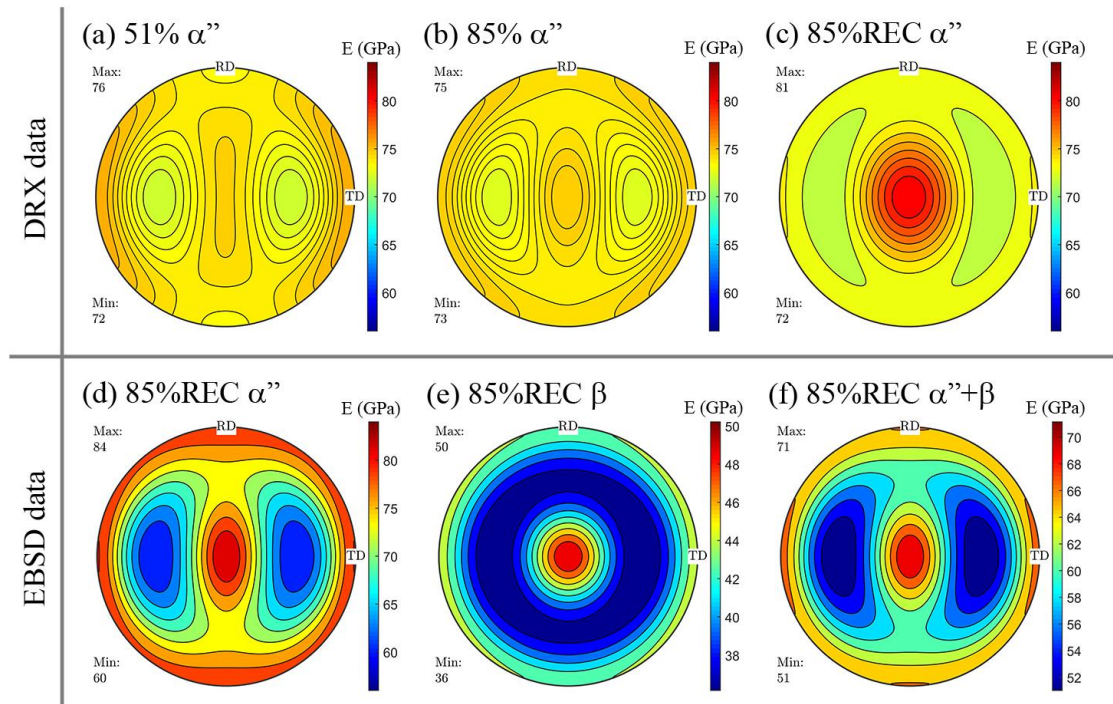


Figure 39: Influence of crystallographic texture on the specimen's elastic modulus anisotropy, considering (a, b, c) the  $\alpha''$  ODFs found by XRD analysis of 51%, 85% and 85%REC samples and (d, e) the  $\alpha''$  and  $\beta$  ODFs found by EBSD analysis of the 85%REC sample. The average elastic modulus of the 85%REC sample is shown on (f).

#### 4.3.2 Texture of the laser surface melted samples

The fusion zone (FZ) and heat affected zone (HAZ) of the laser surface melted samples was analyzed by electron backscattered diffraction (EBSD) mapping. Figure 40 shows the band contrast image and IPF colored orientation maps for the 85% deformed and laser surface melted sample. As already observed on the visible-light microscopy images of Figures 23 and 25, grains near to the FZ have been recrystallized and grown. As the distance from fusion zone increases, recrystallization and grain growth effect become less intense and EBSD patterns become worse due to the very refined condition of microstructure in these regions (see section 2.1, page 22). The orientation map colors in Figure 40 (b, c) represent the crystal directions oriented along the normal specimen direction (ND). It is possible to see a great amount of grains oriented with the  $[111]_{\beta}$ ,  $[110]_{\alpha'}$  and  $[302]_{\alpha'}$  directions nearly parallel to ND. The calculated ODF volume fractions in the  $[111]_{\beta} \parallel \text{ND}$ ,  $[110]_{\alpha'} \parallel \text{ND}$  and  $[302]_{\alpha'}$  fibers are 54%, 10% and 24%, respectively.

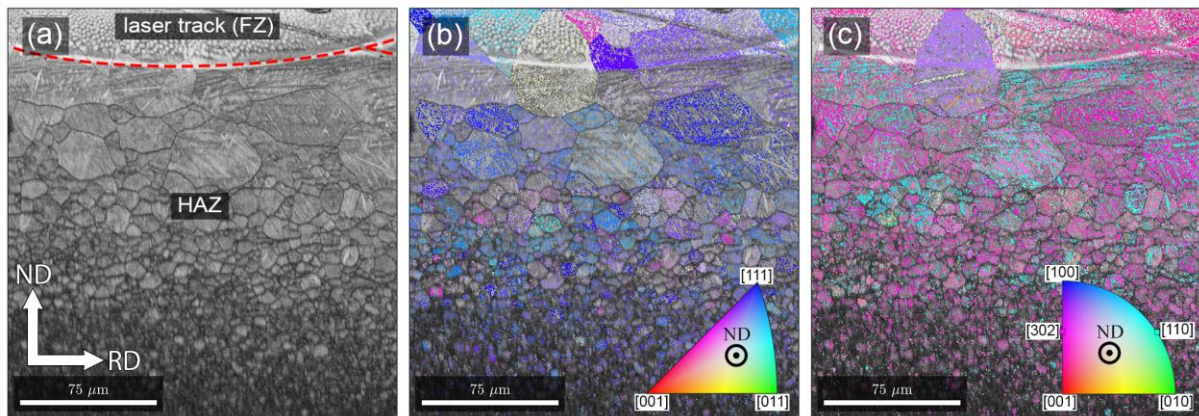


Figure 40: EBSD analysis for the 85% deformed and laser surface melted sample. (a) Band contrast (BC) image showing the fusion zone (red rectangle) and heat affected zone (blue rectangle). (b, c) Orientation maps for the (b)  $\beta$  phase and (c)  $\alpha'$  phase superposed with the BC image. EBSD analysis were performed on the RD-ND plane, transverse to laser tracks, and the orientation maps show the crystals directions aligned in the normal direction.

A similar analysis was performed for the recrystallized (85%REC) specimen. EBSD mappings of three distinct regions are shown in Figure 41. As for the 85% deformed specimen, IPF colored maps show that grains are predominantly oriented with  $[111]_{\beta}$ ,  $[110]_{\alpha'}$  and  $[302]_{\alpha'}$  directions nearly parallel to ND. For this sample, considering the three analyzed regions summed, the calculated ODF volume fractions in the  $[111]_{\beta} \parallel \text{ND}$ ,  $[110]_{\alpha'} \parallel \text{ND}$  and  $[302]_{\alpha'}$  fibers are 61%, 30% and 24%, respectively.

The epitaxial nature of fusion zone solidification, as already observed in Figures 25b and 24, can be easily seen in the orientation maps of Figures 40 and 41. Observing the  $\beta$  grain orientations, showed in Figure 40-b and Figure 41-d,e,f, we see that grains cross the FZ/HAZ interface, indicated by red dashed lines in Figure 40-a and Figure 41-a,b,c.

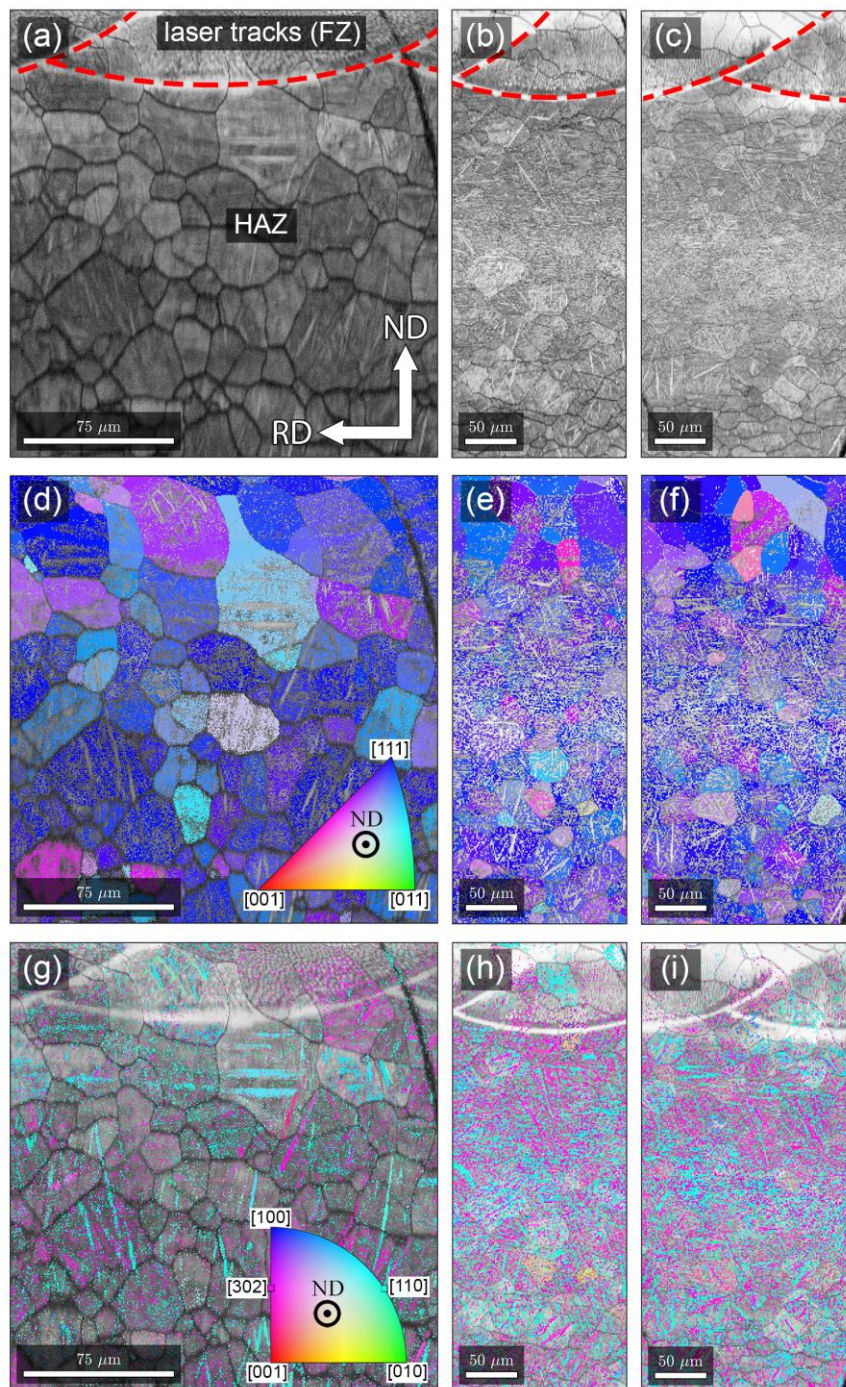


Figure 41: EBSD analysis for three distinct regions of the recrystallized (85%REC) and laser surface melted sample. (a, b, c) Band contrast (BC) image showing the fusion zone (red rectangle) and heat affected zone (blue rectangle). (d, e, f, g, h, i) Orientation maps for the (d, e, f)  $\beta$  phase and (g, h, i)  $\alpha''$  phase superposed with the BC image. EBSD analysis were performed on the RD-ND plane, transverse to laser tracks, and the orientation maps show the crystals directions aligned in the normal direction.

The crystallographic texture observed in the fusion and heat affected zones are the same observed in the base materials. Some differences on volume fractions were observed, but this could be expected since EBSD analysis of laser surface melted samples covered smaller areas. As for the base materials, texture in the laser treated region showed to be stronger for the 85%REC sample.

To better investigate the laser surface melting effects, EBSD analyses with higher magnifications were performed. Simultaneously, energy-dispersive X-ray spectroscopy (EDS) mapping was carried out to verify element segregation during solidification. Figure 42 presents an EBSD/EDS analysis of an 85% deformed sample within a region of two superposed laser melted tracks. The EDS maps show that fusion zone boundaries have been enriched with niobium and depleted of titanium. The same occurred in some regions inside the fusion zone, forming a microsegregation pattern caused by the cellular solidification process. As explained in section 4.1.3, titanium is rejected during solidification process. Consequently, the first regions to solidify will be richer in Nb content and the last ones will be poorer in this element. The same effect was observed for the recrystallized (85%REC) specimen, as shown on the EBSD/EDS analyses of figures 43 and 44. The  $\beta$ -stabilizer effect of Nb made the Nb-richer zones to be composed of  $\beta$  phase, as observed on the  $\beta$  IPF-colored maps shown in Figures 42, 43 and 44.

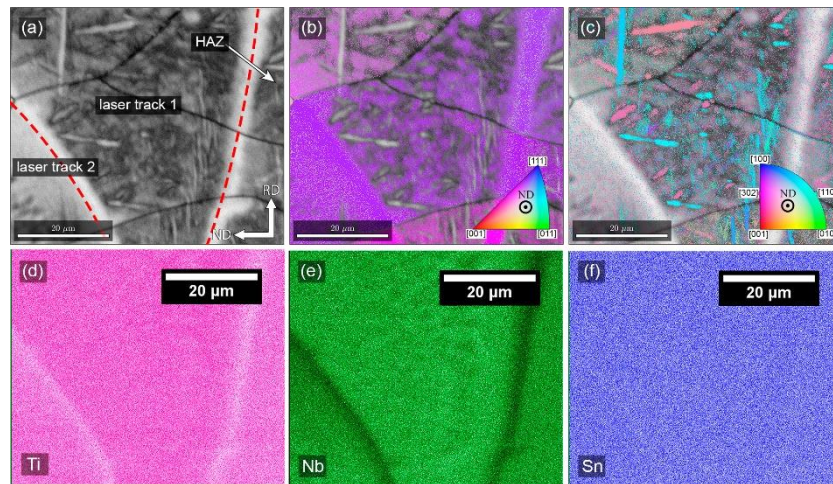


Figure 42: EBSD analysis for the 85% deformed and laser surface melted sample. (a) Band contrast (BC). (b, c) Orientation maps for the (b)  $\beta$  phase and (c)  $\alpha'$  phase superposed with the BC image. (d, e, f) EDS maps for Ti, Nb and Sn elements. EBSD analysis were performed on the RD-ND plane, transverse to laser tracks, and the orientation maps show the crystals directions aligned in the normal direction. Laser track boundaries are marked with red dashed lines.

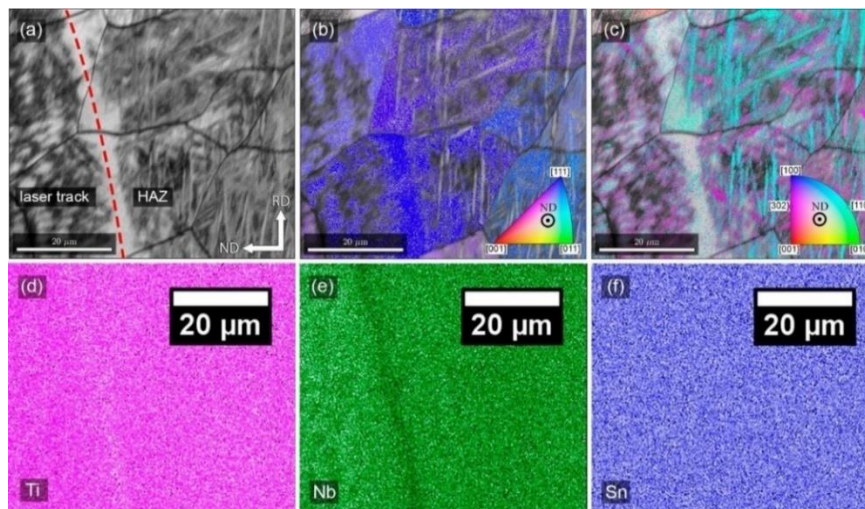


Figure 43: EBSD analysis for the recrystallized (85%REC) and laser surface melted sample. (a) Band contrast (BC). (b, c) Orientation maps for the (b)  $\beta$  phase and (c)  $\alpha'$  phase superposed with the BC image. (d, e, f) EDS maps for Ti, Nb and Sn elements. EBSD analysis were performed on the RD-ND plane, transverse to laser tracks, and the orientation maps show the crystals directions aligned in the normal direction. Laser track boundary is marked with a red dashed line.

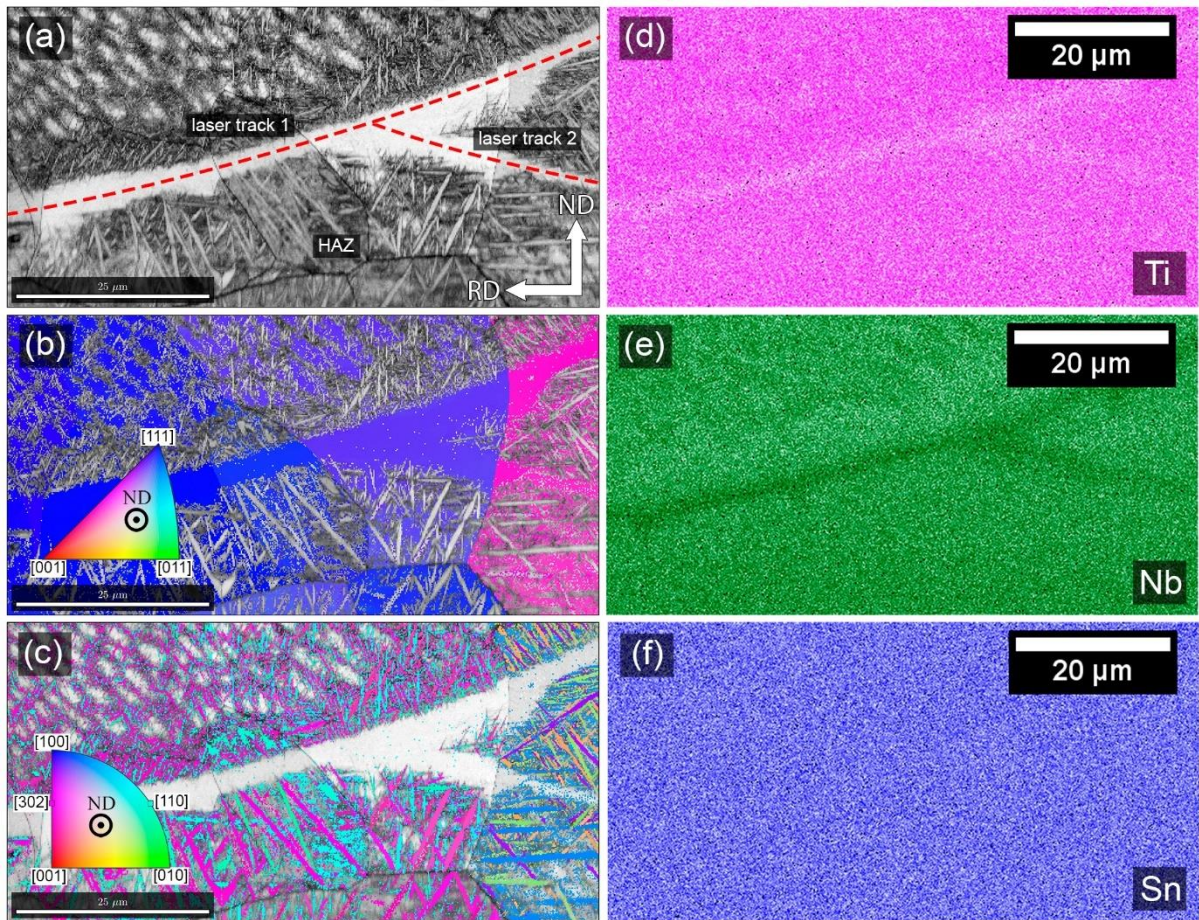


Figure 44: EBSD analysis for the recrystallized (85%REC) and laser surface melted sample.

(a) Band contrast (BC). (b, c) Orientation maps for the (b)  $\beta$  phase and (c)  $\alpha'$  phase superposed with the BC image. (d, e, f) EDS maps for Ti, Nb and Sn elements. EBSD analysis were performed on the RD-ND plane, transverse to laser tracks, and the orientation maps show the crystals directions aligned in the normal direction. Laser track boundaries are marked with a red dashed line.

The EBSD/EDS analyses of the heat affected zone for the 85% deformed (Figures 45 and 46) and 85%REC samples (Figure 47) showed no segregation in this region.



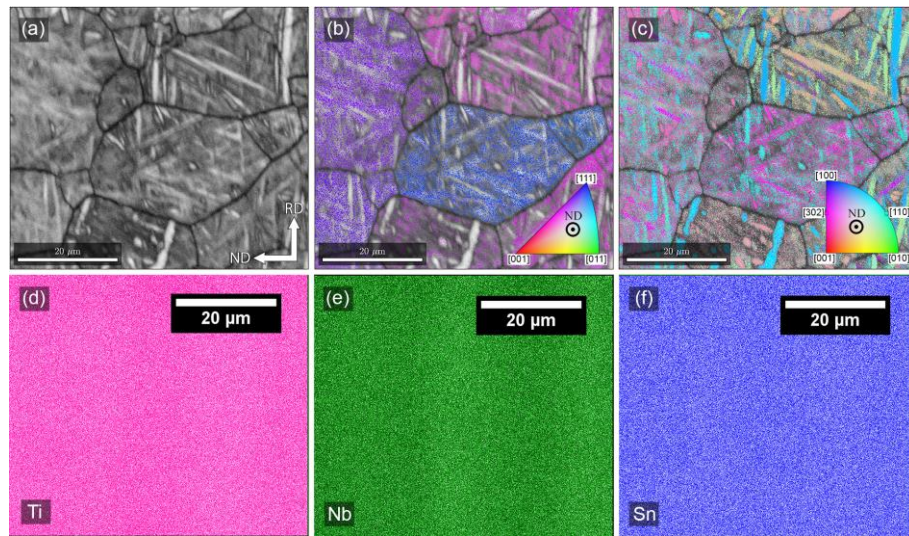


Figure 45: EBSD analysis for the 85% deformed and laser surface melted sample. (a) Band contrast (BC). (b, c) Orientation maps for the (b)  $\beta$  phase and (c)  $\alpha'$  phase superposed with the BC image. (d, e, f) EDS maps for Ti, Nb and Sn elements. EBSD analysis were performed on the RD-ND plane, transverse to laser tracks, and the orientation maps show the crystals directions aligned in the normal direction.

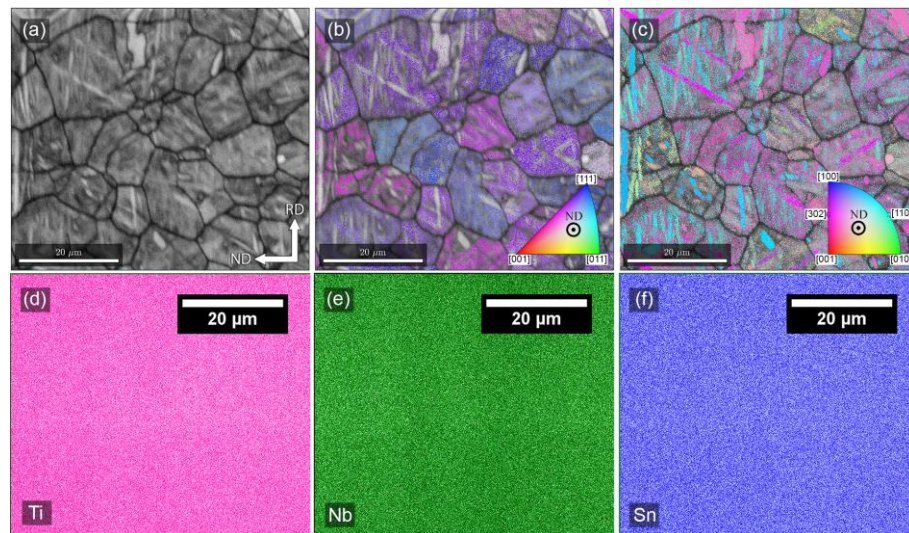


Figure 46: EBSD analysis for the 85% deformed and laser surface melted sample. (a) Band contrast (BC). (b, c) Orientation maps for the (b)  $\beta$  phase and (c)  $\alpha'$  phase superposed with the BC image. (d, e, f) EDS maps for Ti, Nb and Sn elements. EBSD analysis were performed on the RD-ND plane, transverse to laser tracks, and the orientation maps show the crystals directions aligned in the normal direction.

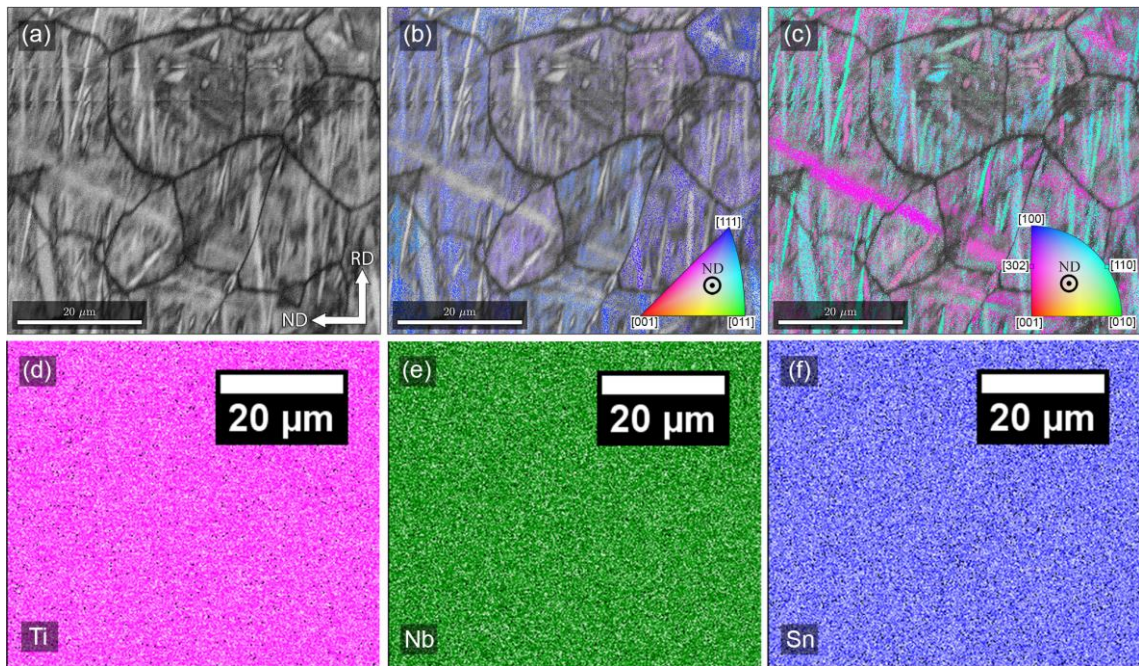


Figure 47: EBSD analysis for the recrystallized (85% REC) and laser surface melted sample.

(a) Band contrast (BC). (b, c) Orientation maps for the (b)  $\beta$  phase and (c)  $\alpha''$  phase superposed with the BC image. (d, e, f) EDS maps for Ti, Nb and Sn elements. EBSD analysis were performed on the RD-ND plane, transverse to laser tracks, and the orientation maps show the crystals directions aligned in the normal direction.

#### 4.4 Correlation between crystallographic texture and nanoindentation measurements

The correlation between nanoindentation measurements and crystal orientation is not straightforward. In traditional tension/compression tests, the load imposed to the specimen is unidirectional (uniaxial). Conversely, in nanoindentation tests the deformation imposed by the indenter is triaxial and dependent on the tip geometry. Some works show that computer simulations can be a good tool to understand the complex plasticity mechanisms involved in this technique (EIDEL, 2011; RENNER et al., 2016; RUESTES et al., 2014; TALAEI; NOURI; ZIAEI-RAD, 2016). Another factor to be considered is that the volume of material affected by indenter may comprise more than one grain and/or second phases. The alloy studied in this work has a refined structure, especially in most deformed specimens. Therefore, indentations will be affected by  $\beta$  grain boundaries of several grains and/or  $\alpha''$  laths. Lower indentation load

and depth would be a better choice to avoid this effect (HAUŠILD; MATERNA; NOHAVA, 2014), since the affected volume is smaller.

An important question to be answered is whether the decrease in elastic modulus with increasing deformation is related to texture. As seen in Table 2, the texture intensity estimated for the 51% and 85% deformed specimens are very similar. Thus, texture cannot explain, by itself, the difference in elastic modulus (Figure 29) observed between these samples. As previously discussed, nanoindentation measurements (Figure 29) for the recrystallized (85%REC) specimen show that both elastic modulus and hardness revert to values close to the less deformed specimen (24%). Therefore, the most important factor that seems to be affecting the decrease of elastic modulus among different samples is work hardening, rather than texture.

There is a contradiction between the elastic modulus measured by nanoindentation in this work and the elastic modulus found by ultrasound technique in the work of FANTON et al. (2016). Conversely to what was found by nanoindentation, ultrasound measurements show a decrease in elastic modulus after recrystallization treatment (gray line in Figure 29). This fact indicates that texture could be affecting ultrasound measurements, since plastic deformation effects cannot explain it. However, further investigation is necessary to solve this issue.

Besides, texture could be affecting nanoindentation measurements made on different cross sections. LI et al. (2014) studied a nanograined titanium alloy and observed lower nanoindentation modulus for measurements made on the RD cross section, pointing out texture as the most probable cause. As seen in the elasticity tensors represented in Figure 39, the 85%REC sample should present the highest anisotropy of elastic properties. However, once again texture cannot support nanoindentation results, since measurements for this sample show no significant difference in elastic modulus between RD, TD and ND cross sections (Figure 29). This behavior corroborates to the idea that elastic modulus and hardness determined by nanoindentation was not affected by texture.

Finally, if it is not texture, what could explain the differences in nanoindentation values between measurements made on RD, TD and ND cross sections? Another important factor that could be affecting material's anisotropy is the dislocation structure induced by plastic deformation, as discussed in section 4.2.2. This phenomenon could explain why deformed samples from 36% to 85% presented higher differences in measurements made on different

cross sections, whilst the less deformed sample (24%), as well as the 85% REC sample, presented no significant difference.

## 5 CONCLUSIONS

For the analyses, it was used six Ti-30Nb-4Sn samples in total: five cold rolled specimens with 24, 36, 51, 68 and 85% of thickness reduction, and a recrystallized specimen named as 85%REC. All samples were water quenched from temperatures above  $\beta$  transus and their microstructure was composed by both orthorhombic  $\alpha''$  martensite and cubic  $\beta$  phases. Laser surface melting was successfully carried out on the 51%, 85% and 85%REC specimens. It had different effects on the deformed and recrystallized specimens. Deformed specimens presented a recrystallized zone near to the fusion zone.

Nanoindentation measurements were carried out on the ND, TD and RD cross sections of each sample. Comparing the results between samples, it was observed that hardness increased proportionally to the amount of plastic deformation, whilst elastic modulus presented the opposite behavior. Nanoindentation results showed that, after recrystallization, both elastic modulus and hardness returned to similar values found in the undeformed state. Comparing results between different cross sections, the 24% and 85%REC samples showed no significant variation, whilst samples from 36 to 85% of deformation presented an important difference between different on the RD cross section.

In what concern the laser surface melted specimens, both fusion and recrystallized zones had their elastic modulus and hardness returned to the values of the undeformed state, creating a stiffness gradient between surface (presenting higher elastic modulus) and substrate (presenting lower elastic modulus). This gradient is, in principle, not beneficial for enhancement of fatigue life. For the recrystallized specimen, both surface and substrate presented similar elastic modulus and hardness.

To better understand the nanoindentation results, a detailed study of crystallographic texture was carried out. XRD pole figure analysis was performed on the 51%, 85% and 85%REC samples. Since XRD- $\beta$  peaks were not clearly distinguished, texture of this phase was not possible to be determined by this technique. EBSD analysis was successfully carried out to measure both  $\beta$  and  $\alpha''$  phase textures in the 85%REC specimen. Since grains in deformed samples were relatively refined, EBSD analysis of these samples was not possible due to a resolution limitation of the technique. For the 51% and 85% deformed specimens, the following

fiber texture components were found:  $[302]_{\alpha''} \parallel \text{ND}$ ,  $[110]_{\alpha''} \parallel \text{ND}$  and  $[001]_{\alpha''} \parallel \text{ND}$ , corresponding to an estimated volume fraction of about 12%, 9% and 6.5%, respectively. For the 85%REC sample, both EBSD and XRD techniques showed the same texture components for the  $\alpha''$  phase: the  $[110]_{\alpha''} \parallel \text{ND}$  fiber, with a volume fraction of about 25%, using both techniques; and the  $[302]_{\alpha''} \parallel \text{ND}$  fiber, corresponding to 10% and 34%, using XRD and EBSD, respectively. The  $\beta$  phase texture, measured only by EBSD, revealed a  $[111]_{\beta} \parallel \text{ND}$  fiber component, representing a volume fraction of 63%.

Considering the Burgers orientation relationship that the  $\beta \rightarrow \alpha''$  transformation must follow, it was concluded that the  $[302]_{\alpha''} \parallel \text{ND}$  and  $[110]_{\alpha''} \parallel \text{ND}$  fiber textures are transformation-type textures derived from the  $[111]_{\beta} \parallel \text{ND}$  texture. The  $[001]_{\alpha''} \parallel \text{ND}$ , however, could be a deformation-type texture, formed during cold rolling process, since it was observed only in the as-deformed specimens.

The 85%REC specimen showed the strongest texture, being for this reason the sample that should present higher anisotropy of properties. Nevertheless, it is not supported by the nanoindentation results, since properties on different cross sections were very similar for this sample. On the other hand, deformed specimens showed a significant difference of properties between different cross section, then the dislocation structure originated from plastic deformation was pointed out as the most probable factor affecting these results. Additionally, the reduction of elastic modulus after deformation was attributed to the increase of dislocation density and other defects, making atomic bonds weaker. Texture did not seem to have effect on the nanoindentation measurements.

With respect to the laser surface melted samples, no significant change in crystallographic texture was observed between fusion zone, heat affected zone and substrate, for any sample. The texture components found in the laser treated surface was the same of those found in the substrate. The gradient of properties created in the deformed specimens is attributed to work hardening related phenomena, rather than crystallographic texture differences.

## 6 REFERENCES

ALMEIDA, A. et al. Laser-assisted synthesis of Ti-Mo alloys for biomedical applications. **Materials Science and Engineering C**, v. 32, n. 5, p. 1190–1195, jul. 2012.

BACHMANN, F.; HIELSCHER, R.; SCHAEBEN, H. Texture Analysis with MTEX – Free and Open Source Software Toolbox. **Solid State Phenomena**, v. 160, p. 63–68, 2010.

BAHL, S.; SUWAS, S.; CHATTERJEE, K. The importance of crystallographic texture in the use of titanium as an orthopedic biomaterial. **RSC Advances**, v. 4, n. 72, p. 38078, 5 ago. 2014.

BALLA, V. K. et al. Microstructure, mechanical and wear properties of laser surface melted Ti6Al4V alloy. **Journal of the Mechanical Behavior of Biomedical Materials**, v. 32, p. 335–344, 2014.

BRAILOVSKI, V. et al. Bulk and porous metastable beta Ti–Nb–Zr(Ta) alloys for biomedical applications. **Materials Science and Engineering: C**, v. 31, n. 3, p. 643–657, 2011.

BUNGE, H. J. **Texture Analysis in Materials Science: Mathematical Methods**, 1993.

CALLISTER, W. D. **Materials science and engineering : an introduction**. [s.l.] Wiley, 2000.

CANDEL, J. J. et al. Effects of Laser Surface Melting on Ti-30Nb-2Sn Sintered Alloy. **Advanced Engineering Materials**, jun. 2016.

CARDOSO, F. F. et al. Ti–Mo alloys employed as biomaterials: Effects of composition and aging heat treatment on microstructure and mechanical behavior. **Journal of the Mechanical Behavior of Biomedical Materials**, v. 32, p. 31–38, 2014.

CHEN, Y. et al. Texture evolution and dynamic recrystallization in a beta titanium alloy during hot-rolling process. **Journal of Alloys and Compounds**, v. 618, p. 146–152, 2015.

CONDE, A. et al. Corrosion behaviour of steels after laser surface melting. **Materials &**

**Design**, v. 21, n. 5, p. 441–445, 2000.

**Core Materials - Colaborative Open Resource Environment - for Materials**. Disponível em: <<http://core.materials.ac.uk/search/detail.php?id=3270>>. Acesso em: 8 dez. 2016.

CORREA, D. R. N.; KURODA, P. A. B.; GRANDINI, C. R. Structure, Microstructure, and Selected Mechanical Properties of Ti-Zr-Mo Alloys for Biomedical Applications. **Advanced Materials Research**, v. 922, n. MAY, p. 75–80, 2014.

CUI, W. et al. Crystal orientation dependence of Young's modulus in Ti-Nb-based  $\beta$ -titanium alloy. **Science China Technological Sciences**, v. 53, n. 6, p. 1513–1519, 2010.

D'YAKONOVA, N. B.; LYASOTSKII, I. V.; RODIONOV, Y. L. Orthorhombic martensite and the  $\omega$  phase in quenched and deformed titanium alloys with 20–24 at % Nb. **Russian Metallurgy (Metally)**, v. 2007, n. 1, p. 51–58, 2007.

DE VITERI, V. S.; FUENTES, E. Titanium and Titanium Alloys as Biomaterials. In: **Tribology - Fundamentals and Advancements**. [s.l.] InTech, 2013.

EIDEL, B. Crystal plasticity finite-element analysis versus experimental results of pyramidal indentation into (0 0 1) fcc single crystal. **Acta Materialia**, v. 59, n. 4, p. 1761–1771, 2011.

ENGLER O., R. V. **Introduction to texture analysis**. [s.l.: s.n.].

FANTON, L. et al. Texture Development in Cold Deformed and Recrystallized Ti-30Nb-4Sn Alloy and Its Effects on Hardness and Young's Modulus. **Advanced Engineering Materials**, p. 27–29, maio 2016.

FIELD, D. P. Texture Evolution and Control. In: **ASM Handbooks: OnlineMetallography and Microstructures**. [s.l.: s.n.]. p. 215–226.

FIZANNE-MICHEL, C. et al. Determination of hardness and elastic modulus inverse pole figures of a polycrystalline commercially pure titanium by coupling nanoindentation and EBSD techniques. **Materials Science and Engineering A**, v. 613, p. 159–162, 2014.



FOGAGNOLO, J. B. et al. A novel proposal to manipulate the properties of titanium parts by laser surface alloying. **Scripta Materialia**, v. 68, n. 7, p. 471–474, 2013.

FOGAGNOLO, J. B. et al. Surface stiffness gradient in Ti parts obtained by laser surface alloying with Cu and Nb. **Surface and Coatings Technology**, v. 297, p. 34–42, 2016.

FROES, F. H. **Titanium : physical metallurgy, processing, and applications**. [s.l.: s.n.].

GEPREEL, M. A.-H. Texturing Tendency in  $\beta$ -Type Ti-Alloys. In: **Recent Developments in the Study of Recrystallization**. [s.l.] InTech, 2013. p. 20.

HAMMOND, C. **The Basics of Crystallography and Diffraction**. Third Edit ed. New York, NY: [s.n.].

HANADA, S. et al. Effect of swaging on Young's modulus of  $\beta$  Ti-33.6Nb-4Sn alloy. **Journal of the Mechanical Behavior of Biomedical Materials**, v. 32, p. 310–320, 2014a.

HANADA, S. et al. Fabrication of a high-performance hip prosthetic stem using  $\beta$  Ti-33.6Nb-4Sn. **Journal of the Mechanical Behavior of Biomedical Materials**, v. 30, p. 140–149, 2014b.

HANADA, S.; MASAHASHI, N.; JUNG, T. K. Effect of stress-induced  $\alpha''$  martensite on Young's modulus of  $\beta$  Ti-33.6Nb-4Sn alloy. **Materials Science and Engineering A**, v. 588, p. 403–410, 2013.

HANSEN, N.; JENSEN, D. J. Flow stress anisotropy caused by geometrically necessary boundaries. **Acta Metallurgica Et Materialia**, v. 40, n. 12, p. 3265–3275, 1992.

HAUŠILD, P.; MATERNA, A.; NOHAVA, J. Characterization of Anisotropy in Hardness and Indentation Modulus by Nanoindentation. **Metallography, Microstructure, and Analysis**, v. 3, n. 1, p. 5–10, 2014.

HAY, J.; AGEE, P.; HERBERT, E. Continuous stiffness measurement during instrumented indentation testing. **Experimental Techniques**, v. 34, n. 3, p. 86–94, 2010.

HAYAMA, A. O. F. et al. Crystallographic texture evolution in Ti-35Nb alloy deformed by cold rolling. **Materials and Design**, v. 60, p. 653–660, 2014.

HICKMAN, B. S. The formation of omega phase in titanium and zirconium alloys: A review. **Journal of Materials Science**, v. 4, n. 6, p. 554–563, 1969.

HIELSCHER, R.; SCHAEBEN, H. A novel pole figure inversion method: Specification of the MTEX algorithm. **Journal of Applied Crystallography**, v. 41, n. 6, p. 1024–1037, 2008.

HO, W. . F. et al. Structure and properties of cast binary Ti-Mo alloys. **Biomaterials**, v. 20, n. 22, p. 2115–2122, 1999.

HOSEINI, M. et al. On the importance of crystallographic texture in the biocompatibility of titanium based substrate. **Journal of Biomedical Materials Research Part A**, v. 102, n. 10, p. 3631–3638, 2014.

INAMURA, T. et al. Anisotropy and Temperature Dependence of Young's Modulus in Textured TiNbAl Biomedical Shape Memory Alloy. **Materials Transactions**, v. 46, n. 7, p. 1597–1603, 2005.

KANNATEY-ASIBU JR., E. **Principles of Laser Materials Processing**. New Jersey: Wiley, 2009.

KENT, D.; WANG, G.; DARGUSCH, M. Effects of phase stability and processing on the mechanical properties of Ti–Nb based  $\beta$  Ti alloys. **Journal of the Mechanical Behavior of Biomedical Materials**, v. 28, p. 15–25, 2013.

KIM, H. Y. et al. Martensitic transformation, shape memory effect and superelasticity of Ti-Nb binary alloys. **Acta Materialia**, v. 54, n. 9, p. 2419–2429, 2006.

KOCKS, U. F.; WENK, H.-R.; TOMÉ, C. N. **Texture and anisotropy: preferred orientations in polycrystals and their effect on materials properties**. [s.l.] Cambridge University Press, 2000.

LEE, C. M.; JU, C. P.; LIN, J. H. C. Structure-property relationship of cast Ti-Nb alloys. p.

314–322, 2002.

LEE, D. N.; HAN, H. N. Recrystallization Textures of Metals and Alloys. **Recent Developments in the Study of Recrystallization**, p. 232, 2013.

LEYENS, C.; PETERS, M. **Titanium and Titanium Alloys**. 2. ed. Weinheim, FRG: Wiley-VCH Verlag GmbH & Co. KGaA, 2003.

LI, Z. et al. Nanoindentation Hardness and Elastic Modulus of Nano-Grained Titanium Produced by Asymmetric and Symmetric Rolling. **Journal of Nanoscience and Nanotechnology**, v. 14, n. 10, p. 7740–7744, 2014.

LI, Z. J.; WINTHER, G.; HANSEN, N. Anisotropy in rolled metals induced by dislocation structure. **Acta Materialia**, v. 54, n. 2, p. 401–410, 2006.

LIU, X.; CHU, P. K.; DING, C. Surface modification of titanium, titanium alloys, and related materials for biomedical applications. **Materials Science and Engineering R: Reports**, v. 47, n. 3–4, p. 49–121, 2004.

LIU, Y. et al. Kinetic modeling of diffusion mobilities in bcc Ti–Nb alloys. **Journal of Alloys and Compounds**, v. 476, p. 429–435, 2009.

LOPES, E. S. N. **Correlação entre transformações de fases e comportamento mecânico de ligas Ti-Nb-Sn e sua aplicação na concepção de implantes ortopédicos com propriedades otimizadas**. [s.l.] University of Campinas, 2009.

LÜTJERING, G.; WILLIAMS, J. C. **Titanium**. Berlin, Heidelberg: Springer Berlin Heidelberg, 2007.

LUTJERING, G.; WILLIAMS, J. C. **Titanium (Engineering Materials and Processes)**. [s.l.] Springer, 2007.

MAINPRICE, D.; HIELSCHER, R.; SCHAEUBEN, H. Calculating anisotropic physical properties from texture data using the MTEX open-source package. **Geological Society, London, Special Publications**, v. 360, n. 1, p. 175–192, 2011.

MATSUMOTO, H.; WATANABE, S.; HANADA, S. Beta TiNbSn Alloys with Low Young's Modulus and High Strength. **Materials Transactions**, v. 46, n. 5, p. 1070–1078, 2005.

MATSUMOTO, H.; WATANABE, S.; HANADA, S. Microstructures and mechanical properties of metastable  $\beta$  TiNbSn alloys cold rolled and heat treated. **Journal of Alloys and Compounds**, v. 439, n. 1–2, p. 146–155, 2007.

MORAES, P. E. L. et al. Effects of Sn addition on the microstructure, mechanical properties and corrosion behavior of Ti–Nb–Sn alloys. **Materials Characterization**, v. 96, p. 273–281, 2014.

NAG, S.; BANERJEE, R. Fundamentals of Medical Implant Materials. In: **ASM Handbook**. [s.l.] ASM International, 2012. v. 23p. 6–17.

NOLZE, G.; HIELSCHER, R. Orientations - perfectly colored. **Journal of Applied Crystallography**, v. 49, p. 1786–1802, 2016.

NOWELL, M. M.; WRIGHT, S. I. Phase differentiation via combined EBSD and XEDS. **Journal of Microscopy**, v. 213, n. 3, p. 296–305, 2004.

NYE, J. F. Physical Properties of Crystals. **Journal of Chemical Information and Modeling**, v. 53, n. 9, p. 1689–1699, 2013.

OSHIDA, Y. **Bioscience and Bioengineering of Titanium Materials**. [s.l.] Elsevier, 2013.

OZAKI, T. et al. Beta Ti Alloys with Low Young's Modulus. **Materials Transactions**, v. 45, n. 8, p. 2776–2779, 2004.

POPA, M. et al. Structural Analysis, Electrochemical Behavior, and Biocompatibility of Novel Quaternary Titanium Alloy with near  $\beta$  Structure. **Metallurgical and Materials Transactions A**, v. 45, n. 7, p. 3130–3143, 2014.

PRODANOV, L. et al. Initial cellular response to laser surface engineered biomaterials. **MRS Bulletin**, v. 36, n. 12, p. 1034–1042, 14 dez. 2011.

RENNER, E. et al. Sensitivity of the residual topography to single crystal plasticity parameters in Berkovich nanoindentation on FCC nickel. **International Journal of Plasticity**, v. 77, p. 118–140, 2016.

RIVA, R.; LIMA, M. S. F.; OLIVEIRA, A. C. Soldagem a laser de estruturas aeronáuticas. **Metalurgia & Materiais**, v. 65, p. 48–50, 2009.

RUESTES, C. J. et al. Atomistic simulation of tantalum nanoindentation: Effects of indenter diameter, penetration velocity, and interatomic potentials on defect mechanisms and evolution. **Materials Science and Engineering A**, v. 613, p. 390–403, 2014.

SAKAGUCHI, N. et al. Effect of Ta content on mechanical properties of Ti–30Nb–XTa–5Zr. **Materials Science and Engineering: C**, v. 25, n. 3, p. 370–376, 2005.

SALVADOR, C. A. F. **Nucleação da fase alfa durante tratamentos isotérmicos em ligas de titânio biomédicas do sistema Ti-Nb e Ti-Nb-Sn**. [s.l.] University of Campinas, 2015.

SALVADOR, C. A. F. et al. Microstructure evolution of Ti–30Nb–(4Sn) alloys during classical and step-quench aging heat treatments. **Materials Science and Technology**, p. 1–8, 8 ago. 2016.

SANDER, B.; RAABE, D. Texture inhomogeneity in a Ti-Nb-based beta-titanium alloy after warm rolling and recrystallization. **Materials Science and Engineering A**, v. 479, n. 1–2, p. 236–247, 2008.

SANDIN, H. R. Z. Heterogeneidades de deformação: uma visão microscópica. In: **Textura e relações de orientação**. 2. ed. São Paulo: [s.n.]. p. 19–34.

SCHWARTZ, A. J. J. et al. **Electron Backscatter Diffraction in Materials Science**. [s.l.: s.n.].

SILFVAST, W. P. **Laser Fundamentals**. 2. ed. [s.l.] Cambridge University Press, 2004.

SINGH, A. K.; SCHWARZER, R. A. Evolution of texture during thermomechanical processing of titanium and its alloys. **Transactions of the Indian Institute of Metals**, v. 61, n. 5, p. 371–387, 2008.

SOKOLOVA, T. A.; ANISIMOVA, L. I.; SOKOLOV, B. K. Texture of Cold-Rolled  $\beta$ -Titanium Alloys With Additions of Hydrogen. **Textures and Microstructures**, v. 32, n. 1–4, p. 101–106, 1999.

SUN, J. et al. Elastic properties of  $\beta$ ,  $\alpha'$  and  $\omega$  metastable phases in Ti–Nb alloy from first-principles. **Journal of Physics: Condensed Matter**, v. 19, n. 48, p. 486215, 2007.

SUN, R.; GUAN, Y.; ZHU, Y. DEVELOPMENT OF LASER SURFACE TECHNOLOGIES FOR ANTI-CORROSION ON MAGNESIUM ALLOYS: A REVIEW. **Surface Review and Letters**, v. 23, n. 4, p. 1630003, ago. 2016.

SUWAS, S.; RAY, R. K. **Crystallographic Texture of Materials**. London: Springer London, 2014.

TALAEI, M. S.; NOURI, N.; ZIAEI-RAD, S. Grain boundary effects on nanoindentation of Fe bicrystal using molecular dynamic. **Mechanics of Materials**, v. 102, p. 97–107, 2016.

TRAGER-COWAN. **Nanoscale characterisation of nitride semiconductor thin films using electron backscatter diffraction, electron channelling contrast imaging, cathodoluminescence and electron beam induced current**. Disponível em: <<http://gan-sem.phys.strath.ac.uk/>>. Acesso em: 12 ago. 2016.

WANG, L. et al. Microstructure and mechanical properties of cold-rolled TiNbTaZr biomedical beta titanium alloy. **Materials Science and Engineering A**, v. 490, n. 1–2, p. 421–426, 2008.

WANG, W.; LU, K. Nanoindentation measurement of hardness and modulus anisotropy in Ni<sub>3</sub>Al single crystals. 2016.

WILKINSON, A. J.; BRITTON, T. BEN. Strains, planes, and EBSD in materials science. **Materials Today**, v. 15, n. 9, p. 366–376, 2012.

WILKINSON, A. J.; HIRSCH, P. B. Electron diffraction based techniques in scanning electron microscopy of bulk materials. **Micron**, v. 28, n. 4, p. 279–308, 1997.

WRIGHT, S. I. et al. Introduction and comparison of new EBSD post-processing

methodologies. **Ultramicroscopy**, v. 159, n. P1, p. 81–94, 2015.

WRIGHT, S. I.; NOWELL, M. M. EDS Assisted Phase Differentiation in Orientation Imaging Microscopy. **Materials Science Forum**, v. 509, p. 11–16, 2006a.

WRIGHT, S. I.; NOWELL, M. M. EBSD image quality mapping. **Microscopy and Microanalysis**, v. 12, n. 1, p. 72–84, 2006b.

XU, Y. F. et al. Effects of cold deformation on microstructure, texture evolution and mechanical properties of Ti-Nb-Ta-Zr-Fe alloy for biomedical applications. **Materials Science and Engineering: A**, v. 547, p. 64–71, 2012.

YANG, Y. et al. Texture investigation of the superelastic Ti-24Nb-4Zr-8Sn alloy. **Journal of Alloys and Compounds**, v. 591, p. 85–90, 2014.

ZHOU, Y. L.; NIINOMI, M.; AKAHORI, T. Effects of Ta content on Young's modulus and tensile properties of binary Ti-Ta alloys for biomedical applications. **Materials Science and Engineering: A**, v. 371, n. 1–2, p. 283–290, 2004.